Search for Supersymmetry in Events with a Muon and Jets at the CMS Detector

von

Deborah Duchardt

Diplomarbeit in Physik

vorgelegt der

Fakultät für Mathematik, Informatik und Naturwissenschaften
der RWTH Aachen

im Oktober 2011

angefertigt am

III. Physikalischen Institut A

Prof. Dr. Thomas Hebbeker

Zusammenfassung

Supersymmetrie stellt eine vielversprechende Erweiterung des Standardmodells der Teilchenphysik dar. Sie liefert eine Lösung des Hierarchieproblems und ist in der Lage einen Kandidaten für Dunkle Materie zu präsentieren. Indem sie jedem Fermion des Standardmodells ein Boson zuordnet, sowie umgekehrt, wird die Anzahl der Teilchen in etwa verdoppelt. Bisher konnte noch kein Beweis für eine supersymmetrische Ordnung der Welt erbracht werden. Experimente an den LEP und Tevatron Beschleunigern haben Ausschlussgrenzen auf Parameter der SUSY Modelle gesetzt und so den Massenbereich der postulierten Teilchen eingeschränkt.

Diese Diplomarbeit befasst sich mit der Suche nach Supersymmetrie in den im Jahr 2010 am CMS Detektor aufgenommenen Daten, die $36\,\mathrm{pb}^{-1}$ entsprechen. Unter Annahme der R-Paritätserhaltung, wird im Rahmen des mSUGRA Modells eine Analyse im Kanal mit einem Myon, mehreren Jets und erheblicher fehlender transversalen Energie durchgeführt. Supersymmetrische Zerfälle sind durch lange Kaskaden charakterisiert, an deren Ende das stabile leichteste supersymmetrische Teilchen den Detektor ungesehen verlässt.

Untergrundprozese des Standardmodells ahmen die Topologie des Signals nach. Schnitte werden gesetzt um diese Untergründe zu reduzieren, wobei weiterhin eine hohe Effizienz des Signals gewährleistet wird. Um ein besseres Verständnis des QCD Multi-Jet Untergrunds zu erlangen, wird eine Methode erläutert, um diesen direkt aus den Daten zu extrahieren. Außerdem werden systematische Unsicherheiten der Signal- und Untergrundabschätzungen bewertet.

Da sich eine gute Übereinstimmung zwischen den Daten und der Vorhersage des Standardmodells ergibt, werden Ausschlussgrenzen innerhalb des supersymmetrischen Modells der minimalen Supergravitation gesetzt. Die Grenzen der vorherigen Experimente können bestätigt werden.

Abstract

Supersymmetry is a promising addition to the Standard Model of elementary particle physics, offering a solution to the hierarchy problem and presenting a dark matter candidate. It assigns a boson to every Standard Model fermion and vice versa, approximately doubling the number of particles. So far no evidence could be given for a supersymmetric world. Experiments at the LEP and Tevatron accelerators have set limits on the parameters of SUSY models, constraining mass range of the postulated particles.

This thesis takes up the search for supersymmetry using $36\,\mathrm{pb}^{-1}$ of data collected at the CMS detector in 2010. Assuming R-parity conservation and working within the framework of mSUGRA, the analysis is performed in the channel with one muon, several jets and substantial missing energy. Supersymmetric decays are characterized by long cascades ending with the stable lightest supersymmetric particle which escapes the detector unseen.

The signal's topology is mimicked by processes of the Standard Model. Cuts are applied to reduce these backgrounds while keeping the signal efficiency high. To gain a better understanding of the QCD multi-jet background a method is introduced to extract it directly from the data. Moreover, systematic uncertainties on the signal and background estimates are evaluated.

Finding the data to be in accordance with the Standard Model prediction, exclusion limits are set within the supersymmetric model of minimal supergravity. The limits from previous experiments can be confirmed.

Contents

Chapter 1

Introduction

Man's natural curiosity has lead to such principal questions as what the world around us is made of. The desire to understand the basic constituents of matter resulted in many models, each considering different aspects of the observations made over time. The most fundamental of these theories is the Standard Model (SM) of elementary particle physics. Developed over the last century, it describes the building blocks of matter as point-like particles. Within the Standard Model, they are held together by three forces: the electromagnetic, weak and strong interaction. Composite particles like protons and neutrons are formed, and in turn build up the nuclei of atoms. The electrons orbiting the nucleus are elementary particles themselves. From atoms one can proceed to molecules and crystals. Bit by bit, larger conglomerates can be formed leading to the objects around us. Stars and planets, held together by the gravitational force, form the galaxies of our universe. Chapter 2 will give a summary of the Standard Model with its particle content and the fundamental interactions.

Although the Standard Model has been verified to great precision, some unsolved issues still remain. How can the gravitational force be included in the SM? What is the nature of the dark matter found throughout the universe? These questions will be further outlined at the end of chapter 2.

Several additional theories have been developed on the path to finding answers. Among them the so called supersymmetry (SUSY) delivers promising explanations. It introduces a new symmetry between the different types of elementary particles. Many searches for evidence of this theory have been performed within the high energy physics community. So far none of them have shown proof of a supersymmetric world. Chapter 3 will give an introduction to supersymmetry, highlighting its basic features and signatures at hadron collisions.

With the startup of the Large Hadron Collider (LHC), the past two years have marked an important step to finding an answer to the question if supersymmetry exists. In 2010 a successful run at a center of mass energy of $\sqrt{s}$=7 TeV delivered 47 pb^{-1} of data. The Compact Muon Solenoid (CMS) is one of the experiments looking at the particle decays produced in the LHC proton-proton collisions. Chapter 4 will give an overview of the LHC and CMS detector. Furthermore, the methods used to reconstruct the collisions will be described.

This thesis uses the CMS 2010 dataset to conduct a search for supersymmetry in events with one muon, several jets and missing energy. Typically SUSY decays exhibit long cascades ending in the stable lightest superpartner, which escapes detection. Throughout the decay chain some leptons and several quarks will occur. The analysis is presented in chapter 5. First, backgrounds from SM processes mimicking the signal are discussed, followed by an explanation of the cut-based strategy used to reduce these backgrounds. Next, a method to estimate the QCD multi-jet background from data will be demonstrated, offering validation of the otherwise used Monte Carlo simulations. Systematic uncertainties on the measurement will be estimated, with emphasis on those resulting from the limited about the proton's parton density functions. As a final result, a limit on cross sections of supersymmetric processes will be set.

Note that natural units will be used throughout this study i.e., $c = \hbar = 1$. Consequently energies, masses and momenta are all given in electron-volts (eV).

Chapter 2

The Standard Model and its Shortcomings

The Standard Model (SM) of elementary particle physics describes the fundamental constituents of matter and the forces they interact with. Gravity is not included in this theory. The particles known today are listed in figure 2.1, along with a selection of their properties, such as mass and charge, as well as the year and location of their initial discovery. Further information on the particle spectrum will be delivered in section 2.1, followed by a summary of the fundamental forces in 2.2. If no additional reference is given in the text, the information in this chapter has been taken from [1].

The SM Higgs mechanism, as a possible realization of a necessary extension to the theory, will be discussed in section 2.3. Finally some of the unsolved questions of the Standard Model will be presented in section 2.4 which will lead to an introduction to Supersymmetry in chapter 3.

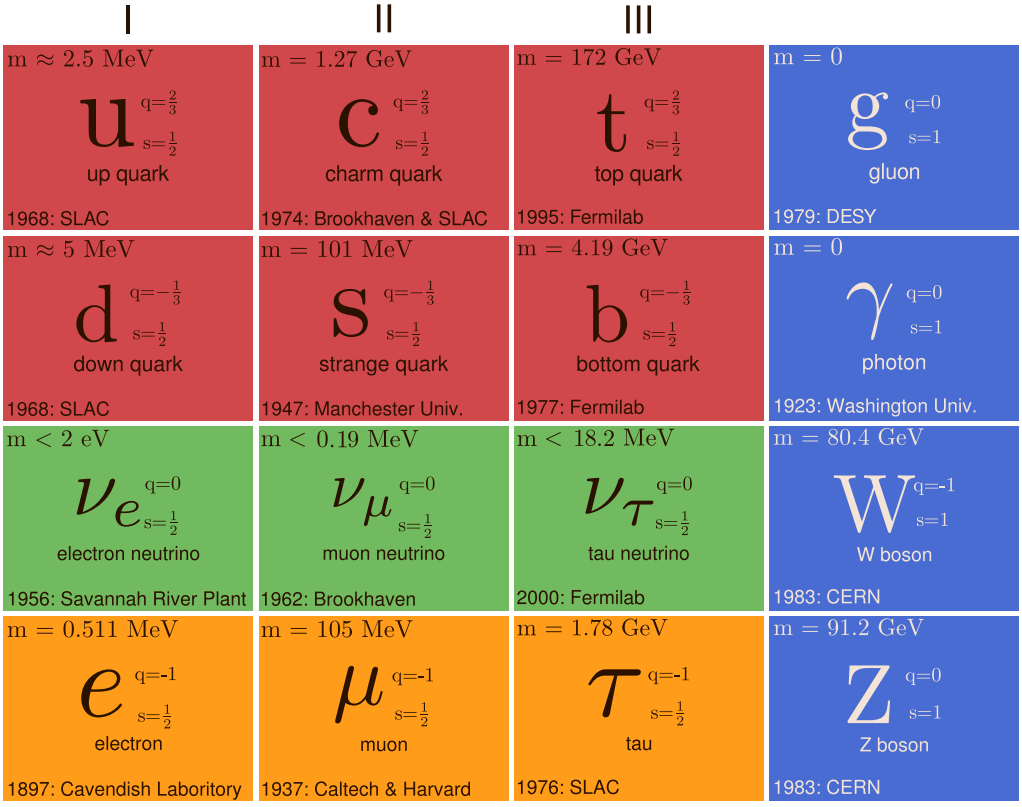

Figure 2.1: Particles of the Standard Model. Properties taken from [2] and information on the discoveries from [3]. The electric charge q is given in units of the elementary charge e=1.602·10^{-19} C. Although many experiments contributed to the discovery of the photon, this figure list the Compton effect as proof for the quantization of light [4].

2.1 The Particle Content

The Standard Model differentiates between two basic types of particles: fermions with half-integer spin and bosons with an integer spin. Fermions make up the visible matter, whereas bosons act as mediators of the forces between them.

Fermions are again divided into 6 quarks and 6 leptons, depending on whether they take part in the strong force or not. As indicated by roman numerals in figure 2.1, three generations can be assigned to these 12 particles. Each generation holds a quark and a lepton doublet. Corresponding particles from the three generations have the same quantum numbers, their mass increases from one generation to the next higher one. Aside from neutrinos, the second and third generation fermions are not stable and decay into first generation fermions. Thus the universe around us is mainly built from electrons and up and down quarks.

Neutrinos are assumed to be massless and stable within the Standard Model. Experiments measuring the flavor of e.g., solar neutrinos [5] [6] have given evidence of oscillations between the three generations. This results in non-zero masses. The electron neutrino mass given in figure 2.1 is an upper limit attained from the β decay of tritium. Whereas the muon neutrino mass is measured from the $\pi^+ \to \mu^+\nu$ decay and the tau neutrino decay is evaluated from τ^- decays [2].

The energy of a free particle can be deduced from the following relativistic equation, relating its energy to its momentum:

$$E^2 - \vec{p}^2 = m^2. \tag{2.1}$$

Solving for E gives a positive and a negative solution. The former describes the fermions listed above. The second solution introduces the notion of antimatter. Every particle has a corresponding antiparticle with the same mass and spin. The additive quantum numbers such as the electric, color or weak charge take on the inverse value. For some particles, like the photon, all additive quantum numbers are zero, so particle and antiparticle are identical.

2.2 The Fundamental Interactions

Apart from particles and their properties the Standard Model also describes the forces they interact with, namely: the electromagnetic, weak and strong force. In quantum field theory these interactions can be characterized as fields. The mediators can be deduced from a local gauge invariance of the Dirac Lagrangian of a free spin $\frac{1}{2}$ particle:

$$\mathcal{L} = \bar{\psi}\left[i\gamma^\mu \partial_\mu - m\right]\psi, \tag{2.2}$$

where ψ refers to particle field and ∂_μ symbolizes the derivative of time and the three spacial coordinates. γ^μ are 4x4 matrices satisfying the relation $\{\gamma^\mu, \gamma^\nu\} = 2g^{\mu\nu}\mathbb{1}$ with the Minkowski metric $g^{\mu\nu}$. The fermion's mass is denoted by m. To ensure this equation is invariant under a transformation:

$$\psi(x) \longrightarrow \psi'(x) = e^{igT_a\Theta^a(x)} \tag{2.3}$$

a local gauge field $A(x)$ needs to be added, which introduces a massless gauge boson with spin 1. A transformation of this kind can be mathematically described by a symmetry group. Here g is the coupling constant and T_a are the generators of the symmetry group. For all three Standard Model forces the elements of these groups are complex $n \times n$ matrices. They are either unitary $U(1)$ i.e., their inverse is equal to the transpose conjugate, or $SU(n)$ matrices. In both cases the matrices have a determinant of 1.

Due to the particles' small masses, the influence of the gravitational force is negligible compared to the other forces that will be described in the following. In the classical sense gravity is described by Newton's law of universal gravitation. For relativistic velocities and high energies Einstein's theory of general relativity gives an explanation for gravitational effects. A consistent quantum

mechanical theory has not been developed yet. If one chooses the framework of quantum field theory the graviton is considered to be the mediating boson. So far no experimental evidence has been found to prove its existence.

2.2.1 The Electromagnetic Force

The electromagnetic force is derived within the theory of quantum electrodynamics (QED) and described by the $U(1)_{QED}$ symmetry group. The photon is revealed as the massless quantum of a field with infinite range. All particles carrying electric charge i.e., quarks, electrons, muons, taus and the W boson, couple to the photon. Since the photon itself is neutral, self-coupling does not occur at tree-level and the potential shows a $\frac{1}{r}$ dependency. The electromagnetic force conserves its charge as well as the lepton number i.e., a muon cannot decay into another lepton via a QED process.

2.2.2 The Weak Force

The β decay of nucleons is a common example of a process mediated by the weak force. It exhibits the charged component of this interaction, the W^+ and W^- bosons. They couple to left-handed fermions and right-handed antifermions. This behavior is characterized by a $SU(2)_L$ gauge group, accompanied by the *weak isospin* T and its third component T_3. This quantum number assigns left-handed fermions to doublets with $T_3 = \pm\frac{1}{2}$ and right-handed fermions to singlets with $T_3 = 0$. The gauge group introduces three massless gauge bosons. Linear combinations of W^1 and W^2 result in the observed W^+ and W^- bosons. The charged weak interaction of the SM is defined as lepton number conserving i.e., an electron and a electron neutrino result from a β^- decay, neutrino oscillations are not taken into account. The quark number conservation, however, is violated by the charged component of the weak force. This so called quark mixing is described by the 3×3 CKM-matrix[1] that can only be determined experimentally.

Apart from the charged current described above, a second type of weak interaction, the neutral current mediated by the Z^0 boson appears in weak processes. The Z^0 couples to all fermions and cannot change their flavor.

Within the GSW-model[2] of electroweak interaction a $SU(2)_L \times U(1)_Y$ symmetry group is introduced, which leads to an additional gauge boson referred to as B. Moreover it defines the *weak hypercharge* $Y = 2(q - T_3)$ as a combination of the electric charge q and the third component of the weak isospin T_3. Linear combinations of the B and W^3 boson introduced above are revealed to be the photon of QED and the neutral Z^0 boson. So in total there are four gauge bosons of the unified electroweak force:

$$W^+ = (W^1 + W^2)/\sqrt{2} \tag{2.4}$$

$$W^- = (W^1 + W^2)/\sqrt{2} \tag{2.5}$$

$$Z^0 = -B \cdot \sin\theta_w + W^3 \cos\theta_w \tag{2.6}$$

$$\gamma = B \cdot \cos\theta_w + W^3 \sin\theta_w, \tag{2.7}$$

where θ_w is known as the *weak mixing* or *Weinberg angle* and is a free parameter.

As will be described in section 2.3 the W and Z bosons acquire their masses via the Higgs mechanism. Being measured to m_W=80.399 ± 0.023 GeV and m_Z=91.1876 ± 0.0021 GeV [2], one can understand that the range of the weak force cannot be large, it is in fact only about 10^{-17} m. Furthermore particles that decay via the weak interaction have a long lifetime i.e., from about 10^{-15} s for the tau to approximately 15 min for the neutron.

[1] **C**abibbo-**K**obayashi-**M**askawa
[2] **G**lashow-**W**einberg-**S**alam

2.2.3 The Strong Force

Over the course of research in high energy physics more particles, often heavier than the ones listed in figure 2.1, were discovered. These so called hadrons are composite particles of quarks. They only appear in groups of two (quark and antiquark) or three quarks, called mesons and baryons respectively. The following section will give an explanation for this.

In quantum chromodynamics (QCD) the strong force is described by the $SU(3)_{QCD}$ gauge group. A color charge is introduced which can take on three values referred to as: red (r), green (g) and blue (b). All quarks are assigned a color and take part in the strong interaction. The field quanta are eight gluons, each carrying a color and an anti-color. They couple to the 18 quarks and also to each other.

The gluon self-coupling implies that the field does not have a simple $\frac{1}{r}$ dependency as is the case in QED. At large distances the force becomes constant. This is reflected in the so called *running* of the strong coupling constant α_s. In fact a running can be observed for all three SM couplings. At short distances α_s is small and quarks can be characterized as free particles, the so called *asymptotic freedom*. At distances of about the size of a hadron, i.e. 10^{-15} m, enough energy has been accumulated to produce new pairs of colored particles. The fact that a single colored particle cannot be isolated is known as *confinement*. Only neutral combinations of either color and anti-color i.e., mesons, of combinations of all three colors i.e., baryons, are possible.

Apart from the so called valence-quarks that determine the quantum numbers, a baryon is also composed of see-quarks and a gluon field. More details on the proton's substructure will be given in section 5.6.1.

In a detector at a hadron collider the experimental signatures of quarks are collimated bunches of colorless hadrons, so called jets. They are the result of fragmentation and hadronization processes. Quarks produced in the collision radiate gluons, which induce the so called *parton shower*. This in turn initiates additional quarks, building collections of hadrons.

2.3 The Higgs Sector

The Standard Model as described above fails to answer the fundamental question of the origin of the particles' masses. Inserting mass terms by hand leads to a breaking of the gauge invariance. The Higgs mechanism is an attempt to extend the current theory to incorporate this. The search for the Higgs boson is an open field of modern day particle physics.

The necessity for an addition in SM arises if one examines the local gauge invariance of the electromagnetic, strong and weak interaction. As stated above this introduces massless gauge bosons. For the electromagnetic and strong interaction the photon and gluons have indeed been found to possess a mass of zero, but the W and Z bosons of the weak interaction are far from being massless. To solve this discrepancy a principle called spontaneous symmetry breaking is applied, which introduces a massive scalar particle, the Higgs boson, and a massive gauge field. By coupling to this field all fermions, as well as the W and Z bosons acquire their mass. The photon and gluon do not couple to the Higgs field and thus remain massless.

Unfortunately the mass of the Higgs boson is not predicted within the theory, but constraints can be made with the help of electroweak precision measurements. Moreover theoretical arguments concerning the triviality bound of the Higgs self-coupling and the stability bound of the Higgs couplings to fermions and vector bosons deliver upper and lower bounds on the Higgs mass [7]. Direct searches have been performed at the LEP[3] collider, leading to the exclusion of a mass smaller than 114.4 GeV [8]. Furthermore, recent results from Tevatron [9] have excluded a region of 156 to 177 GeV. At the LHC a combined Higgs search at CMS [10] has set exclusions limits from 149 to 206 GeV and from 300 to 440 GeV. The ATLAS detector has reported limits from 155

[3] **L**arge **E**lectron **P**ositron

to 190 GeV and from 295 to 450 GeV [11]. All these exclusions together constrain the Higgs boson mass to:

$$114.4\,\text{GeV} < m_H < 149\,\text{GeV}, \qquad 206\,\text{GeV} < m_H < 295\,\text{GeV}, \qquad m_H > 450\,\text{GeV},$$

at 95% C.L.

2.4 Unresolved Issues

Over the past decades the Standard Model has shown to be a satisfying description of the particles and their interactions. It predicted the existence of several particles e.g., the Z^0 boson and the top quark, and withstood precision measurements at the LEP collider. Still it does not cover all questions of modern day particle physics such as the values of the fermion masses or the gravitational force, as already indicated above. Further unresolved observations and theoretical problems lead to the assumption that the Standard Model is but the low energy realization of a more general theory. Some of the indications for new physics at the electroweak scale of about 100 GeV to 1 TeV will be outlined in the following section. The theory of supersymmetry will be introduced as a possible solution to these open questions in chapter 3.

2.4.1 The Hierarchy Problem

When calculating the physical mass of the Higgs boson m_H one-loop quantum corrections Δm_H of scalar particles must be taken into account. The measurable Higgs boson mass squared is determined by [12][13]:

$$m_H{}^2 = m_H^0{}^2 + \Delta m_H{}^2, \tag{2.8}$$

where m_H^0 is the bare mass i.e., the mass of the scalar field appearing in the Lagrangian. The corrections are proportional to the respective gauge coupling constant λ and also to the energy scale Λ at which new physics comes in:

$$\Delta m_H{}^2 \propto \frac{\lambda^2}{16\pi^2} \cdot \Lambda^2. \tag{2.9}$$

Setting the energy scale to the Planck scale $M_P \sim 10^{19}\,\text{GeV}$ results in a very large correction. An assumed Higgs boson mass in the order of 100 GeV can only be achieved if the bare mass is accurate to over 30 orders of magnitude.

To evade this extreme *fine-tuning* one would need additional corrections of approximately the same size of the bosonic loops but of the opposite sign. Fermionic loops fulfill the requirement of a negative contribution, yet the Standard Model presents a fairly large difference between the number and masses of fermions and bosons. Thus only an exact symmetry between all fermions and bosons of the SM would lead to a complete cancellation.

2.4.2 Dark Matter

Recent measurements of cosmic microwave background by WMAP[4] have once again confirmed that our universe is made up of only about 4% baryonic matter [14], the constituents of all visible stars and planets around us. At about 73% dark energy has the largest contribution to the universe's energy density. This form of energy is introduced in the theory of cosmology analogous to the cosmological constant and incorporates the expansion of the universe. The remaining 22% are non-luminous dark matter. Its existence was suggested by the unexpected flat behavior of

[4] **W**ilkinson **M**icrowave **A**nisotropy **P**robe

galactic rotation curves [15]. This can be explained by a spherical halo of otherwise undetected matter outside of the visible part of the galaxy.

To comply with the observed structures of the universe, dark matter is assumed to be *cold* i.e., non-relativistic during the formation of galaxies and clusters[16]. WIMPS[5] are among the candidates for cold dark matter. Many experiments are dedicated to the search for these particles e.g., [17][18]. As will be explained in the following chapter, supersymmetry potentially provides a particle to fulfill the criteria for cold dark matter.

2.4.3 Grand Unification

Grand Unified Theories (GUT) joining the electroweak and strong force are greatly favored, having the potential of reducing the number of free parameters in the SM and possibly leading to a superior theory. The curious fact that the $SU(3) \times SU(2) \times U(1)$ symmetry group of the SM can be incorporated in the $SU(5)$ leads to theories based on this gauge group [13].

As indicated in the previous sections all three coupling constants of the Standard Model are subject to a running, depending on the energy scale Q. In the Standard Model the α_i do not unify at any given scale, which is shown by the dashed lines in figure 2.2.

Adding new particles to the theory will introduce more loop corrections. This will change the slope of the α_i lines at the mass scale of the new particles, leading to a possible gauge coupling unification. A realization of this in the MSSM[6] which will be introduced in section 3.2 is shown in figure 2.2 by red and blue lines. They represent the maximum values of a variation of the new particle's masses and of the value of the strong coupling constant at the Z^0 boson mass [19].

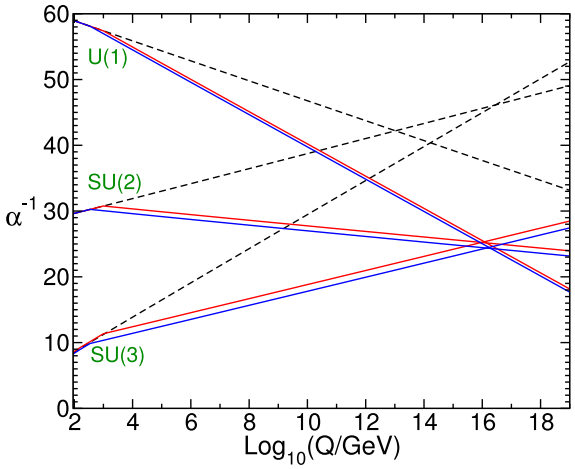

Figure 2.2: Running of the three coupling constants in the SM (dashed lines) and in the supersymmetric extension MSSM (solid lines). A unification can only be achieved in the second case. Blue and red lines represent variations of input parameters, see text for further explanations. Taken from [20]

The additional particles must have masses high enough to avert the proton decay but small enough to refrain from causing a new hierarchy problem.

[5] **W**eakly **I**nteracting **M**assive **P**articles
[6] **M**inimal **S**upersymmetric **S**tandard **M**odel

Chapter 3

Introduction to Supersymmetry

After offering the hierarchy problem, the existence of dark matter and a possible grand unification of the SM forces as motivations for a symmetry between bosons and fermions, the following chapter will introduce precisely this symmetry, the so called supersymmetry. Starting with a short description of the new symmetry group, the so called Minimal Supersymmetric extension of the Standard Model (MSSM) will be introduced in section 3.2, doubling the particle content of the Standard Model. A possible method to perform a necessary breaking of the symmetry will be outlined in section 3.3 and constrained by a new quantum number, the R-parity, in section 3.4. This leads to a five dimensional parameter space constrained by only few restrictions from theory and previous experiments.

To facilitate the comparison of results from different searches for supersymmetry a set of benchmark points was introduced in the high-energy physics community and are the subject of section 3.5. For a better understanding of the new particles' properties their mass spectrum, production at hadron colliders and decay channels will be discussed in sections 3.5.2 through 3.5.3.

3.1 A New Symmetry

The Coleman-Mandula no-go theorem states that new symmetries can only be added to the theory, if their generators commute with the existing ones of the Standard Model Poincaré group [21]. Fortunately, the theorem itself offers a loophole: it is only proven for bosonic generators. A fermionic generator Q can be used to introduce a new global symmetry that provides non-zero commutators with the Standard Model generators [19]:

$$Q\,|boson\rangle = |fermion\rangle \qquad Q\,|fermion\rangle = |boson\rangle\,. \tag{3.1}$$

Applying this symmetry to a quantum field theory with chiral i.e., left and right-handed, fermions like the Standard Model one can derive an algebra in which the new generator Q commutes with the SM generators of space time translations, but not with generators of Lorentz transformations [13]. For the case of only one SUSY generator left and right handed fermions are kept in separate states of the new field and will not lead to problems under $SU(2)$ gauge transformations. Higher dimensional theories are possible, but since they combine the chiral fermions, must take place at high energies. They cannot be the desired low-energy extension of the Standard Model at about 1 TeV.

This new symmetry, transforming bosonic into fermionic states and vice versa, is known as supersymmetry. It is the only possible non-trivial addition to the Poincaré group, aside from adding more gauge groups. SUSY can solely be brought into existence by adding new particles. How this can be achieved will be outlined in the next section.

3.2 The Minimal Supersymmetric Standard Model

Within the minimal supersymmetric extension of the Standard Model every particle is associated with precisely one superpartner, as shown in table 3.1. In each pair all particle properties (apart from the mass which will be discussed in the section 3.3) are identical, only the spin differs by a

factor of 1/2. A naming scheme is introduced for the new particles. Fermions receive a prefix s- for scalar and are named e.g., selectron, sneutrino and squark. Bosons gain an additional suffix -ino and are summarized as gauginos. Sparticles are denoted by an additional tilde as superscript and anti-sparticles often receive an asterisk instead of using the usual 'bar' notation.

The slepton sector shows a mixing of the chiral states that is proportional to the lepton mass. Thus it is large for stops, sbottoms, staus and stau neutrinos. As indicated in table 3.1 mixing of the first two generation sfermions is small and can generally be set to zero.

In the MSSM additional Higgs bosons are needed to ensure the correct electroweak breaking. Two Higgs doublets are proposed: one gives mass to the up-type quarks and the other does likewise to the down-type quarks and charged leptons. This leads to five massive Higgs bosons, of which the lightest h_0 can be associated with the SM Higgs boson [19].

Looking closely at table 3.1, one sees that the gauge bosons are not doubled in their mass eigenstates but in their gauge eigenstates, resulting in Binos, Winos, gluinos and Higgsinos. The counterparts of the electroweak bosons mix with the Higgsinos to form several observable charginos $\widetilde{\chi}^{\pm}$ and neutralinos $\widetilde{\chi}^{0}$. The role of the gravitino and goldstino, listed in table 3.1 for the sake of completion, will be explained in the following section.

	Spin	R	Gauge Eigenstates	Mass Eigenstates
Higgs bosons	0	+1	$H_u^0\ H_d^0\ H_u^+\ H_d^-$	$h^0\ H^0\ A^0\ H^{\pm}$
squarks	0	-1	$\widetilde{u}_L\ \widetilde{u}_R\ \widetilde{d}_L\ \widetilde{d}_R$ $\widetilde{c}_L\ \widetilde{c}_R\ \widetilde{s}_L\ \widetilde{s}_R$ $\widetilde{t}_L\ \widetilde{t}_R\ \widetilde{b}_L\ \widetilde{b}_R$	- - $\widetilde{t}_1\ \widetilde{t}_2\ \widetilde{b}_1\ \widetilde{b}_2$
sleptons	0	-1	$\widetilde{e}_L\ \widetilde{e}_R\ \widetilde{\nu}_e$ $\widetilde{\mu}_L\ \widetilde{\mu}_R\ \widetilde{\nu}_\mu$ $\widetilde{\tau}_L\ \widetilde{\tau}_R\ \widetilde{\nu}_\tau$	- - $\widetilde{\tau}_1\ \widetilde{\tau}_2\ \widetilde{\nu}_\tau$
neutralinos	1/2	-1	$\widetilde{B}^0\ \widetilde{W}^0\ \widetilde{H}_u^0\ \widetilde{H}_d^0$	$\widetilde{\chi}_1^0\ \widetilde{\chi}_2^0\ \widetilde{\chi}_3^0\ \widetilde{\chi}_4^0$
charginos	1/2	-1	$\widetilde{W}^{\pm}\ \widetilde{H}_u^+\ \widetilde{H}_d^-$	$\widetilde{\chi}_1^{\pm}\ \widetilde{\chi}_2^{\pm}$
gluino	1/2	-1	$\widetilde{g}$	-
goldstino (gravitino)	1/2 (3/2)	-1	$\widetilde{G}$	-

Table 3.1: The particle content of the MSSM as given in [19]

3.3 Supersymmetry Breaking

The fact that no selectron has been discovered with the mass of the electron leads to the assumption that SUSY is not a true symmetry of nature and must be broken by some means. At the same time it would be desirable to preserve the features of the MSSM that solve the hierarchy problem and lead to a GUT. This can only be sustained if the coupling constants of broken and unbroken supersymmetry have the same relationship to the couplings of the Standard Model.

The so called *soft* breaking of supersymmetry precisely fulfills the needs mentioned above. One divides the effective Lagrangian of the MSSM into two parts [19]:

$$\mathcal{L} = \mathcal{L}_{SUSY} + \mathcal{L}_{soft}. \tag{3.2}$$

The first one contains all terms needed to preserve SUSY under transformations i.e., all gauge and Yukawa couplings. The second one breaks SUSY but does not introduce new quadratic divergences.

Quite in contradiction to the general desire of minimizing the number of free parameters within the theory of particle physics, breaking of the MSSM contributes 105 additional parameters to the 19 unknown parameters of the Standard Model [13].

Similar to the Higgs mechanism described in section 2.3 one believes SUSY to be broken spontaneously. The Lagrangian density is invariant under the supersymmetric transformation, while the vacuum state introduces a new gauge field and new particle. For the case of a globally broken supersymmetry a massless *goldstino* appears with the same quantum numbers as the generator being broken i.e., spin-1/2. If one defines a local supersymmetry breaking gravity must be included, thus coined *supergravity* [13]. In terms of particles this manifests itself in a massive graviton and its superpartner the spin-3/2 gravitino, which acquires its mass by absorbing the goldstino.

Phenomenological constraints of the sparticle spectrum do not allow a breaking of SUSY with the MSSM particle content. Nor does adding supermultiplets at the electroweak scale explain the breaking, since tree-level couplings inducing gaugino masses are prohibited by renormalization [19]. This leads to a *hidden sector* of particles unaffected by the SM gauge group, in which the breaking can take place. In the theory of supergravity the gravitino then acts as a mediator between the hidden sector and the visible sector.

The minimal supergravity model mSUGRA combines the particle content of the MSSM with gravity mediated symmetry breaking. If one assumes a unification of several quantities at the GUT scale the number of free parameters can be reduced from 105 to five [19]:

- m_0: unified mass of the scalar sparticles at the GUT scale
- $m_{1/2}$: unified mass of the gauginos at the GUT scale
- A_0: unified trilinear sfermion-sfermion-Higgs coupling at the GUT scale
- $\tan\beta = \frac{\langle H_u^0 \rangle}{\langle H_d^0 \rangle}$: ratio of the neutral Higgs vacuum expectation values at the electroweak scale
- $sign(\mu)$: sign of the unified Higgsino mass term at the electroweak scale

The unification of gaugino masses is initialized by setting the three couplings M_i to a joined value at the GUT scale. Figure 3.1 shows an example of how the values of m_0, $m_{1/2}$ and the Higgs mass parameter can be evolved from the GUT scale of about 10^{16} GeV down to the electroweak scale defined by the Higgs vacuum expectation value of about 174 GeV.

3.4 R-Parity

The new couplings of the MSSM introduce lepton (L) and baryon (B) number violating processes. To avoid this one can define a new multiplicative quantum number, relating both quantities to each other [13]:

$$R = (-1)^{3B+L+2S}. \tag{3.3}$$

This is known as R-parity, being +1 for fields of the Standard Model and -1 for their supersymmetric versions as shown in table 3.2.

R-parity conservation is by no means a necessary requirement of the supersymmetric theory. Models in which R-parity is violated (RPV SUSY) have been developed and must include upper bounds on the RPV couplings to ensure a proton lifetime that is long enough to agree with the experimental measurements.

In case of R-parity conservation sparticles can only be produced in pairs, since they are initiated by ordinary matter with R=+1. The final state of a SUSY decay includes an even number of the stable lightest supersymmetric particles (LSPs). Assuming that all sparticles produced during the Big Bang have decayed into the LSP, a large amount of these sparticles would be spread out over

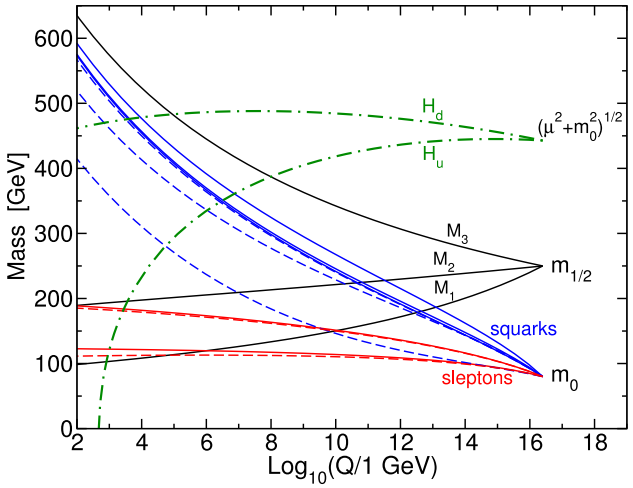

Figure 3.1: Evolution of the scalar masses, gaugino couplings M_i and values appearing in the Higgs potential from the GUT scale down to the electroweak scale. Electroweak symmetry breaking is indicated by negative values of H_u [19].

Field	L	B	s	R
Quark	0	1/3	1/2	$(-1)^2 = +1$
Squark	0	1/3	0	$(-1)^1 = -1$
Lepton	1	0	1/2	$(-1)^2 = +1$
Slepton	1	0	0	$(-1)^1 = -1$

Table 3.2: Summary of the lepton (L) and baryon (B) number, as well as the spin s and the resulting R-parity for particles and sparticles. Adapted from [13].

the entire universe. As will be indicated in section 3.5.2 the lightest neutralino is the LSP in many MSSM models. It carries no electric or color charge and represents a prime WIMP candidate for dark matter.

3.5 Benchmark Models

In order to facilitate the comparison of results from different experiments, benchmark points have been introduced in the five dimensional mSUGRA parameter space in regions that have not yet been excluded experimentally. CMS has introduced a group of so called low-mass points (LM) with fairly high cross sections and small sparticle masses, as well as additional high-mass points (HM) with rather low cross sections.

During the first year of running the LHC not enough data were collected to possibly find sparticles in the high-mass regions. Accordingly, this thesis uses LM0 and LM1 as reference points to build up an analysis strategy. Final results will be generalized to the $m_0 - m_{1/2}$-plane. The properties of LM0 and LM1 are given in table 3.3 as well as the low-mass points up to LM9 for the sake of comparison. In all scenarios the χ_1^0 is the LSP and its mass is also given in table 3.3.

Figure 3.2 displays all LM and HM points in the $m_0 - m_{1/2}$-plane for $\tan\beta$=10, A_0=0, μ >0. Although not all of these points have the same values of $\tan\beta$, A_0 and $sign(\mu)$, they are still shown in one plane to give a general impression of how they depend on m_0 and $m_{1/2}$. As will be shown later, the sparticle masses are a function of these two values. An additional set of benchmark points

not discussed here is also included in the figure [22]. Exclusions based on theoretical considerations are shown and represent the region where the stau would be the LSP and where no electroweak symmetry breaking would occur.

Benchmark points LM1, LM2 and LM6 are motivated by limits on cold dark matter set by WMAP and strictly follow the mSUGRA scenario. LM0 was introduced as a point close to the Tevatron bound. The other low mass points were chosen in a model without unified Higgs masses and where the gravitino is a LSP candidate [23].

Model	$\sigma(\sqrt{s}=7\,\text{TeV})$	$m(\tilde{\chi}_1^0)$ [GeV]	m_0 [GeV]	$m_{1/2}$ [GeV]	A_0 [GeV]	$\tan\beta$	sign(μ)
LM0	38.9 pb	60	200	160	-400	10	+
LM1	4.89 pb	96	60	250	0	10	+
LM2	0.60 pb	141	185	350	0	35	+
LM3	3.44 pb	94	330	240	0	20	+
LM4	1.88 pb	112	210	285	0	10	+
LM5	0.47 pb	144	230	360	0	10	+
LM6	0.31 pb	161	85	400	0	10	+
LM7	1.21 pb	94	3000	230	0	10	+
LM8	0.73 pb	120	500	300	-300	10	+
LM9	7.13 pb	65	1450	175	0	50	+

Table 3.3: Properties of the CMS low-mass bechmark points as listed in [24]. The LSP mass was calculated using SOFTSUSY [25] for the spectrum and SUSYHIT [26] to simulate the decay, the respective output files can be found at [27]. The cross sections are given at leading order.

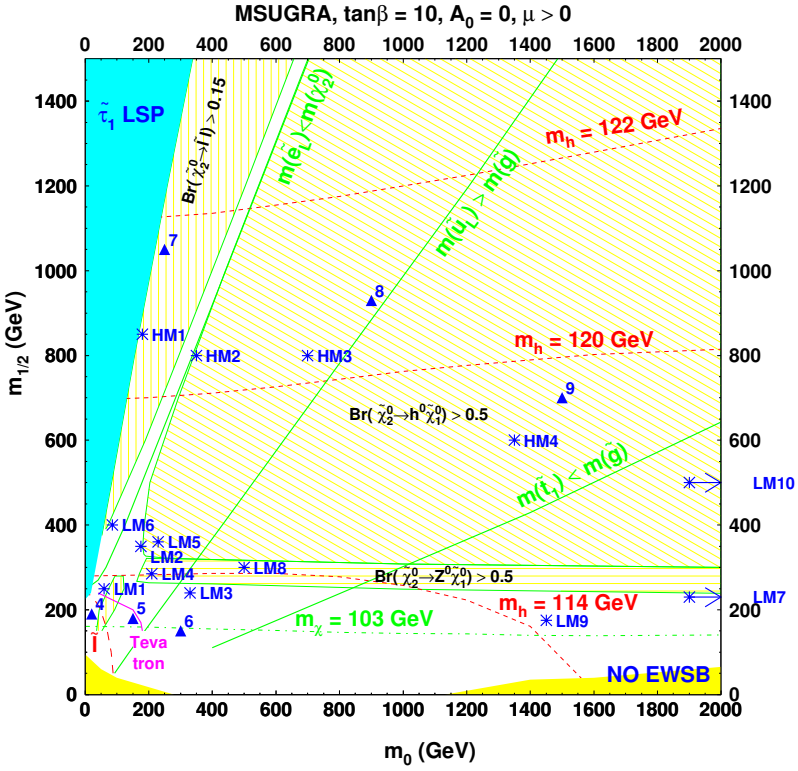

Figure 3.2: The CMS low (LM) and high mass (HM) benchmark points are indicated by blue stars in the $m_0 - m_{1/2}$-plane. Triangles represent a further set of points not discussed here. Some exclusions from theory and searches are also shown [28].

3.5.1 Production at Hadron Colliders

The production of sleptons, charginos and neutralinos at a proton-proton collider is mediated by the electroweak force. The following processes can occur at tree-level [19]:

$$q\bar{q} \to \widetilde{\chi}_i^+ \widetilde{\chi}_j^-, \quad \widetilde{\chi}_i^0 \widetilde{\chi}_j^0, \quad \tilde{l}_i^+ \tilde{l}_j^-, \quad \tilde{\nu}_l \tilde{\nu}_l^* \tag{3.4}$$

$$q\bar{q}' \to \widetilde{\chi}_i^\pm \widetilde{\chi}_j^0, \quad \tilde{l}_L^\pm \tilde{\nu}_l^{(*)}. \tag{3.5}$$

Furthermore chargino/neutralio-squark pairs can be produced via quark-gluon fusion:

$$gq \to \tilde{q}\widetilde{\chi}^0, \quad \tilde{q}'\widetilde{\chi}^\pm. \tag{3.6}$$

Gluino and squark production via gg or gq fusion are usually the dominant processes for LM0 and LM1. They are mediated by the strong force in the following fashion:

$$gg/q\bar{q} \to \tilde{g}\tilde{g}, \quad \tilde{q}_i \tilde{q}_j^* \tag{3.7}$$

$$gq \to \tilde{g}\tilde{q} \tag{3.8}$$

$$qq \to \tilde{q}_i \tilde{q}_j. \tag{3.9}$$

Via a t-channel squark-exchange gluinos can also be produced together with a chargino or neutralio:

$$qq \to \tilde{g}\widetilde{\chi}^0 \tag{3.10}$$

$$qq' \to \tilde{g}\widetilde{\chi}^\pm. \tag{3.11}$$

As can be seen in figure 3.3 the LM0 benchmark point follows a production hierarchy of:

$$\sigma(\tilde{g}\tilde{q}^{(*)}) > \sigma(\tilde{q}\tilde{q}^*) > \sigma(\tilde{q}^{(*)}\tilde{q}^{(*)}) > \sigma(\tilde{g}\tilde{g}).$$

Similar hold to be true for LM1. The sparticle mass spectrum of these points will be discussed in the following section. Other benchmark points can exhibit a very different structure, with stronger contributions from $\widetilde{\chi}\widetilde{\chi}$ and $\tilde{g}\tilde{g}$. A summary of the production channels in benchmark points LM0-LM9 can be found in [24].

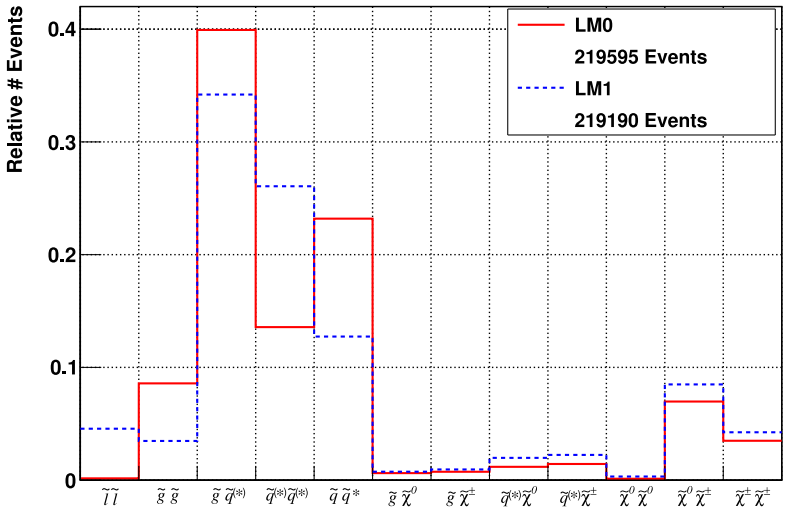

Figure 3.3: Comparison of LM0 and LM1 production channels used in this thesis. The histograms have been normalized to area, the absolute number of generated events is given in the legend.

3.5.2 Mass Spectrum

As already suggested in section 3.4, all sparticle decays end with the lightest supersymmetric particle if R-parity is conserved. The question that arises is which sparticle has the smallest mass. One strong argument is that no sparticle has ever been seen, so the stable LSP cannot be electrically charged or interact via the strong force. The gravitino is ruled out as LSP in mSUGRA models, since it is the heaviest sparticle. The sneutrino was excluded as a potential candidate at the LEP collider [29]. This leaves only the lightest neutralino $\widetilde{\chi}_1^0$ to fulfill the function of LSP.

In the mSUGRA model the gaugino masses at the electroweak scale can be approximated to [28]:

$$M_{\widetilde{B}^0} \simeq 0.4 \cdot m_{1/2} \tag{3.12}$$

$$M_{\widetilde{W}^\pm} \simeq 0.8 \cdot m_{1/2} \tag{3.13}$$

$$M_{\widetilde{g}} \simeq 2.7 \cdot m_{1/2} \tag{3.14}$$

by running down the unified masses at the GUT scale via Renormalization Group Equations. Similarly the scalar masses of the first two sfermion generations can be determined as functions of m_0 and $m_{1/2}$:

$$m_{\tilde{f}} \simeq {m_0}^2 + a \cdot {m_{1/2}}^2 + c, \tag{3.15}$$

where a is a constant ranging from 0.15 for the right-handed selectron to 5.0 for the left-handed up squark. The term c depends on $\cos 2\beta \cdot M_Z$ and a constant multiplicative factor taking on values between -0.42 and +0.50. These relations cannot be applied to sfermions of the third generation, due to the strong mixing of their chiral states.

The mass spectrum for benchmark points LM0 and LM1 is shown in figure 3.4. It depicts the invariant masses of the sparticles produced in the hard interaction. The Monte Carlo samples used for both benchmark points are listed in table 5.1 of section 5.2. In both scenarios the $\widetilde{\chi}_1^0$ can be identified as the LSP at about 60 GeV and 96 GeV, respectively. For the case of LM1 the gluino is the heaviest sparticle with a mass of about 603 GeV. Moreover, squarks show to be generally heavier than sleptons. The gravitino is not shown as it is only included in the simulation of gauge-mediated SUSY breaking, where it is the LSP [30].

In figure 3.4 red crosses indicate the on-shell mass of the respective sparticle. The width of each mass distribution is calculated with the program SDECAY [31] and corresponds to the gamma parameter of the relativistic Breit-Wigner distribution [30].

Looking at the mass spectrum of the gluino, one can see that it is not symmetric around the on-shell mass (marked by a red cross). It stops abruptly at a minimal mass of about 360 GeV for LM0 and 515 GeV for LM1. As will be explained in section 3.5.3, this results from kinematic restrictions on the gluino decay.

3.5.3 Decays

A typical signature of supersymmetric events are long decay chains. The sparticles produced in the hard-scattering cascade down to the LSP. The topology can therefore contain several jets, leptons and a large amount of missing energy. To understand the individual steps of the cascade, each sparticle's main decay modes are summarized in the following.

Squarks will decay dominantly via $\tilde{q} \to q\tilde{g}$, if they are heavier than the gluino. Otherwise, a decay into quark and chargino or neutralino will occur.

Sleptons can decay into lepton and chargino or neutralino: $\tilde{l} \to l\widetilde{\chi}$. This includes direct decays to the LSP, as well as intermediate decays to the heavier charginos and neutralinos.

Gluinos carry only the color charge, hence the sole decay is into squark-quark pairs: $\tilde{g} \to \tilde{q}q$. This can take place as a two-body decay if a the sum of the squark and quark masses is smaller than the gluino mass. If this is not given a decay via an off-shell squark: $\tilde{g} \to q\tilde{q}^{virt} \to qq^{(\prime)}\widetilde{\chi}$ is also possible.

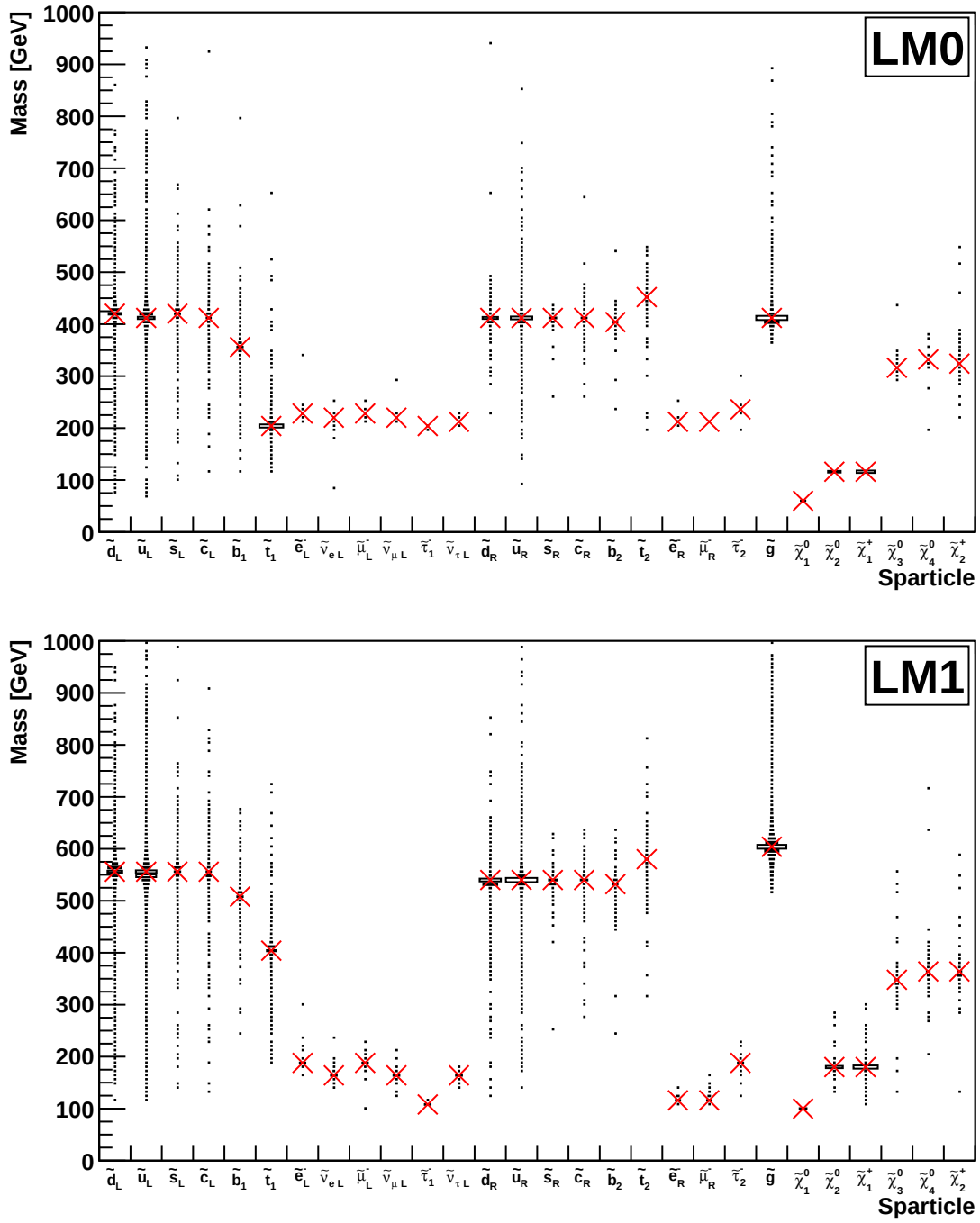

Figure 3.4: LM0 and LM1 mass spectrum of the two produced sparticles. Red crosses indicate the bin with the largest number of entries, i.e. the on-shell mass of each sparticle.

The program SDECAY [31] is used in the process of producing the SUSY benchmark models considered in this thesis. Due to the way this program is configured, the gluino decays via off-shell squarks are completely suppressed if the two-body decays are kinematically open, since they would only play a very minor role. This is the case for the LM0 and LM1 points and explains the shape of gluino mass spectrum in figure 3.4. For the example of LM0 the gluino must be heavier than the on-shell mass of $\tilde{b}_1$ and bottom quark combined. All other combinations of squark and the

corresponding quark require the gluino to have a higher invariant mass. For benchmark points such as LM7 and LM9 the on-shell mass of the gluino is about 400 GeV smaller than that of the lightest squark $\tilde{t}_1$. In these cases the three-body decays are the only possibility and they are included by SDECAY.

Charginos and neutralinos inherit the weak coupling from the superpartners of the $SU(2)_L \times U(1)_Y$ gauge bosons. Consequently, they can decay into either $\tilde{l}l$ or $\tilde{q}q$ pairs, where the former is favored since sleptons are generally lighter than squarks. Decays to lighter charginos/neutralinos plus scalar Higgs or electroweak gauge bosons are also possible. If all of these channels are forbidden, especially for the lighter $\widetilde{\chi}$, three body decays with virtual gauge bosons can take place.

Figure 3.5 shows an example of a supersymmetric decay chain from the LM0 scenario. The topology of the event fulfills the search criteria of this thesis. Gauginos are represented by a double wavy line and sfermions are shown by two straight lines.

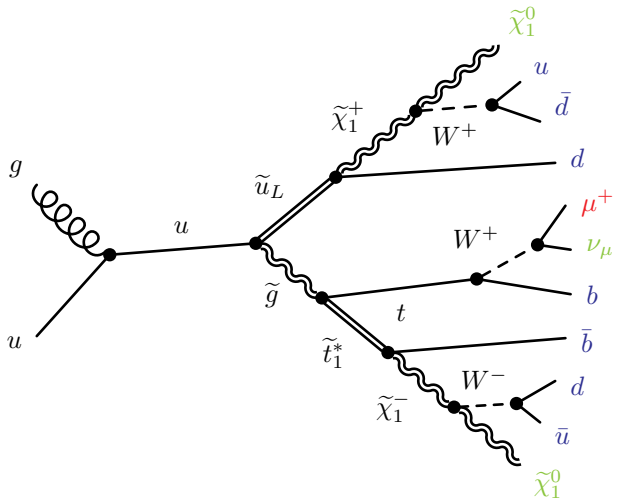

Figure 3.5: Example of a mSUGRA decay chain from the LM0 scenario corresponding to the search channel presented in this thesis with: one muon (red) at least three jets (blue) and missing transverse energy (green).

The multifold of SUSY event topologies has motivated the CMS SUSY group to divide their efforts into many individual search strategies, the so called Reference Analysis (RAs) [32]. To keep results from different searches comparable, event selection criteria of all groups are based on these topologies. The SUSY models, with cross sections varying over several orders of magnitude, are only a loose guidance when introducing kinematic cuts. This thesis follows the procedures of the single-lepton (RA4) group. They have chosen to pursue two separate and exclusive search channels: one selecting events with a single electron and the other requiring a single muon. Their final results can then be combined to give a higher significance. The single muon channel was chosen for this thesis.

Chapter 4

Experimental Setup

4.1 The Large Hadron Collider

Located at CERN[1] near Geneva, Switzerland the Large Hadron Collider (LHC) is a proton-proton collider situated in the tunnel of its predecessor, the Large Electron Positron Collider (LEP). At $\sqrt{s}$ =14 TeV design center of mass energy, it is the most energetic collider ever built. High hopes are set on probing new regimes of high-energy particle physics, testing the Standard Model and searching for signs of new physics.

Two proton beams circulate the 26.7 km long ring in opposite directions. Since both beams have the same charge, separate beam pipes must be used for their acceleration and deflection. To achieve such high energies 1232 strong superconducting dipole magnets are used, reaching fields of over 8 T. These are cooled down to temperatures below 2 K with liquid helium. Limited space in the tunnel lead to a two-in-one solution for the cooling, yet each beam has its own magnet and vacuum system. Opposed to electrons, protons loose only a negligible amount of energy via synchrotron radiation. The energy of one beam is limited to $\sqrt{s}$ =7 TeV mainly due to technical restrictions of the magnets' field strength.

Ionized hydrogen atoms deliver the protons brought to collision. Before these can be injected into the LHC ring a chain of accelerators shown in figure 4.1 is used to create collimated 450 GeV bunches of about 10^{11} particles.

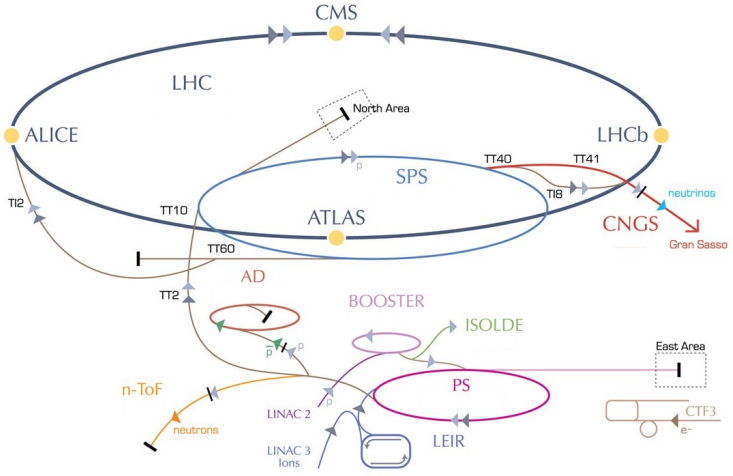

Figure 4.1: The LHC accelerator chain. Modified from [33].

A central parameter of collider physics is the instantaneous luminosity L, given per collision point via [2]:

$$L = \frac{N_p^2 \, n_{beam}}{4\pi\sigma_x\sigma_y} f \tag{4.1}$$

[1] European Organization for Nuclear Research, originally: **C**onseil **E**uropéen pour la **R**echerche **N**ucléaire

where N_p refers to the number of particles in each bunch and n_{beam} is the number of bunches per beam, reaching 2808 at design level. The width of the transverse beam profiles σ_x and σ_y are assumed to follow a Gaussian distribution. The revolution frequency f of about 11 kHz is fixed by the particles traveling through the ring nearly at the speed of light and the circumference of the ring itself. All other parameters can be optimized to ensure the highest possible instantaneous luminosity.

The luminosity can be used to relate the number of events measured per time $\dot{N}_{ev}$ to the cross section σ of a process [34]:

$$\dot{N}_{ev} = L \cdot \sigma. \tag{4.2}$$

Integrating over this equation for the time of the measurement gives the correlation between the total number of events and the so called integrated luminosity $\int L dt$. During the first round of data taking in 2010 the LHC delivered an integrated luminosity of $47\,\mathrm{pb}^{-1}$ [35].

Four main experiments are situated at interaction points along the LHC, as shown in figure 4.1. CMS[2] and ATLAS[3] are two high luminosity experiments. They are used for various new physics searches in proton and heavy-ion collisions. The CMS detector is described in more detail in section 4.2, being the source of the data investigated in this thesis. The LHCb detector specializes in new signatures in heavy flavor physics and has a forward asymmetric geometry. Focused on QCD events the ALICE[4] detector relies on heavy ion collisions produced with lead nuclei. Further information on the LHC machine and its experiments can be found in [36] [37] [38] [34] [39] [40] [41].

4.2 The Compact Muon Solenoid

The Compact Muon Solenoid (CMS) is a multipurpose detector that is used to search for signatures of new physics and remeasure quantities of the Standard Model at a design luminosity of $10^{34}\,\mathrm{cm}^{-2}\mathrm{s}^{-1}$. Used for proton, as well as heavy-ion collisions, the detector has the height of a five story building and weighs over 12 000 t. Its cylindrical shape is a compromise between the symmetrical detection of all outgoing particles and the need of space for the beam pipe. To ease construction and maintenance a five-wheel structure was chosen called the *barrel* region. Complemented by three *endcaps* on either side, the detector nearly reaches a solid angle coverage. This is an important factor for measuring the missing transverse energy of an event, discussed in section 4.4.5. Figure 4.2 shows the full detector layout. More detailed information can be found in [34].

Due to the vast range of event topologies in collision data, the CMS experiment consists of several very different detector components, each specialized on measuring specific particle types or properties. The four main detection systems will be introduced in the following sections. They are built concentrically around the collision point.

As its name suggests the CMS experiment is constructed around an extraordinary superconducting solenoid, creating a magnetic field of about 3.8 T. The tracker and calorimetry systems are located inside of the magnet, while the muon system is inserted into the sections of its iron return yoke. Thus a muon's track is bent twice in opposite directions when traversing the entire detector and its charge can be determined unambiguously.

Several different coordinate systems are used to describe the CMS detector and particle trajectories. The nominal interaction point is set as the origin. In the Cartesian coordinate system, the x-axis points to the center of the LHC ring, the y-axis points vertically upwards and the z-axis points along the beam pipe. The x-y plane is used to define the azimuthal angle ϕ, starting at the x-axis and reaching the y-axis at 90°. The polar angle θ, measured from the z-axis, has a strong dependence on the particles boost along the beam direction. One therefore resorts to using the

[2] **C**ompact **M**uon **S**olenoid
[3] **A** **T**oroidal **L**HC **A**pparatu**S**
[4] **A** **L**arge **I**on **C**ollider **E**xperiment

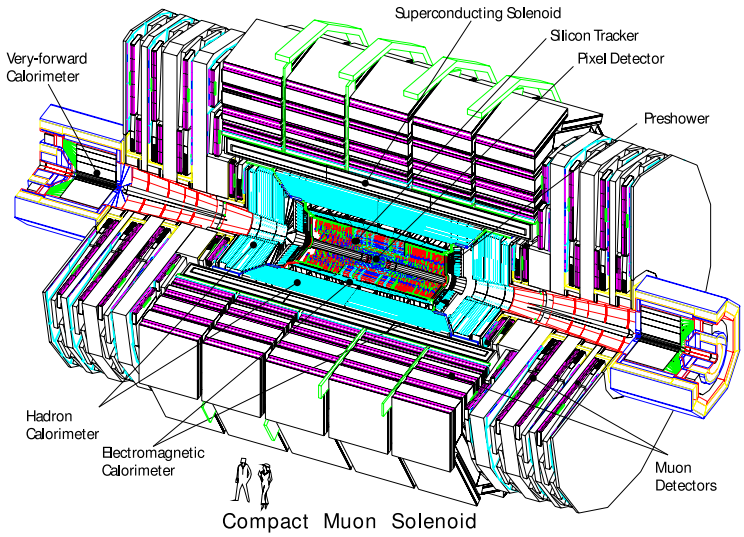

Figure 4.2: Layout of the CMS experiment highlighting its main components [34].

pseudorapidity η, defined as:

$$\eta = -\ln\left(\tan\left(\frac{\theta}{2}\right)\right). \tag{4.3}$$

It ranges from -∞ to ∞ and differences in this variable $\Delta\eta$ are Lorentz-invariant for ultra-relativistic particles with a boost in z-direction.

4.2.1 The Inner Tracking System

Reconstructed tracks of charged particles are the basis for identifying many of the objects produced in pp collisions. It is vital to provide a high spatial resolution and fast response, so each particle can be associated with the correct bunch crossing and vertices can be reconstructed. Furthermore, the detection material must withstand the high level of radiation close to the beam pipe. To fulfill all these requirements and provide a large range of coverage while still being affordable, the CMS tracker was built using two types of silicon detectors: pixel ans strip. A schematic view of the entire tracker in the r-z plane is shown in figure 4.3. In a region of $|\eta|$ <2.4 about 9 hits are provided for every track in the strip tracker and additional three hits are given in the pixel detector. With a diameter of 2.5 m the tracker's full length extends 5.8 m along the beam direction.

The innermost part of the detector consists of three cylindrical silicon pixel detector modules at radii of 4.4 to 10.2 cm, closed off by two endcap discs on either side. All together the silicon pixel detector consists of about 66 million pixels with an active area of about 1 m^2. A charged particle passing through a 100x150 μm pixel cell ionizes the silicon atoms. In the barrel region the high magnetic field is perpendicular to the charged particle's trajectory. This leads to a Lorentz drift of the electric charge over several cells, resulting in a spatial resolution in the order of 10 μm. In the endcaps this behavior is enhanced by tilting the forward detector elements. All three spatial coordinates can be measured simultaneously.

To extend the tracker's reach, while keeping the number of read-out channels at an affordable and manageable level, silicon micro-strip modules are used. Four inner barrel layers (TIB) and three discs (TID) at each end deliver up to four hits in the r-ϕ plane. The respective strips are aligned parallel and radial to the beam axis. A strip pitch of 80 and 120 μm enables a single hit resolution of 23 and 35 μm in the TIB. The strip pitch of the TID varies from 100 μm to 141 μm. The outermost parts of the tracker consist of six barrel layers (TOB) and nine endcap disks (TEC). Due to the lower particle flux in the outer region a wider strip pitch can be chosen, again reducing

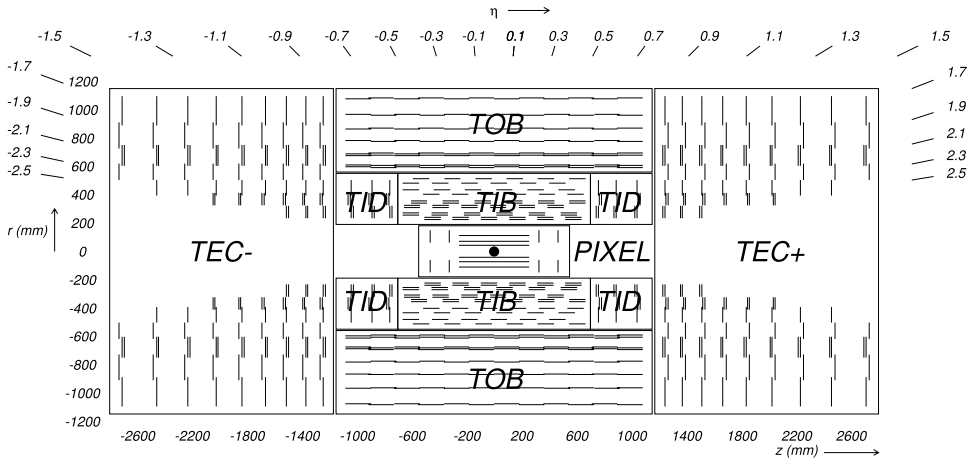

Figure 4.3: Layout of the CMS tracker in the r-z plane. Stereo modules are represented by a double line [34].

the number of read-out channels. To gain access to the a second orthogonal coordinate in the barrel and endcap, several modules have a further micro-strip detector mounted on the back at a specific stereo angle. These are marked with double lines in figure 4.3.

To reduce radiation damage the entire tracker has to be cooled down to below -10 °C. Combining the pixel and strip detector leads to a resolution in transverse momentum of [42]

$$\frac{\delta p_T}{p_T} = \sqrt{\left(c\left(\eta\right) \cdot \frac{p_T}{\mathrm{TeV}}\right)^2 + (0.5\%)^2}, \tag{4.4}$$

where the value of $c\left(\eta\right)$ rises from 15% to 60% with increasing η.

4.2.2 The Electromagnetic Calorimeter

The electromagnetic calorimeter (ECal) is used to determine the energy of particles after they have passed through the tracker. This is achieved by over 68000 lead tungstate crystals mounted in the barrel and endcap regions as shown in figure 4.4. This material was chosen for its high density and short radiation length. The size of the crystals is determined so that electrons and photons deposit most of their energy within the region of a single crystal. During a particle's passage through the scintillator, photons are emitted and a fast read-out must be ensured. This is solved with avalanche photo diodes in the barrel and vacuum photo triodes in the endcaps. These are rather insensitive to the high magnetic field throughout the ECal. Overall a coverage of about $|\eta| < 3.0$ is reached.

High energy photons in the endcaps can be faked by the decay of a π_0 meson. Within this range of pseudorapidity a high energy π_0 of typically about 60 GeV will result in two angularly close photons, which would be reconstructed as one high energy photon in the crystal ECal. To reduce this effect a preshower system is installed in both endcaps. It is made of alternating lead and silicon strip layers. The silicon sensors measure the electromagnetic showers initiated by the photons in the lead radiators with a high granularity capable of identifying the individual photons.

The energy resolution of a 3x3 crystal array was measured using electron beams with energies up to 250 GeV and found to be [34]:

$$\frac{\delta E}{E} = \sqrt{\left(\frac{2.8\%}{\sqrt{E/\mathrm{GeV}}}\right)^2 + \left(\frac{0.12}{E/\mathrm{GeV}}\right)^2 + (0.30\%)^2}. \tag{4.5}$$

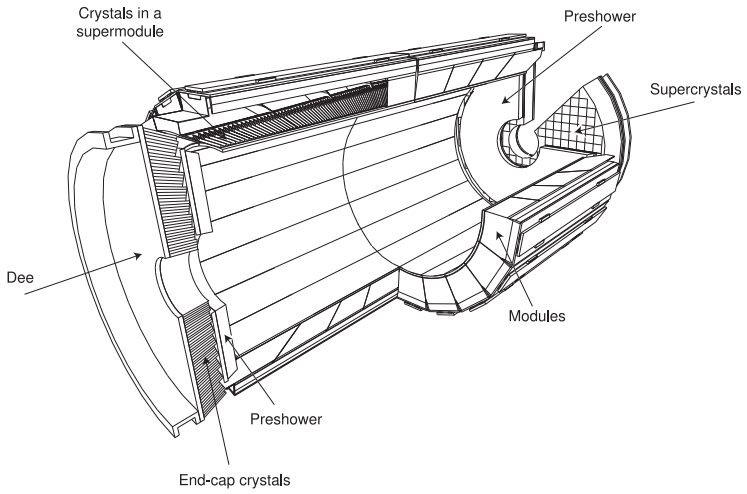

Figure 4.4: Drawing of the ECal system showing the barrel end endcap crystals as well as the preshower detector [34].

The first term incorporates statistical fluctuations inside the crystals and of the light yield. Noise from the electronics and digitalization as well as pile-up effects are summarized in the second term. An additional constant is used to correct the calibration and accounts for energy leakage at the back of the crystal occurring primarily at energies exceeding about 500 GeV.

4.2.3 The Hadron Calorimeter

Hadron jets produced in the collisions loose only a part of their energy in the ECal. To measure the entire hadronic shower a thick calorimeter is needed. Since the space left between ECal and the solenoid does not suffice, an additional layer is placed outside of the magnet, the hadron outer (HO). The entire system consist of four different parts as shown in figure 4.5.

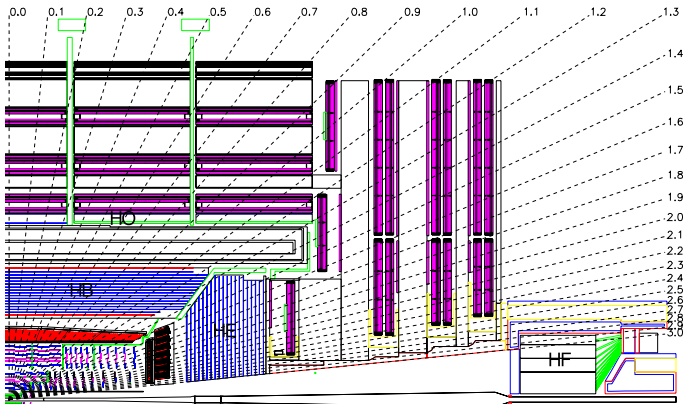

Figure 4.5: View of the CMS detector in the r-z plane highlighting the placement of the hadron calorimeter subsystems [34].

Similar to the ECal layout a hadron barrel (HB) and endcap (HE) are installed within the solenoid. They consist of approximately 70 000 tiles of alternating brass absorbers and plastic scintillator layers, thus detecting the entire shower length. For extra mechanical support the inner and outermost absorber layers are made of steel. To be in accordance with the electromagnetic calorimeter and the muon chambers, a granularity in $\Delta\eta$-$\Delta\phi$ of 0.087 was chosen in a range of $|\eta|$ <1.6 and

0.17 for larger pseudorapidity ranges. The combination of ECal barrel crystals and the HCal barrel structure including the hadron outer ensures an absorber thickness of nearly 12 hadronic interaction lengths.

To seal the HCal almost hermetically the hadron forward (HF) calorimeters are placed around the beam pipe at either end of the endcaps. They expand the range in pseudorapidity from η=3 to η=5.3, thus enabling a good measurement of the missing transverse energy in an event. The most important requirement to be fulfilled by the hadron forward is a high radiation hardness. Quartz fibers with a diameter in the order of 100 μm were chosen. They transmit Cherenkov light created by the traversing particles and hence are most sensitive to the electromagnetic component of the showers.

At energies from 30 GeV to 1 TeV, the combined resolution of ECal and HCal can be approximated to [43]:

$$\frac{\delta E}{E} = \sqrt{\left(\frac{100\%}{\sqrt{E/\mathrm{GeV}}}\right)^2 + (4.5\%)^2}, \tag{4.6}$$

for jets, if dependencies on η, ϕ and $\not{E}_{\mathrm{T}}$ are neglected.

4.2.4 The Muon System

Muons are signatures of various new physics processes and their identification and momentum measurement is a central task of the CMS detector. Furthermore muons are often used to trigger the events over a large kinematic range, which will be explained in section 4.3. To enable a good resolution over a large spatial and energetic range three types of gaseous detectors are used: drift tube chambers (DT), cathode strip chambers (CSC) and resistive plate chambers (RPC). A longitudinal quadrant of the CMS detector with special focus on the muon system can be seen in figure 4.6. Four muon stations are inserted into the return yoke of the solenoid. The iron offers additional shielding against high energy hadrons, thus almost exclusively muons are detected in the chambers.

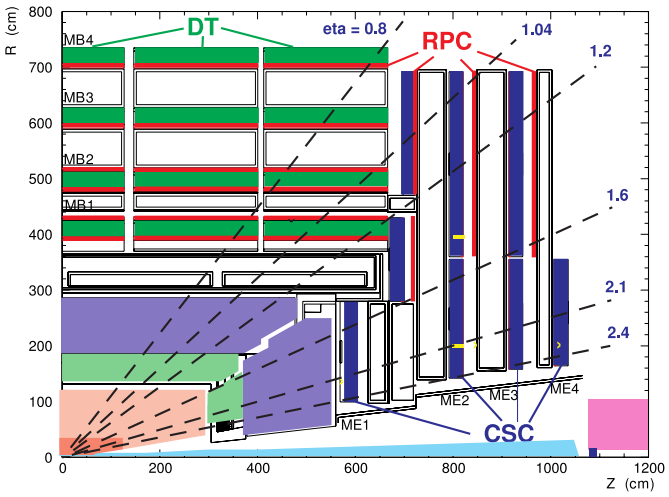

Figure 4.6: Longitudinal view of the CMS detector with focus on the muon system [44].

A total of 250 drift tube chambers (DTs) are used in the barrel region of $|\eta|$ <1.2, where the muon flux and magnetic field are relatively low. Filled with a mixture of argon and carbon dioxide, the individual DT cells are grouped together in a staggered fashion to form a superlayer. This helps increase the sensitive detector volume and gives an improved spatial resolution. Two or three

superlayers are then combined to form a DT chamber. Each DT cell contains one 50 μm thick anode wire, two aluminum cathode strips and two field-shaping strips. A maximum drift time of 380 ns is reached by adjusting the proportion of the two gas types. Assuming the LHC nominal bunch spacing of 25 ns, about 15 bunch crossings occur during this time.

To survive the higher radiation levels and inhomogeneous magnetic field in the endcaps, 468 cathode strip chambers (CSC) are installed, identifying muons within $0.9 < \eta < 2.4$. Arranged perpendicular to the beam, trapezoidal discs of six anode wire planes layered between seven cathode panels are overlapped. This ensures a full coverage of ϕ, without gaps. Cathode strips and anode wires build an angle of 90 °, so a measurement of r and ϕ is possible within a few millimeters. By combining measurements from all six planes of a chamber, the time resolution is narrow enough to assign each hit to the correct bunch crossing.

Since muons are often used to trigger events, an even better time resolution is needed once the LHC reaches its full luminosity. Additional resistive plate chambers (RPCs) are installed in both barrel and endcap, marked in red in figure 4.6. They ensure a reliable trigger performance over $|\eta|$ <1.6. RPCs consist of two parallel bakelite plates, performing as ground electrodes, and separated by about 2 mm with a gas mixture [45]. They are coated with conductive graphite paint on the outside to form high voltage electrodes. A pair of two gaps operated in avalanche mode, share a set of read-out strips, thus increasing the signal strength.

In total about 25 000 m^2 and a full eta range of $|\eta| < 2.4$ are covered by the muon system. Figure 4.7 shows the resolution of a muon as a function of its transverse momentum p_T and pseudorapidity. The resolution of the inner tracking system and muon spectrometer are depicted separately as well as combined.

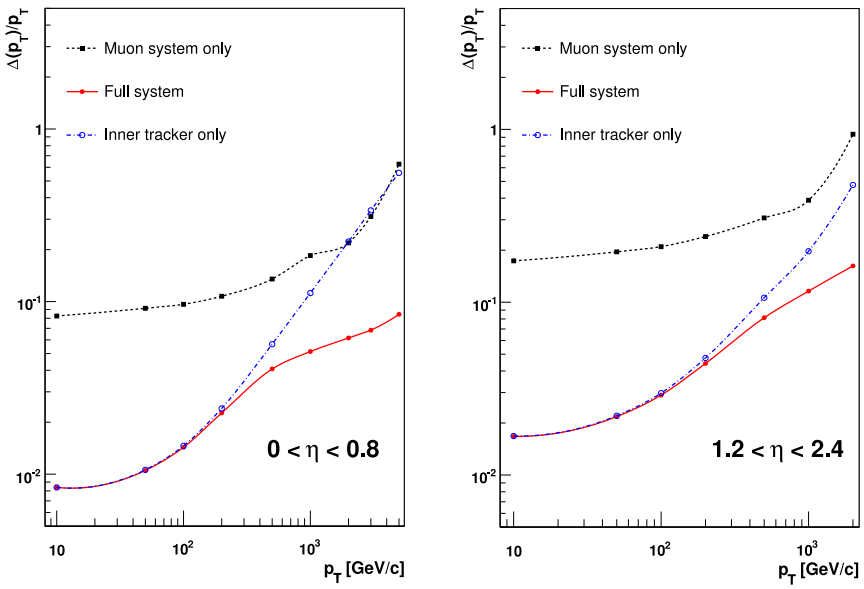

Figure 4.7: Resolution of a muon's transverse momentum for two different ranges in η. Separate functions are shown for the muon system and inner tracker, as well as their combination [34].

4.3 Triggers

Running the LHC at design luminosity produces about 10^9 collisions per second [46]. This immense amount of data must be reduced by at least seven orders of magnitude to allow processing and storage, in any case most of the events taking place are not of interest to analyses. At CMS a

two-level trigger system is installed, selecting the more interesting events in which possibly new particles are produced.

The first step consists of a custom hardware-based, so called *Level-1* (L1) trigger. It is in direct succession of the front-end electronics which provide the read-out of the detector elements. It processes the coarse input from the muon system and calorimeters, whilst storing the complete high-resolution information of the tracker during the latency time of 3.2 μs. The decision to accept or discard a specific event is based on an energy threshold of the detected objects. It is important to achieve a high trigger efficiency (>95%) in the sensitive range of $|\eta| < 2.5$.

An event passing the L1 trigger reaches the High-Level Trigger filters (HLT), which are software-based using about one thousand commercial processors [34]. Taking the entire event into account procedures are performed that are comparable to those of the off-line physics object reconstruction. Trigger paths are defined that set requirements on event topologies such as the multiplicity and energy of specific particles, i.e. muons, or also on such quantities as the sum of the transverse jet energies H_T.

The precise trigger strategy used for the presented analysis will be discussed in section 5.3.

4.4 Reconstruction of Physics Objects

Dedicated methods have been developed to deduce the actual physics objects used in analyses from the data taken at the CMS detector. The following section will introduce techniques used for the reconstruction of the objects taken into account for this thesis: muons, electrons, jets and missing transverse energy $\not{E}_{\mathrm{T}}$.

4.4.1 Muons

Aside from rare *punch-through* particles, muons are the only visible objects to traverse the entire detector. They are minimum ionizing particles whose energy loss is more or less independent of the initial energy. As with every charged particle inside the CMS detector, a muon's trajectory is curved due to the magnetic field. This curvature can be used to determine the particle's charge and momentum.

A charged particle causes so called *hits* in the tracker by ionizing material of the detector components. A pair of hits, one at a larger radius than the other, that are compatible with a given beam spot are chosen as the *seed* [47] for a combinatorial Kalman filtering technique [48]. This method executes a least-squares approach of the measurements to a track model, working from the innermost hit outwards. It is followed by a smoothing procedure working in the opposite direction. Once the track is defined the particle's initial direction can be determined by its tangent at the vertex.

This track building technique can also be used independently in all three detector types of the muon system. When extending the trajectory progressively from one chamber to the next energy loss due to material effects such as bremsstrahlung in the iron return yoke is also taken into account.

Three categories of muons are reconstructed at CMS from tracker and/or muon system information: *tracker*, *standalone* and *global* muons [49]. Tracker muons are based on reconstructed tracks in the tracker with p_T >0.5 GeV and p >2.5 GeV. If extrapolating the track to the muon system returns at least one segment, the muon is considered valid. If a muon can only be identified in the muon spectrometer it is considered standalone. Due to a high tracking efficiency in the inner detector only approximately 1% of muons originating from the hard scattering process are only detected in the muon system, without leaving hits in the tracker. Lastly, a global muon is built by matching a standalone muon to a tracker track. A fit is then performed to redefine the complete

track, improving the momentum resolution of the muon.

4.4.2 Electrons

Electron reconstruction initiates with clustering energy deposits in the ECal [50]. Due to the high magnetic field, electrons exhibit a curved track. Thus bremsstrahlung photons, which are emitted during the passage of tracker layers, spread out over a wider range in ϕ. Though a single electron or photon leaves about 97% of its energy within a 5x5 array of ECal crystals, a so called *cluster*, one must extend the region in ϕ to account for the energy of the bremsstrahlung photons. A single ECal crystal with a high energy deposit seeds the cluster, which is in turn used to seed a *supercluster*. Two different clustering algorithms are used to determine the supercluster in the barrel and endcaps, both optimized to include radiated photons into the energy sum.

The electrons' tracks are determined by similar methods described above for muons. However they do not rely on a Kalman but on a Gaussian Sum Filter (GSF) [51]. The Kalman filter performs best with single Gaussian probabilities, yet this does not describe the behavior of an electron with photon radiation. The GSF extends from one to several Gaussian distributions to describe the energy loss of an electron in the tracker layers. Seeding of the GSF is done by reconstructing the initial electron energy from the supercluster and extrapolating it to the impact point in question.

4.4.3 The Particle Flow Algorithm

The jet and $\not{E}_{\mathrm{T}}$ reconstruction described in the following sections rely on the particle-flow algorithm. Future analyses could profit from using particle-flow also for electrons and muons [52]. This thesis reconstructs them via the methods described above.

The particle-flow algorithm [53] is used to distinguish five types of stable particles subsequently used to reconstruct all desired physics objects: charged and neutral hadrons, muons, electrons and photons. The fundamental idea behind the algorithm is to include all CMS detector components for their reconstruction, then using these stable particles to assemble the desired physics objects e.g., jets, $\not{E}_{\mathrm{T}}$ and taus.

The tracker is essential for delivering precise measurements of the transverse momentum and direction of charged particles, thus it is of great value to ensure a high tracking efficiency, whilst keeping the fake rate at a low level. This is achieved by an iterative strategy: first a negligible fake rate is realized by using very tight seeding criteria for tracks. Hits identified as part of a good track in each iteration are removed to keep the fake rate down in further iterations. These following iterations are performed with increasingly loose quality requirements on the tracks.

To reach a high detection rate for neutral and charged particles of all energies in the calorimeters a specialized algorithm has been developed for particle-flow. Its persuasive feature is the separation of energy deposits close to one another but originating from different particles. The algorithm is seeded by deposits exceeding a given energy threshold. They are then grouped with neighboring cells fulfilling a minimal energy requirement. These *topological clusters* are then seeds for larger *particle-flow clusters*.

To build stable particles from the individual detector components a link algorithm is performed, also removing objects counted twice. First charged particle tracks are matched to the particle-flow cluster by extrapolating the electromagnetic and hadronic shower profiles of the particle in question to the calorimeters. Bremsstrahlung photons are considered by fitting tangents to the electron tracks and extending them to the ECal.

If tracker tracks are compatible with ones in the muon system, a muon is reconstructed by the same procedure as the global muon described above and denoted as a *PF muon*. Next tracks to a single ECal cluster are refit with a Gaussian Sum Filter to define *PF electrons*. Remaining tracks are tagged as *PF charged hadrons* if their momentum agrees with the energy sum in ECal and

HCal. Calorimetry deposits that cannot be linked to tracks give rise to a *PF photon* or *neutral hadron*.

4.4.4 Jets

The reconstruction of jets strives to deduce the initial quark's or gluon's fragmentation and hadronization processes. There are four different approaches at CMS to define jets, each using different combinations of the detector components: calorimeter-based *CALO jets*, track based *TrackJets*, jets following the Jet-Plus-Track algorithm (*JPT jets*) and ones following the particle-flow algorithm (*PF jets*). The jets used in this analysis are particle-flow jets that have been clustered with the anti-k$_T$ algorithm [54] with a size parameter of R=0.5.

The anti-k$_T$ sequential jet clustering algorithm combines the advantages of a cone and a sequential recombination algorithm, returning approximately cone-shaped infrared safe[5] and collinear safe[6] jets. Cone shaped jets are beneficial, since corrections to the jets are applied with respect to a mean jet position. Defining the distance d_{ij} between particles i and pseudojets j, as well as the distance between particles and the beam d_{iB} one selects the smallest of these distances during each phase of the iteration. If a distance d_{ij} is smallest one combines the respective particle and pseudojet to a larger pseudojet. If a d_{iB} is smallest one declares the respective particle a jet. This procedure is common to all sequential clustering algorithms [55] [56]. Due to a particular choice of defining these distances the anti-k$_T$ algorithm succeeds in producing the qualities mentioned above.

4.4.5 Missing Transverse Energy

Despite its large range of coverage, not all detectable particles are seen by CMS: particles passing through the cracks of the sensitive detector elements or ones flying in forward direction traveling along the beam pipe. To reduce the influence of particles of the latter kind the momentum imbalance of an event is calculated in the plane perpendicular to the beam axis [57]. The large and continuous coverage of the detector facilitates the measurement of the entire missing energy of an event. Particles in forward direction only have a small transverse component, thus the uncovered region of the beam pipe does not present a significant loss in $\not\!\!E_{\mathrm{T}}$. Events from Standard Model processes can only exhibit real missing transverse energy $\not\!\!E_{\mathrm{T}}$ through neutrinos. A large amount of $\not\!\!E_{\mathrm{T}}$ is a valuable indicator for new physics describing heavier uncharged, weakly interacting particles, such as neutralinos.

Three $\not\!\!E_{\mathrm{T}}$ flavors have been developed within the CMS collaboration: *particle-flow* (PF) $\not\!\!E_{\mathrm{T}}$ [53], calorimeter-based *CALO* $\not\!\!E_{\mathrm{T}}$ [58] and *Track Corrected* (TC) $\not\!\!E_{\mathrm{T}}$ which includes particles detected in the tracker to the energy deposits in the calorimeters [59]. The PF $\not\!\!E_{\mathrm{T}}$ used in this thesis can be easily calculated as the negative sum of the transverse momentum vectors from all reconstructed particle flow candidates.

Furthermore $\not\!\!E_{\mathrm{T}}$ is divided into two categories: the *clustered* and *unclustered* energy. The former consists of contributions from isolated high p_T electrons and photons, as well as muons and jets. The unclustered energy sums up any energy left in the detector that has not been assigned to one of these four physics object [60].

4.4.6 Jet Energy Scale and $\not\!\!E_{\mathrm{T}}$ Corrections

If one compares the true energy of a jet, i.e. from the generator information of a Monte Carlo simulation (see section 5.2 for details), one finds a discrepancy to the energy reconstructed from the measurement in the detector. A non-linear response of the calorimeters is the main reason for

[5] insensitive to soft gluon radiation
[6] insensitive to splitting one jet into two parallel ones

this. The deviations are functions of η as well as p_T, changing the shape and rate of kinematic distributions. Corrections must be applied to the detector jet's PF constituents to ensure a flat dependency in both variables.

Calibration of the jets is performed with Monte Carlo simulations [61]. An angular matching is performed between generator and reconstructed jets. Their ratio determines a multiplicative factor, which factorizes to an η and a p_T dependent component. The so called L2 relative correction [62] uses this factor to correct the detector jet in η. Data events with back-to-back dijets are used for crosschecks. The L3 absolute correction is applied afterward and ensures the detector jet response is flat in p_T. A crosscheck can be made with γ+jet events, since photons can be measured very accurately in the ECal. Both data-driven calibration methods will be used as a replacement once statistics are high enough. Moreover small discrepancies between the jet energy response in data and MC were found. These are corrected by applying the *residual* jet corrections (L2+L3) to the data, thus compensating detector effects. All three corrections applied are accompanied by a systematic uncertainty explained in section 5.6.

Additional corrections to the jet's energy can be made to remove the impact of pile-up, a dependence on the fraction of energy in the ECal or on the quark flavor, but they are not used by default within the CMS collaboration.

Since the missing transverse energy is reconstructed from the jet constituents the L2 and L3 corrections applied to the particle-flow candidates are also propagated into the clustered energy, the so called type-I $\not\!\!E_{\mathrm{T}}$ correction. PF $\not\!\!E_{\mathrm{T}}$ is less sensitive to these adjustments than CALO $\not\!\!E_{\mathrm{T}}$. Additional corrections to the unclustered energy, known as type-II, have been optimized with $Z \to ee$ events, but are generally not used within CMS groups [60]. Results from studies show that influence of both type-I and type-II corrections is rather small [63][60]. Neither corrections are used in this thesis, yet an uncertainty has been assigned as discussed in section 5.6.

Chapter 5

Analysis

The analysis to be presented searches for experimental signatures of a supersymmetric extension of the Standard Model. The search channel is defined by events containing exactly one muon, at least three jets and missing transverse energy. Section 5.1 will address Standard Model background processes mimicking the search topology. Monte Carlo estimates used to conduct a comparison of CMS experimental data to the simulated processes will be introduced in section 5.2.

To differentiate between potential signatures of supersymmetry and background (BG) events, kinematic and topological cuts are applied to data and simulation. Methods used within the CMS collaboration to identify the quality of reconstructed physics objects will be introduced in section 5.3, followed by analysis based cuts in section 5.4. At an early stage of the event selection QCD multi-jet is the main Standard Model process. A data-driven technique used to validate the Monte Carlo estimate of this background is explained in section 5.5.

The evaluation of systematic uncertainties in the analysis is discussed in section 5.6. Due to a lack of evidence for supersymmetry in the 2010 data, exclusion limits are set in three regions of the mSUGRA parameter space in section 5.7.

5.1 Standard Model Backgrounds

A strong signature of R-Parity conserving supersymmetry is a large amount of missing transverse energy originating from the undetectable pair of LSPs. An isolated lepton can be produced via the electroweak decay of a slepton, chargino or neutralino and can be used to reduce a great amount of the Standard Model background events. Quark and gluon jets are added to the event signature during the complex decay cascade. A possible search channel that results from this contains one muon, at least three jets and $\not{E}_{\mathrm{T}}$.

Unfortunately several Standard Model processes exhibit a similar event topology. Figure 5.1 gives examples of Feynman diagrams for some of the processes considered in this analysis. Efficient ways must be found to reduce these backgrounds without loosing too much of the signal.

The total cross section of the proton-proton process is approximately 100 mb [64]. About one fourth of this value can be assigned to an elastic scattering of the two particles. The remaining 75% make up the inelastic cross section, representing collisions in which at least one of the protons is destroyed.

With a large cross section of about 37 mb, see table 5.2 for details, the purely quantum chromodynamical production of quarks and gluons is a very prominent background. It is often referred to as QCD or QCD multi-jet. Figure 5.1(a) shows an example of a Feynman diagram that contributes to this process. Fortunately this background can be suppressed by requiring an isolated lepton. The reconstructed leptons in QCD multi-jet events are either produced inside of a jet, or the jet itself is misidentified as a lepton. Missing transverse energy can be produced by neutrinos or "faked" by detector mis-measurements.

The next most frequently produced background at center of mass energies of about $\sqrt{s} = 7\,\mathrm{TeV}$ is the W boson. It decays equally to lepton-neutrino pairs from all three generations, as shown in figure 5.1(b), but with a branching ratio of about 68%, the dominant decay is into jets. For the leptonic decay additional jets needed to fulfill the signature requirements can be produced by

initial-/final state radiation or by pile-up effects.

The $t\bar{t}$ background has a very similar topology to the signal processes, an example is given in figure 5.1(c). Due to its short lifetime in the order of 10^{-24}[s] [65] the top decays before top flavored hadrons can develop. Two b quarks and W bosons are produced. If one of the W bosons decays leptonically and the other one via a quark and anti-quark pair the topology of the event is identical to the one searched for. A reduction of $t\bar{t}$ is challenging, and it is the main background in the final event selection.

Drell-Yan is a charged and neutral current process in which an off-shell photon or Z boson is produced and decays into neutrino or charged lepton pairs, as shown in figure 5.1(d). This means that either the isolated lepton or the missing transverse energy must be fakes in someway or another to fulfill the search criteria.

Diboson events with WW, WZ or ZZ production can also mimic the SUSY signal. Yet they are not as abundant as the processes mentioned above. Figure 5.1(e) gives an example of WW production and decay.

The single-top s, t and tW channels add up to a cross section of about 30 pb and play a minor role in the composition of SM backgrounds. A s-channel production is given in figure 5.1(f).

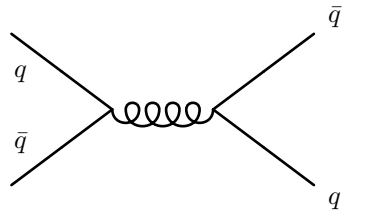

(a) Example of QCD Multi-jet BG

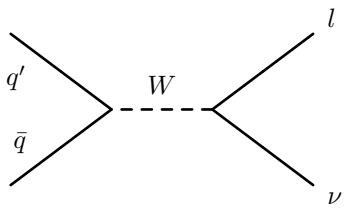

(b) Example of W to $l\nu$ BG

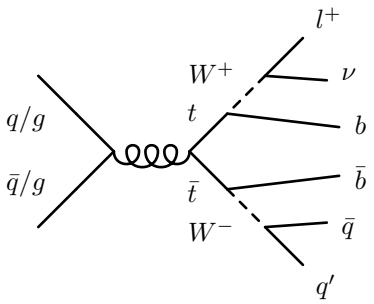

(c) Example of $t\bar{t}$ BG

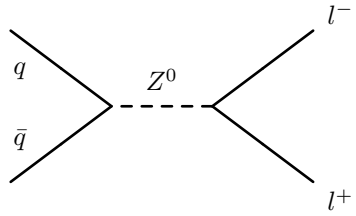

(d) Example of Drell-Yan BG

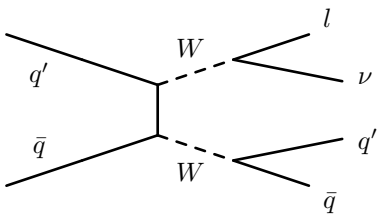

(e) Example of diboson BG

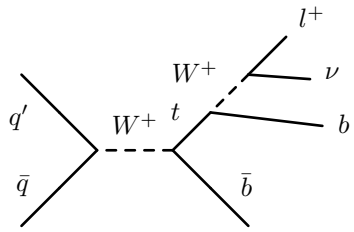

(f) Example of single-top s-channel BG

Figure 5.1: Feynman diagrams for several Standard Model background processes.

5.2 Monte Carlo Simulation and Data Samples

To provide an estimate of the Standard Model and signal processes, so called Monte Carlo (MC) samples are used. Examples of several physics processes have been given in figures 3.5 and 5.1. An event generator, such as PYTHIA 6 [30], follows several steps, which will be outlined in the following paragraph, to produce a model of such a process.

Parton distribution functions, discussed in more detail in section 5.6.1, define the partonic substructure of the colliding protons. The hard scattering i.e., the process between the two incoming partons and the two outgoing particles, is evaluated from the quantum mechanical matrix element. Both in the initial and in the final state gluons and photons may be radiated, which is taken into account by the so called parton showering. In cases such as $t\bar{t}$, diboson or SUSY processes the final state particles decay further, often referred to as resonance decays. Due to color confinement all quarks and gluons undergo a fragmentation process resulting in stable colorless hadrons. The particle's passage through the CMS detector material is then simulated with GEANT 4 [66].

Thus, a Monte Carlo sample consists of many events mimicking the quantum mechanical fluctuations of the data by means of statistical fluctuations following the desired probability distributions. In contrast to the data, one can access the originally generated physics process in the Monte Carlo simulation. In data only the reconstructed detector objects can be observed.

Samples used in this thesis were generated at tree-level using either the PYTHIA 6 [30] or MadGraph [67] event generator. In most cases PYTHIA 6 is also used for the showering. Decays of tau leptons were simulated with TAUOLA [68].

The so called underlying event summarizes the parts of the event that do not belong to the hard scattering process e.g., beam-beam remnants and multiple-parton interactions (MPI). Studies at the Tevatron [69] and at the LHC [70] have performed data–Monte Carlo comparisons resulting in different so called *tunes* of the event generator. The tunes consist of a set of parameters that are adjusted to control the modeling of the MPI, initial-state radiation and intrinsic transverse momentum of the partons, achieving a better description of the data. The Monte Carlo samples used in this analysis were generated using tune Z2 which is similar to the Z1 tune [71], apart from a different model for the parton density functions.

Tables 5.1 and 5.2 list the process names, number of events and cross sections of all Monte Carlo samples used throughout the analysis. Cross sections given at leading order (LO) were calculated during the MC generation [72], while higher order cross sections were obtained from [73]. The uncertainties given will be propagated into the number of events in the final selection as discussed in section 5.6.

To develop a basic cut strategy, SUSY benchmark points LM0 and LM1 are used at leading order. This is a more conservative approach than using the next-to-leading order (NLO) cross sections of 54.9 pb for LM0 and 6.6 pb for LM1 [74]. A short signal study for these two benchmarks was given in section 3.5, highlighting their main characteristics. The final step of the analysis is performed at NLO for a range of scenarios in the m_0-$m_{1/2}$ plane. A_0, $\tan\beta$ and $sign(\mu)$ are set to constant values in each scenario.

The data used for this analysis corresponds to an integrated luminosity of about $\int Ldt$=36 pb^{-1} and was taken throughout 2010 at a center of mass energy of $\sqrt{s}$ =7 TeV. To scale all Monte Carlo estimates to this luminosity the following factor is applied to all MC samples:

$$scale = \frac{\int Ldt}{\int L_{MC} dt} = \frac{\int Ldt \cdot \sigma}{N}, \tag{5.1}$$

where $\int L_{MC} dt$ is the integrated Monte Carlo luminosity defined as the ratio of the number of generated events N and the respective cross section σ. In all of the plots shown throughout this thesis the Monte Carlo estimates are normalized in this fashion if not stated otherwise.

Process	Sample	$\sigma \pm \Delta\sigma_{sys}$ / pb
$t\bar{t}$	TTJets_TuneZ2_7TeV-madgraph-tauola*	165 ± 10 (NNLL)
single top s-ch.	TToBLNu_TuneZ2_s-channel_7TeV-madgraph*	1.5 ± 0.2 (NNLL)
single top t-ch.	TToBLNu_TuneZ2_t-channel_7TeV-madgraph*	$21.5^{+0.5}_{-0.37}$ (NLO)
single top tW-ch.	TToBLNu_TuneZ2_tW-channel_7TeV-madgraph*	10.6 ± 0.8 (NLO)
$W \to \mu\nu$	WToMuNu_TuneZ2_7TeV-pythia6*	10438 ± 136 (NNLO)
$W \to \tau\nu$	WToTauNu_TuneZ2_7TeV-pythia6-tauola*	10438 ± 136 (NNLO)
WW	WWtoAnything_TuneZ2_7TeV-pythia6-tauola*	43 ± 1.5 (NLO)
WZ	WZtoAnything_TuneZ2_7TeV-pythia6-tauola*	18.2 ± 0.7 (NLO)
ZZ	ZZtoAnything_TuneZ2_7TeV-pythia6-tauola*	5.9 ± 0.15 (NLO)
$\gamma^*/Z \to \mu\mu$	DYToMuMu_M-10To20_TuneZ2_7TeV-pythia6*	3407 ± 23 (LO)
$\gamma^*/Z \to \mu\mu$	DYToMuMu_M-20_TuneZ2_7TeV-pythia6*	1666 ± 11 (NNLO)
$\gamma^*/Z \to \tau\tau$	DYToTauTau_M-10To20_TuneZ2_7TeV-pythia6-tauola*	3407 ± 185 (LO)
$\gamma^*/Z \to \tau\tau$	DYToTauTau_M-20_TuneZ2_7TeV-pythia6-tauola*	1666 ± 91 (NNLO)
LM0	LM0_SUSY_sftsht_7TeV-pythia6*	38.93 (LO)
LM1	LM1_SUSY_sftsht_7TeV-pythia6*	4.888 (LO)

Table 5.1: Specifications of the electro-weak and LM point Monte Carlo samples used in the analysis, where * = /Winter10-E7TeV_ProbDist_2010Data_BX156_START39_V8-v1/AODSIM. The number of generated events is in the range of $2 \cdot 10^5 - 5 \cdot 10^6$. The systematic uncertainties $\Delta\sigma_{sys}$ on the cross sections will be discussed in section 5.6.6. Both Drell-Yan backgrounds are divided into two samples with 10 GeV< m_{ll} <20 GeV in the first and m_{ll} >20 GeV in the second.

$\hat{p}_T$ / GeV	Sample	# Events	σ / pb (LO)
$20 - \infty$	QCD_Pt-20_MuEnrichedPt-15_TuneZ2_7TeV-pythia6*	5000000	84679
$5 - 15$	QCD_Pt_5to15_TuneZ2_7TeV_pythia6*	1648096	36750000000
$15 - 30$	QCD_Pt_15to30_TuneZ2_7TeV_pythia6*	5420080	815900000
$30 - 50$	QCD_Pt_30to50_TuneZ2_7TeV_pythia6*	3244045	53120000
$50 - 80$	QCD_Pt_50to80_TuneZ2_7TeV_pythia6*	164994	6359000
$80 - 120$	QCD_Pt_80to120_TuneZ2_7TeV_pythia6*	3208299	784300
$120 - 170$	QCD_Pt_120to170_TuneZ2_7TeV_pythia6*	3045200	115100
$170 - 300$	QCD_Pt_170to300_TuneZ2_7TeV_pythia6*	3212880	24260
$300 - 470$	QCD_Pt_300to470_TuneZ2_7TeV_pythia6*	3160200	1168
$470 - 600$	QCD_Pt_470to600_TuneZ2_7TeV_pythia6*	2009369	70.22
$600 - 800$	QCD_Pt_600to800_TuneZ2_7TeV_pythia6*	1968447	15.55
$800 - 1000$	QCD_Pt_800to1000_TuneZ2_7TeV_pythia6*	2070884	1.844
$1000 - 1400$	QCD_Pt_1000to1400_TuneZ2_7TeV_pythia6*	1077390	0.3321
$1400 - 1800$	QCD_Pt_1400to1800_TuneZ2_7TeV_pythia6*	1021510	0.01087
$1800 - \infty$	QCD_Pt_1800_TuneZ2_7TeV_pythia6*	529360	0.0003575

Table 5.2: Specifications of the different QCD Monte Carlo samples used in the analysis, where * = /Winter10-E7TeV_ProbDist_2010Data_BX156_START39_V8-v1/AODSIM. A scale of 1.3 is applied to the QCD_Pt_1400to1800 sample to ensure a continuous $\hat{p}_T$ distribution.

At an early stage of the analysis, the main background of the channel examined here is QCD multi-jet. Consequently it is important to have a good amount of statistics in the Monte Carlo estimate for this process. This is also a crucial factor for performing cross checks of the data-driven QCD background estimate discussed in section 5.5. In order to obtain a good description of this background in Monte Carlo, a short study is done with two different types of samples.

Figure 5.2 shows the $\hat{p}_T$ distribution for the muon enriched and the $\hat{p}_T$-binned QCD MC samples, see table 5.2 for details on these samples. The generator level variable $\hat{p}_T$ is the transverse momentum of the hard interaction and is an input parameter during the production of the MC sample. The $\hat{p}_T$ distribution is steeply falling, so a great deal of the generated events will gather at low $\hat{p}_T$. To achieve a good amount of statistics, even at high values of $\hat{p}_T$, one can divide the sample into several subranges of $\hat{p}_T$ and generate events separately for each interval. This has been performed for the binned sample shown in blue and green lines in figure 5.2. The muon enriched sample, shown in red in figure 5.2, is generated by requiring the produced hadrons to decay into to a muon within a given cylindrical volume around the primary vertex.

Comparing the statistics of both samples, drawn as shaded areas in figure 5.2, shows that it is best to use the muon enriched sample up to $\hat{p}_T$=120 GeV and the binned QCD sample for the remaining spectrum. This combination will be used throughout the following chapters and will be denoted as "QCD" in all legends.

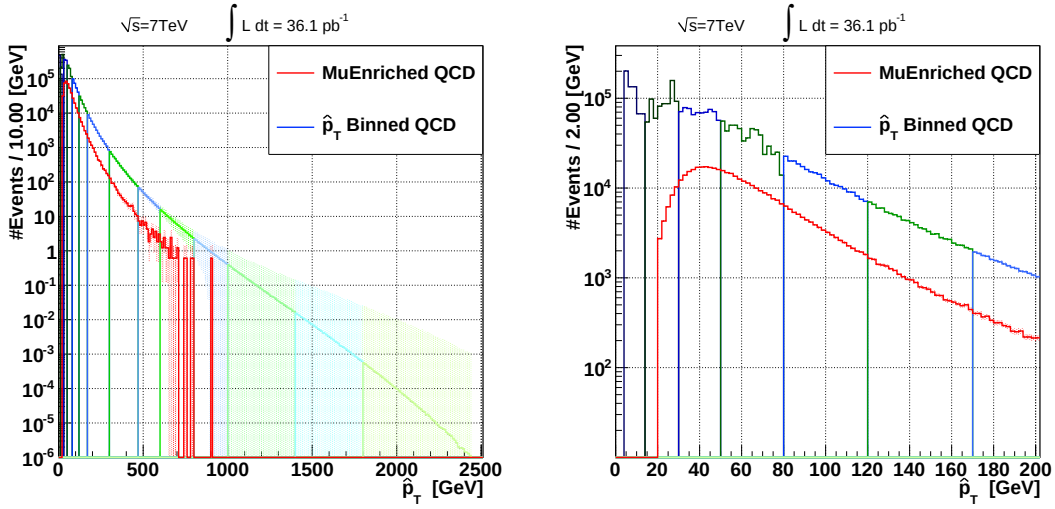

(a) (b)

Figure 5.2: Comparison of the $\hat{p}_T$ distributions for the QCD binned sample (green and blue lines) and the muon enriched QCD sample (red line). Only very loose cuts have been applied. The shaded area represents the statistical uncertainties. Figure 5.2(b) is an enlarged detail of 5.2(a).

The distributions in figure 5.2 are shown after applying only very loose cuts, so before the actual object selection of muons, electrons and jets. The events are restricted to those containing at least one muon with p_T^{μ} >15 GeV and three jets with p_T^{jet} >30 GeV, but no further selection criteria of the muons and jets have been introduced. This clarifies why the two types of QCD multi-jet MC samples show such a large difference in normalization of the $\hat{p}_T$ distribution: the reconstructed muons in the $\hat{p}_T$-binned sample are generally of lower quality than the ones from the muon enriched sample. The $\hat{p}_T$-binned samples typically also contain events in which a jet is mis-identified as a muon.

Once muon and jet selection criteria explained in section 5.3 have been applied, good agreement between both sets of MC samples is found. This is shown by two example distributions in figure 5.3. Figure 5.3(a) enlightens once more that the muon enriched QCD estimate, depicted by an

orange line, has very low statistics at energies over about 200 GeV. The pseudorapidity distribution in figure 5.3(b) shows that samples from the binned estimate with low values of p_T, i.e. high cross sections, lead to distinctive spikes due to their low statistics. These samples are depicted by dark blue and purple histograms.

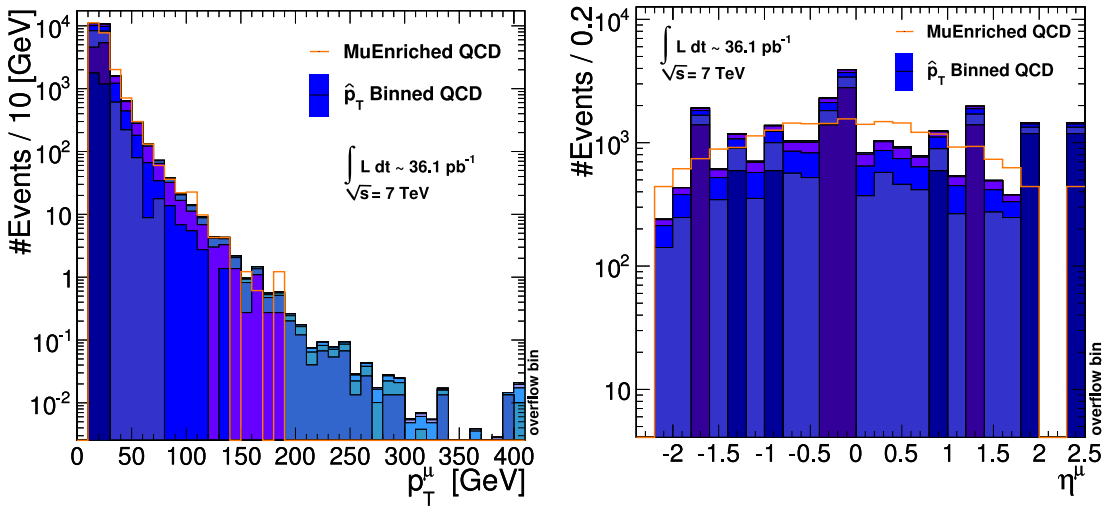

(a) (b)

Figure 5.3: Two example distributions (muon transverse momentum p_T and pseudorapidity η) for comparison of the muon enriched (orange line) and QCD binned (blue histograms) MC samples. Object selection cuts have been applied for muons, electrons, jets and $\not{E}_T$.

5.3 Object Selection

The physics objects taken into consideration in this search for supersymmetry are muons, electrons, jets and missing transverse energy. To assure a high efficiency and low misidentification rate for these objects, general selection cuts are made. Furthermore cuts are introduced to narrow down the number of events, excluding those of no interest to this analysis, and will be introduced in section 5.4. The general assumption is made that all cuts have the same influence on the simulations and on data. Dedicated efficiency studies have shown the corrections to be small [75].

5.3.1 Triggers

As described in section 4.3, triggers are imposed on the data taken at the CMS detector to select specific event topologies. The set of triggers used for this search channel requires the event to have at least one muon passing a given transverse momentum threshold i.e., $p_T^\mu = 9\,\text{GeV}$ for the HLT_Mu9. Due to a growing instantaneous luminosity the prescale i.e., the relative number of events passing the respective trigger and being recorded, increases over time. Hence a prescale of 10 means that only every 10^{th} triggered event is also saved. Figure 5.4 depicts the development of the prescale for the applied triggers over the course of the 2010 data taking. The trigger shown with the highest threshold, $p_T^\mu > 15\,\text{GeV}$, remains unprescaled throughout the entire data-taking period in 2010.

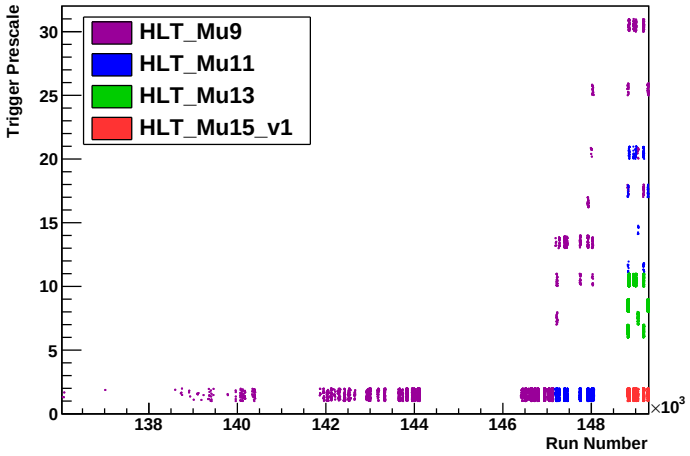

Figure 5.4: Evolution of the trigger prescale for the single muon trigger in 2010 data.

5.3.2 Muons

To select good muons the following cuts are applied and the muons passing them will be referred to as *loose* [76]. To reject events that have been triggered by fake muons, the triggering muon is required to pass a number cuts. These are summarized in the following list and will be explained in more detail in the next paragraph.

- $p_T^\mu > 15\,\text{GeV}$
- $|\eta| \leq 2.1$
- global muon
- tracker muon
- $\chi^2/\text{ndof}_{global\ \mu} < 10$
- $|d_0|_{tracker\ \mu} < 0.2\,\text{cm}$
- $\#\ \text{hits}_{tracker\ \mu} \geq 11$

The first two cuts are motivated by trigger efficiencies, as shown in figure 5.5 for the LM0 signal scenario. Only muons originating directly from the SUSY decay chain, *prompt* muons, are included in these distributions. To distinguish them from muons produced in jets an angular matching is performed between the reconstructed (RECO) and the generated (GEN) muons of the Monte Carlo sample. In all cases only the leading muon of the event is taken into account. Distributions drawn in solid red lines in figure 5.5 represent all prompt muons, whereas the ones shown by dashed blue lines require the muons to fulfill the trigger strategy described above. The efficiency is determined by the ratio of both distributions, and is shown for each individual trigger, as well as the complete trigger strategy. Due to the sharp turn-on that can be seen in the top left portion on figure 5.5, the p_T^μ cut can be set to 15 GeV, cutting at 20 GeV would lead to a loss in signal of approximately 10%. Selecting only muons with p_T^μ >15 GeV, the efficiency in η is computed. One can see that the plateau is reached for $|\eta^\mu|$ <2.1, hence the cut value listed above. The dips in the efficiency curve reveal the structure of the muon system.

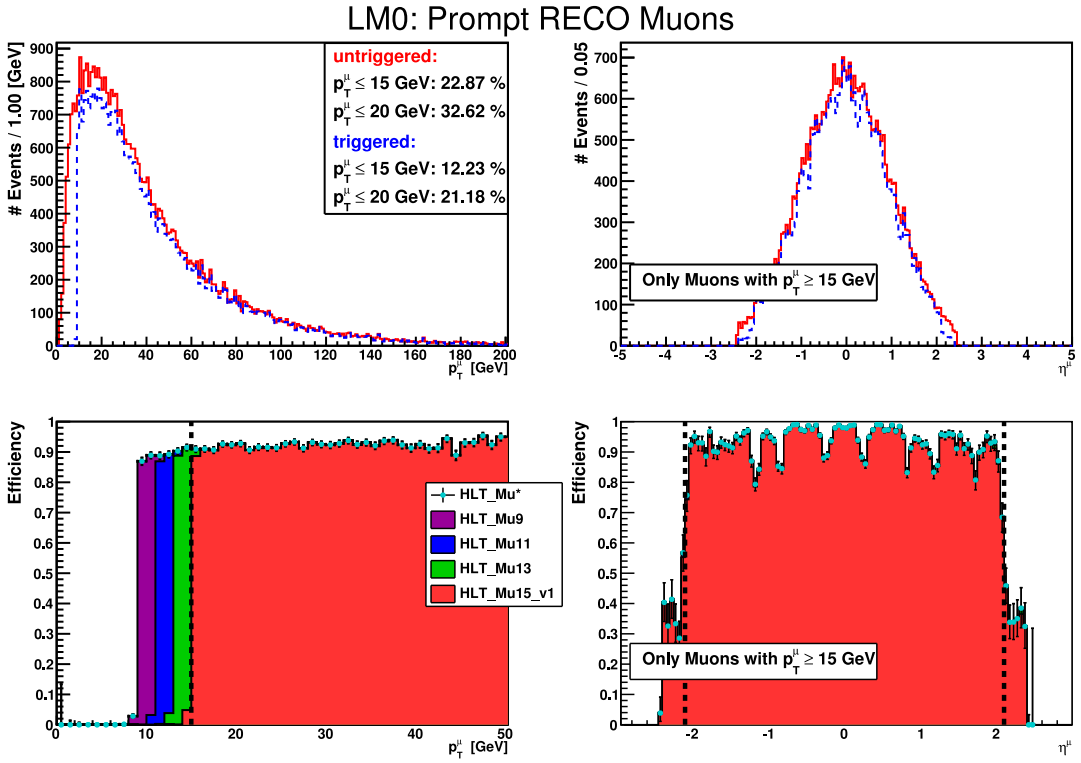

Figure 5.5: Trigger efficiencies in p_T^μ and η^μ for LM0. Distributions shown in solid red include all prompt muons, those shown in dashed blue lines include only muons that have passed the trigger requirements explained above. The colored histograms in the bottom two figures show the efficiency of the individual triggers specified in the legend, whereas the light blue dots with error bars represent the complete trigger strategy.

Effort is also put into rejecting muons originating from hadron decays in flight and muon candidates produced by so called punch-through particles, which are not muons but other particles with enough energy to induce hits in the muon system [76][77]. The quantity $\chi^2/\text{ndof}_{global\ \mu}$ describes the normalized χ^2 fit to the global muon, whereas the impact parameter $|d_0|_{tracker\ \mu}$ and the number of hits $\#\ \text{hits}_{tracker\ \mu}$ refer to the fit of the muon's track in the silicon tracker. Distributions of all three variables are shown in appendix A.

For the final analysis cuts stricter requirements are applied for a so called *tight* or *isolated* muon, as motivated in [24]:

- $\text{TrkIso}^{\mu} < 6\,\text{GeV}$
- $\text{ECalIso}^{\mu} < 6\,\text{GeV}$
- $\text{HCalIso}^{\mu} < 6\,\text{GeV}$
- $\Delta R(\mu, \text{jet}_i) \geq 0.4$

The isolation variables are calculated by summing up all transverse momenta or energy inside of a cone in the corresponding detector component. For example the requirement of $\text{TrkIso}^{\mu} < 6\,\text{GeV}$ means that the sum of the transverse momenta of all tracker tracks within a specified cone around the muon may not exceed 6 GeV. The isolation in the ECal and HCal are defined respectively. In the tracker the cone is defined by $\Delta R = \sqrt{(\Delta\eta)^2 + (\Delta\phi)^2} < 0.3$, whereas $\Delta R < 0.4$ is chosen in the calorimeters. The muon itself has been removed for all three cases.

An additional ΔR cut between the muon and every jet passing the selection criteria described below is introduced to veto against muons in jets, rejecting mainly QCD background. More detailed information on the effect of this cut will be given in section 5.4.3.

5.3.3 Electrons

Electrons are selected using the following ID cuts developed by the Vector Boson Task-force (VBTF) and tuned on Spring10 Monte Carlo samples [78]. The overlap region between barrel and endcap has been excluded. The cross section of the ECal crystals in the $\eta\phi$-plane is known to be about 0.0174×0.0174 ($22\times22\,\text{mm}^2$)[34]. Consequently the pseudorapidity of the ECal superclusters η_{sc} in the overlap region can be given at five digit precision. This corresponds to 7 crystals or an angular distance of $\Delta\theta \approx 3^\circ$ between the chosen barrel and endcap region.

Barrel ($|\eta_{sc}| < 1.4442$)

- $\sigma_{i\eta i\eta} < 0.01$
- $|\Delta\phi_{\text{in}}| < 0.8$
- $|\Delta\eta_{\text{in}}| < 0.007$
- H/E < 0.15

Endcap ($1.5660 < |\eta_{sc}| < 2.5$)

- $\sigma_{i\eta i\eta} < 0.03$
- $|\Delta\phi_{\text{in}}| < 0.7$
- $|\Delta\eta_{\text{in}}| < 0.01$
- H/E < 0.07

The spread in η of energy deposited in a 5×5 ECal cluster is denoted by $\sigma^2_{\eta\eta}$ and defined as [79]:

$$\sigma^2_{\eta\eta} = \frac{\sum_i^{5x5} w_i \cdot (\eta_i - \bar{\eta}_{5x5})^2}{\sum_i^{5x5} w_i} \quad \text{with} \quad w_i = 4.2 + \ln\left(\frac{E_i}{E_{5x5}}\right) \tag{5.2}$$

where $\bar{\eta}_{5x5}$ is the mean pseudorapidity of the seed cluster. Weights w_i are introduced that relate the energy in one crystal E_i to the energy of the entire cluster E_{5x5}. The $\sigma^2_{\eta\eta}$ variable ensures that the energy deposits are collimated and not spread out over wide regions of the ECal: entries further away from the seed crystal contribute stronger to the sum than ones of the same energy that are closer. Distances in ϕ are not taken into account but projected to the η plane. The actual quantity used for the electron selection $\sigma_{i\eta i\eta}$ has a slightly different definition. $\sigma_{i\eta i\eta}$ is given in units of the mean crystal pseudorapidity position. It achieves a better performance if the reconstructed energy deposit is spread out over two 5x5 clusters separated by a crack [80][81].

The variables $|\Delta\phi_{\text{in}}| = |\phi_{\text{sc}} - \phi_{\text{in}}^{\text{extrap.}}|$ and $|\Delta\eta_{\text{in}}| = |\eta_{\text{sc}} - \eta_{\text{in}}^{\text{extrap.}}|$ represent a geometrical matching between a track reconstructed in the tracker which has been extrapolated into the ECal and the position of a supercluster. The angles at the interaction vertex $\phi_{\text{in}}/\eta_{\text{in}}$ are extrapolated to the ECal $\phi_{\text{in}}^{\text{extrap.}}/\eta_{\text{in}}^{\text{extrap.}}$ and compared to the angles of the supercluster $\phi_{\text{sc}}/\eta_{\text{sc}}$. Setting an additional bound on the ratio of energy in the HCal to that in the ECal of the seed cluster H/E ensures a good identification of electrons. Details of these variables can be found in [50].

Furthermore electrons from photon conversion are rejected by restricting the number of layers in the tracker where no hit was measured to ≤ 1 as stated in [82]. They must also satisfy $p_T^{ele} > 10\,\text{GeV}$ and have a combined relative isolation of:

$$RelIso^{ele} = \frac{\text{TrkIso}^{ele} + \text{ECalIso}^{ele} + \text{HCalIso}^{ele}}{p_T^{ele}} < 0.1. \tag{5.3}$$

The distributions for all variables used to define good electrons in the barrel and endcap regions are shown in appendix A.

5.3.4 Jets and Missing Transverse Energy

The jets and missing transverse energy $\not{E}_{\text{T}}$ used in this analysis are constructed via the particle-flow algorithm, as described in section 4.4.3. To further constrain the jet candidates the following selection is applied as recommended by the JetMET group [83] [84].

- $p_T^{jet} > 30\,\text{GeV}$
- $|\eta| \leq 2.4$
- # constituents > 1
- # $CH > 0$
- $NHF < 0.99$
- $NEF < 0.99$
- $CHF > 0$
- $CEF < 0.99$

The p_T^{jet} and $|\eta|$ cuts are set to values that ensure a well understood jet energy scale. Further cuts are introduced to reject jets reconstructed from calorimeter and readout electronics noise. They constrain quantities resulting from the particle-flow algorithm: the fractions of neutral hadrons *NHF*, charged hadrons *CHF*, neutral electromagnetic particles *NEF* and charged electromagnetic particles *CEF* within the jet, as well as the multiplicity of charged hadrons *CH* and jet constituents. The distributions for all these variables used to define good jets are shown in appendix A.

To ensure jets are not faked by muons a $\Delta R < 0.05$ veto is applied to jets passing the selection and every loose muon in the event.

Throughout the long SUSY decay chains numerous quarks and gluon jets can be produced. Requiring at least three jets exceeding the p_T threshold of 30 GeV endorses this notion. In analyses of data taken after 2010 raising the jet multiplicity to at least four jets could be sensible due to more pile-up in the events.

A loose requirement of at least 20 GeV is set on the missing transverse energy, helping to reduce the impact of detector noise and energy mis-measurements.

5.3.5 Summary of the Object Selection

Conclusively, the requirements for a preselection of interesting events are: at least one loose muon with $p_T^{\mu} > 15\,\text{GeV}$, at least three jets with $p_T^{jet} > 30\,\text{GeV}$ and $\not{E}_{\text{T}} > 20\,\text{GeV}$. Figure 5.6 shows the transverse momentum distribution of the leading muon after all these object selection cuts have been applied. The lower part of the plot represents the ratio of data and the sum of all backgrounds. One can see that the SUSY signals LM0 and LM1, shown by on orange and lime

green line, are completely overwhelmed by the SM processes. Further analysis specific cuts must be applied to suppress the background. The poor agreement between data and MC simulation is due to the very loose object selection cuts and lack of MC statistics in the tail of the distribution. Furthermore, a normalization factor for the QCD multi-jet background is determined from a later stage of the analysis. This factor accounts for the lack of precision to which the cross section of the QCD multi-jet process is known.

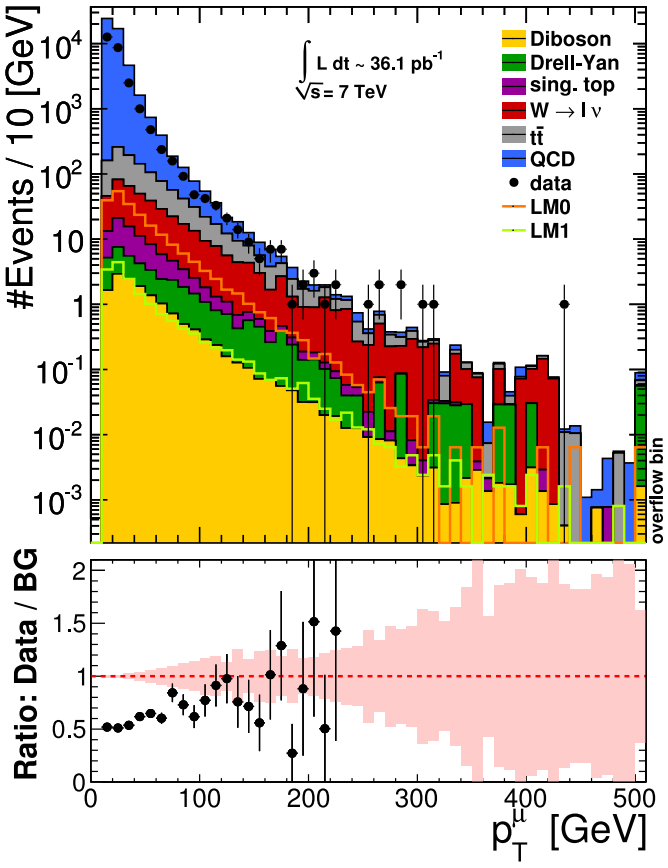

Figure 5.6: Distribution of the transverse momentum of the leading muon after object selection

5.4 Cut Based Analysis

To reduce the SM backgrounds analysis specific cuts are introduced. Figure 5.7 shows the complete set of cuts applied in succession. All cuts from the previous section 5.3 are summarized and labeled as "Object Selection". The following section will describe the additional six groups of cuts outlined in figure 5.7. Table 5.3 at the end of this chapter gives the number of events after the respective cuts have been applied for the SM backgrounds, signals LM0 and LM1 and the data.

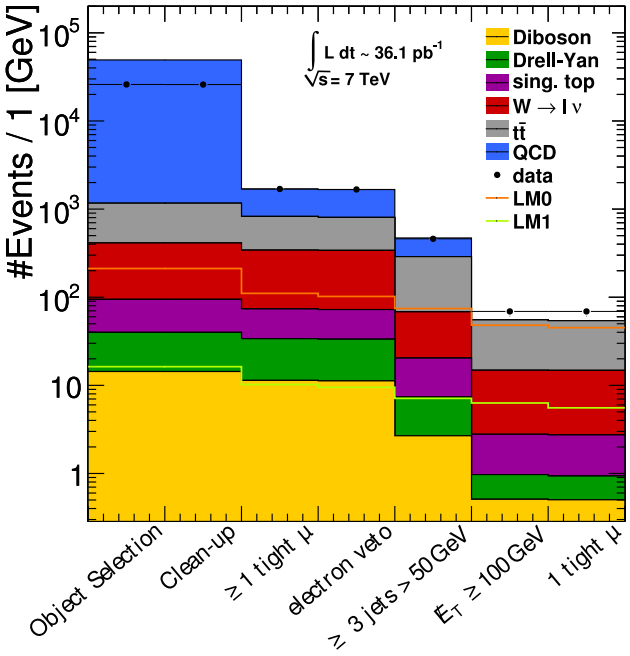

Figure 5.7: Summary of all cuts. Those already introduced in the previous section are summarized as "Object Selection".

5.4.1 Vertex and ECal Noise Cleaning

Two clean-up selections are made. A good vertex is selected by requiring that the least-squares fit made to model it has at least 5 degrees of freedom and that its position in z is no more than 23 cm away from the origin of the CMS coordinate system, which is close to the nominal beam spot. Every event is required to have at least one good primary vertex.

Secondly a procedure to exclude noise in the ECal was developed [85] and cuts are applied. The R9 variable, which is the ratio of the central cell in an 3x3 cluster and the surrounding 8 cells, points out single hot cells and is set to R9 > 0.9. At the same time the energy of this single cell may not exceed 3 GeV.

As can be seen in table 5.3 and figure 5.7 the influence these cuts have on the SM backgrounds is minor. In data only 67 events, i.e. under 1%, are rejected by this cut, since a cleaning procedure is already performed during the reconstruction.

5.4.2 Pile-Up

High values of instantaneous luminosity can cause more than two protons from the same bunch to collide, so called in-time pile-up. Consequently more than one primary vertex can be reconstructed

in the event. It is important to incorporate this effect when generating the Monte Carlo samples. Figure 5.8 shows the vertex multiplicity distribution after object selection and clean up cuts. One can see, that this specific selection of MC samples already includes pile-up events. The shapes of data and simulation agree well. The offset of about a factor 2 between data and the SM Monte Carlo estimates originates from a normalization of the QCD multi-jet cross section and will be explained in more detail in the following section.

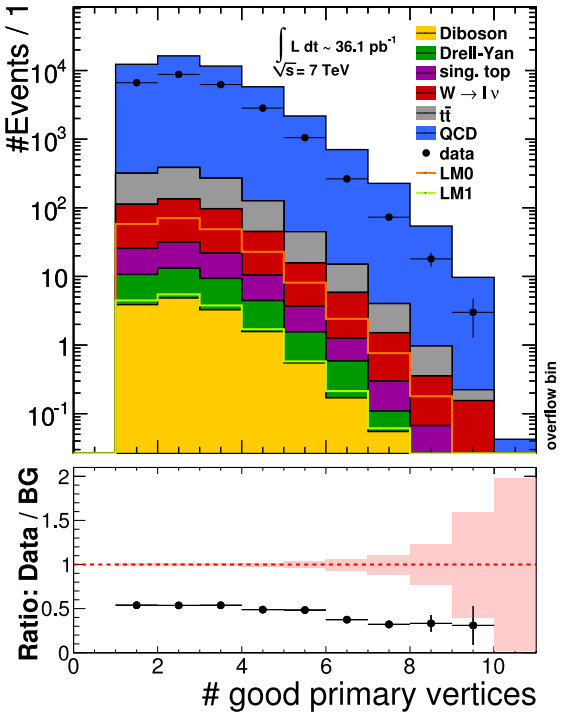

Figure 5.8: Distribution of the number of vertices after object selection cuts

Due to a higher instantaneous luminosity in 2011 a dedicated reweighting technique must be applied to the Monte Carlo samples to model the large amount of in-time pile-up events in the data. Furthermore, out-of-time pile-up originating from proton collisions of neighboring bunches must also be taken into account.

5.4.3 Tight Muons

To suppress muons originating from jets, i.e. through a hadron decay, isolation cuts on the muon are enforced by selecting only events with at least one tight muon. The respective distributions for the muon's track, ECal and HCal isolation are shown in figure 5.9 after the object selection and clean-up cuts. The vertical line represents the cut value at 6 GeV. Figure 5.10 shows the cut on $\Delta R(\mu, \text{jet}_i) \geq 0.4$ at two different stages of the analysis. Figure 5.10(a) depicts the distribution at the same level of cuts as the previous isolation plots. The cut value is clearly visible: a dip at 0.4 separates the well isolated muons from those close to or inside jets. Figure 5.10(b) shows the distribution after all analysis cuts have been applied. After the full selection only one event is left in data below 0.4. Yet it is still worthwhile to introduce this cut, since it ensures a better definition of an isolated muon at an early stage of the analysis.

These four cuts reduce the QCD multi-jet background by about two orders of magnitude. Events of $t\bar{t}$ are also reduced by over 30%. The price one has to pay for this is loosing about 50% of the LM0 and 40% of the LM1 signal.

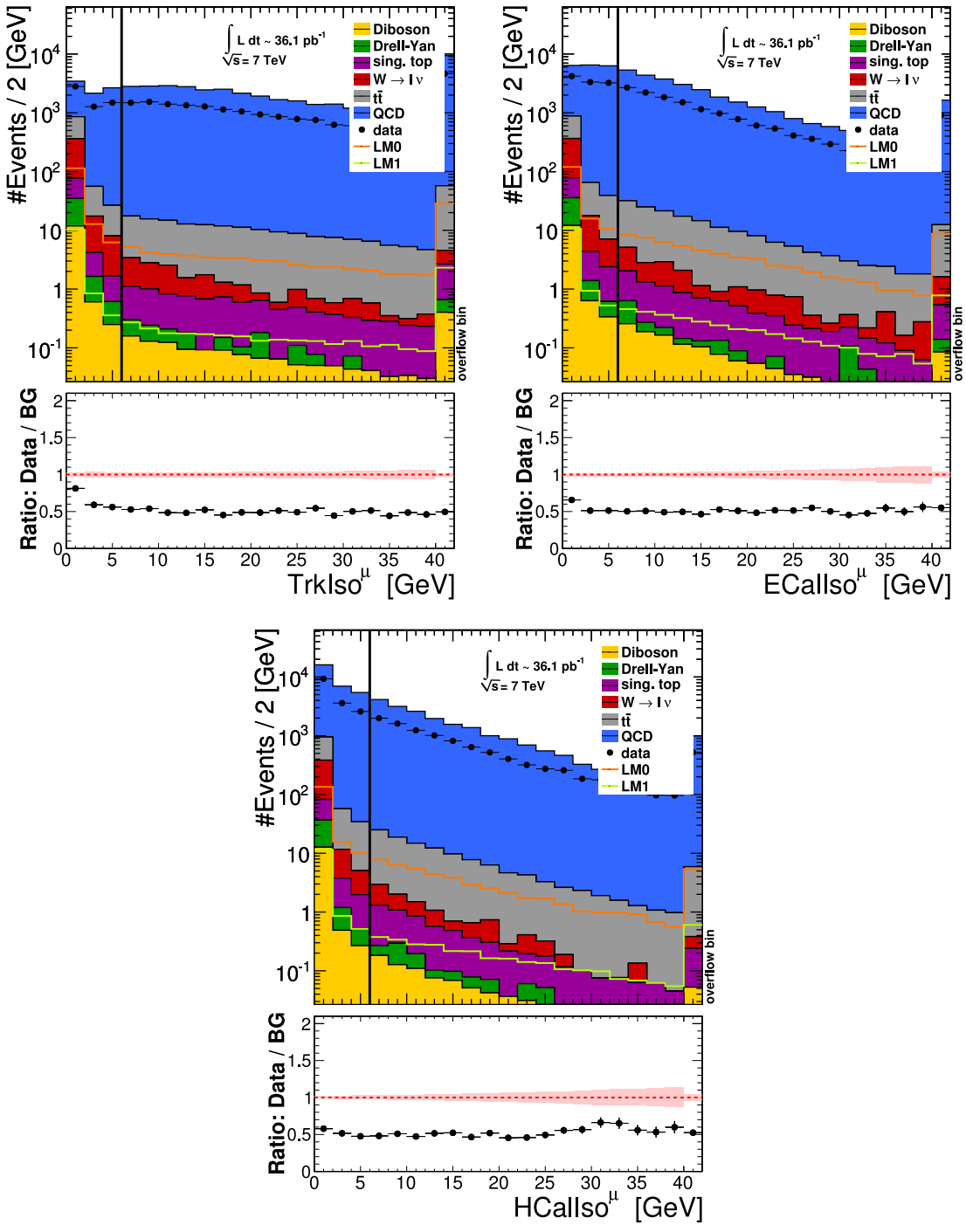

Figure 5.9: Distributions of the muon's isolation in the tracker and calorimeters. All three are cut at 6 GeV. Object selection and clean-up cuts have already been applied.

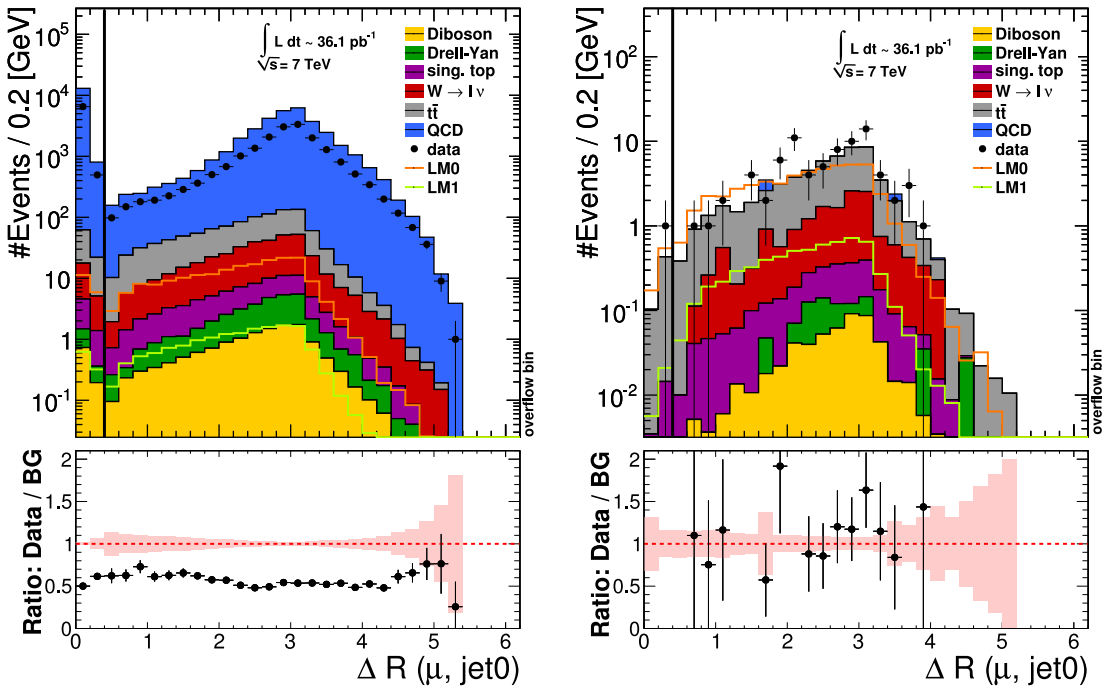

(a) (b)

Figure 5.10: Motivation of the ΔR cut between the leading muon and jet. Shown on the left after object selection and clean-up cuts and on the right after the full set of analysis cuts has been applied.

The cross sections for the QCD multi-jet production listed in table 5.2 are only given at leading order as determined during the generation of the Monte Carlo samples. For other background processes, such as the $t\bar{t}$ process, the ratio of the NLO to the LO cross section estimate can be used to determine a so called k-factor. This scaling factor can be applied to the LO cross section to account for the missing higher order corrections. For the example of the $t\bar{t}$ process the k-factor is evaluated to $k = \frac{169\,\text{pb}}{94\,\text{pb}} \approx 1.8$ [73][72]. A k-factor for the specific phase space of QCD multi-jet background used in this analysis has not been calculated yet. The normalization depends strongly on cuts used to define the event topology and kinematics.

To gain an estimate for a k-factor of the QCD background within this analysis the QCD multi-jet background is normalized to the data after object selection, clean-up cuts and the tight muon requirement have been made. At this stage of the analysis it is still the dominating background. Furthermore, the applied cuts represent a similar topology of the events as what is required in the final selection with isolated muons, several jets and missing transverse energy. The normalization scale is calculated to about 2.1 and is applied to the QCD multi-jet background throughout the entire analysis. An alternative approximation of this background is discussed in section 5.5, where a data-driven method is introduced to validate the Monte Carlo estimate and shows both to be in good accordance.

5.4.4 Electron Veto

In terms of the CMS SUSY group's strategy of independent and exclusive search channels, a veto on electrons is introduced. Only a small influence of this cut can be seen on the total number of events in table 5.3 and figure 5.7. Selecting at least one isolated muon already reduces the number of events containing electrons.

5.4.5 Tighter Jet and Missing Transverse Energy Requirements

The jet selection described in section 5.3 is now tightened by raising the p_T threshold of all three jets to 50 GeV. Due to correlations between the jets from the SUSY cascade, no individual thresholds are evaluated for the energies of the three jets. Most SM processes have a softer jet spectrum than the benchmark points. The backgrounds are reduced by about 70%, while only about 30% of LM0 are lost.

During object selection, the threshold of the missing transverse energy was set to 20 GeV. In the light of R-parity conserving supersymmetry this is a very loose cut. At the end of the decay cascade two undetectable LSPs will be produced, giving rise to substantial $\not{E}_T$. From table 3.3 one can see that for LM0 this results in at least 120 GeV of undetected energy. Since only the transverse component of the LSPs' momentum vector sum can be measured, the resulting $\not{E}_T$ will be lower than 120 GeV. The cut-value is set to 100 GeV, as is shown in figure 5.11(b). This reduces the contribution from the QCD multi-jet background to under one event. Most of this background is distributed at values of $\not{E}_T$ under 70 GeV. The LM0 signal is flat at $\not{E}_T$ values around 100 GeV, but a steep fall is observed for the backgrounds.Thus lowering the cut value will only achieve a moderate increase of signal efficiency, whilst gaining a large amount of background events.

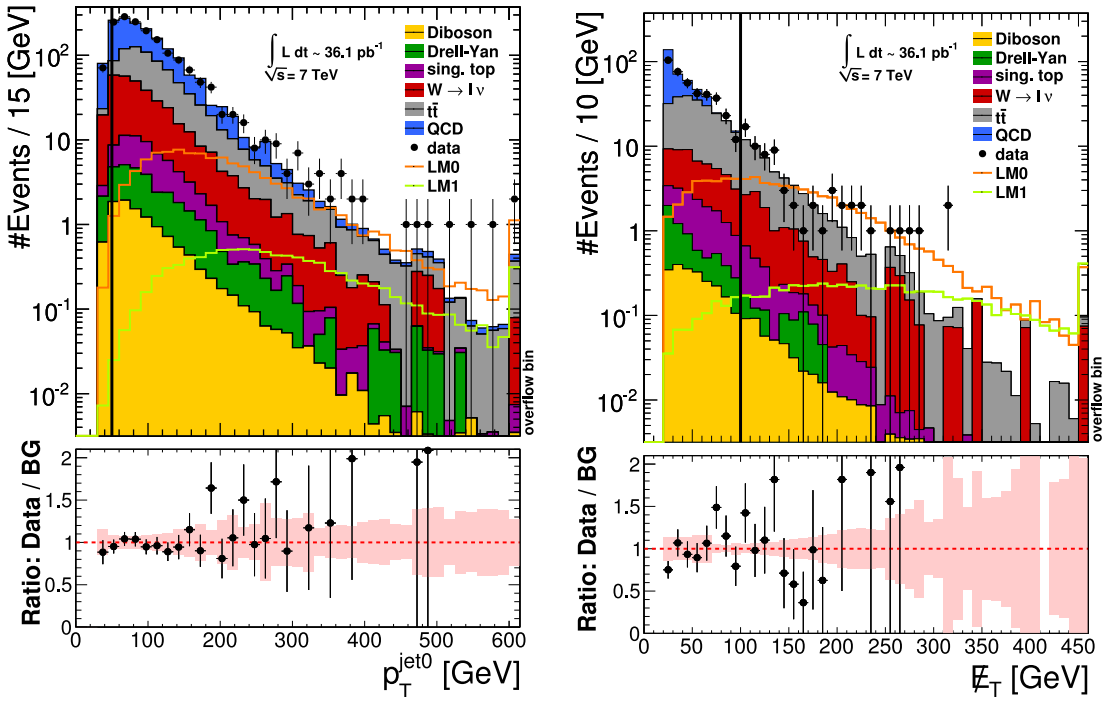

(a) (b)

Figure 5.11: (a) Motivation of the cut on the transverse momentum of all three jets, shown here is the leading jet. The respective distributions for the second and third hardest jet are given in appendix B. (b) Motivation of the cut on the missing transverse energy. Both distributions are shown after the object selection and all cuts introduced before the respective one have been applied.

5.4.6 Single Muon Requirement

In the final selection exactly one tight muon is required. Recalling that the CMS single-lepton group also pursues a search strategy with exactly one electron, one can understand that both of

these exclusive analyses can be combined more easily for a better sensitivity, without counting events twice.

5.4.7 Results

From table 5.3 one can see that the SM backgrounds have been reduced by three orders of magnitude, while keeping the LM0 and LM1 signals at a high level. After all cuts 69 events in data and 54.3 ± 1.1 in the Monte Carlo estimate are observed. The uncertainties given on the simulation is of purely statistical nature. For a more complete picture, sources of systematics must be determined. They will be explained in section 5.6. In total they account for a systematic uncertainty of about Δn_{sys}=16.3 events on the background yield. This leads to the following result in the final event selection:

$$\text{data: } 69 \text{ events} \qquad \text{vs.} \qquad \text{SM BG: } 54.3 \pm 1.1(\text{stat.}) \pm 16.3(\text{sys.}) \text{ events.}$$

The data are compatible with the Standard Model expectation. For comparison 45 events would be expected in the LM0 scenario and about 6 in the LM1 scenario in addition to the SM background. This leads to the conclusion that only LM0 can be excluded in lines of this analysis. A more detailed treatment of these final numbers will be conducted in chapter 5.7, where a Bayesian method is used to calculate exclusion limits in the m_0-$m_{1/2}$ plane.

Figure 5.12 depicts the transverse mass between the leading muon and $\not\!\!E_{\mathrm{T}}$ which is defined as [86]:

$$m_T(\not\!\!E_{\mathrm{T}}, \mu) = \sqrt{2\ \not\!\!E_{\mathrm{T}}\ E_T^{\mu}(1 - cos(\phi^{\not\!\!E_{\mathrm{T}}} - \phi^{\mu}))}. \tag{5.4}$$

The distribution is shown at object selection level on the left and in the final selection on the right. It is of interest due to the large number of events with W bosons in the background prediction. The mass peak is recognizable at about 80 GeV. The data and Monte Carlo estimate are in good agreement. No data is observed in the region over 140 GeV in the final selection.

Over the entire range of the distribution less than one event is expected in the QCD Monte Carlo estimate. To validate this number a data-driven technique for this background will be developed in section 5.5.

Figure 5.13 shows an event in the CMS detector that has passed all selection criteria. It was created using the Fireworks event display [87]. The muon system is depicted in pale red and blue, hits are shown by more saturated colors. The ECal and HCal towers are also shown in red and blue. Reconstructed charged particle tracks are shown by green lines in the tracker.

An isolated muon with a transverse momentum of about 36 GeV was reconstructed with four entries in the muon drift tube chambers. The muon's fit is shown by a red line. Only tracks exceeding 3 GeV and jets with a p_T greater than 50 GeV are depicted in the figure. Three particle flow jets, each with a transverse momentum of about 150 GeV can be found in the event, depicted by yellow cones with the jet axis extended to represent the amount of energy of the respective jet. Furthermore, missing transverse energy of about 121 GeV was also reconstructed with the particle flow algorithm and is shown in figure 5.13 by a red arrow.

Two of the jets are rather close together, but the individual jets can still be identified. These two jets are more or less back-to-back to the system of the muon and $\not\!\!E_{\mathrm{T}}$. Calculating the invariant mass of the of the first and second jet gives a value of about 115 GeV. This leads to the assumption that they might originate from a Z boson decay.

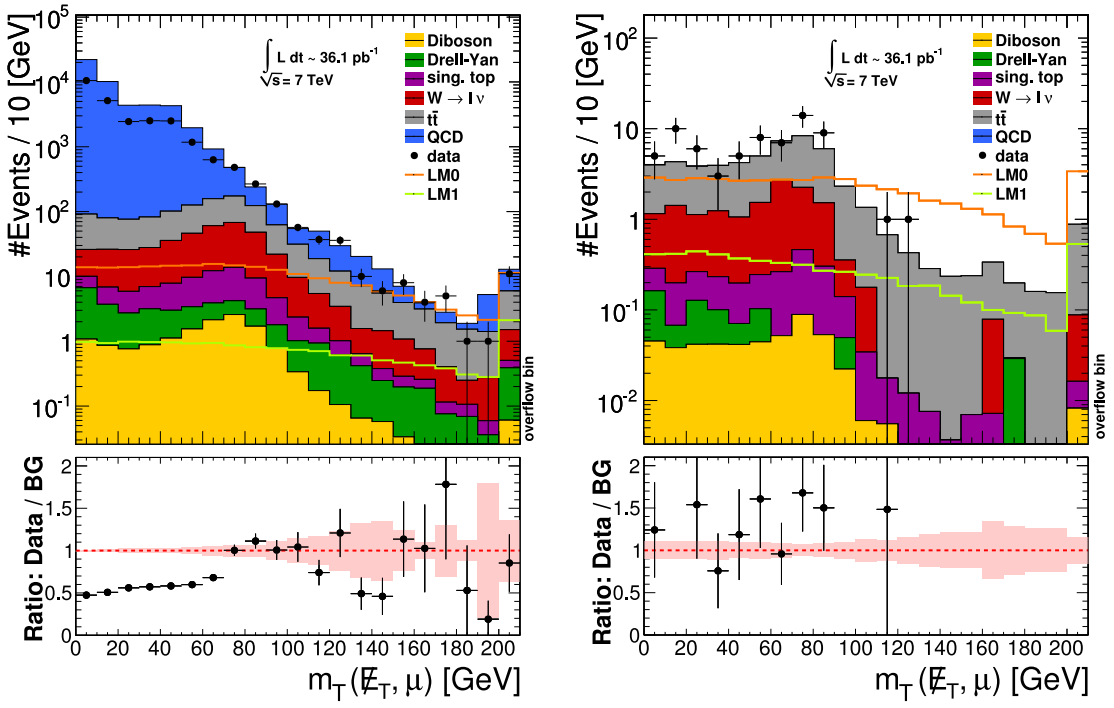

(a) (b)

Figure 5.12: Distribution of the transverse mass between $\not{E}_T$ and the leading muon (a) after object selection (b) in the final selection.

	Object Selection	Clean-up	$\geq$1 tight μ	electron veto	$\geq$ 3 jets $>$50 GeV	$\not{E}_{\mathrm{T}} \geq$100 GeV	1 tight μ
Diboson	14.351 ± 0.094	14.345 ± 0.094	11.376 ± 0.085	11.228 ± 0.085	2.677 ± 0.041	0.509 ± 0.018	0.503 ± 0.018
Drell-Yan	25.57 ± 0.86	25.57 ± 0.86	22.44 ± 0.80	22.15 ± 0.79	4.68 ± 0.37	0.46 ± 0.12	0.43 ± 0.11
sing. top	54.66 ± 0.26	54.64 ± 0.26	39.76 ± 0.22	39.05 ± 0.22	13.02 ± 0.13	1.810 ± 0.046	1.800 ± 0.046
$W \to l\nu$	317.8 ± 4.8	317.7 ± 4.8	268.5 ± 4.4	267.6 ± 4.4	47.9 ± 1.9	12.05 ± 0.93	12.05 ± 0.93
$t\bar{t}$	754.0 ± 2.0	753.7 ± 2.0	483.8 ± 1.6	464.8 ± 1.6	220.4 ± 1.1	40.47 ± 0.46	39.34 ± 0.45
QCD	$(481.2 \pm 2.7) \cdot 10^2$	$(481.0 \pm 2.7) \cdot 10^2$	866 ± 36	862 ± 36	182 ± 17	0.151 ± 0.063	0.151 ± 0.063
$\sum$ BGs	$(492.9 \pm 2.7) \cdot 10^2$	$(492.7 \pm 2.7) \cdot 10^2$	1692 ± 36	1667 ± 36	470 ± 18	55.5 ± 1.1	54.3 ± 1.1
Data	25965	25898	1692	1671	460	69	69
LM0	211.8 ± 1.2	211.7 ± 1.2	110.55 ± 0.84	102.02 ± 0.81	74.43 ± 0.69	48.15 ± 0.56	45.14 ± 0.54
LM1	16.29 ± 0.11	16.29 ± 0.11	10.213 ± 0.091	9.513 ± 0.088	7.116 ± 0.076	6.306 ± 0.071	5.555 ± 0.067

Table 5.3: Summary of event counts for SM backgrounds, the data and two benchmark points LM0 and LM1. Each set of analysis cuts is listed individually and correspond to 5.7. All cuts of section 5.3 have been summarized in the first column. All uncertainties are purely statistical.

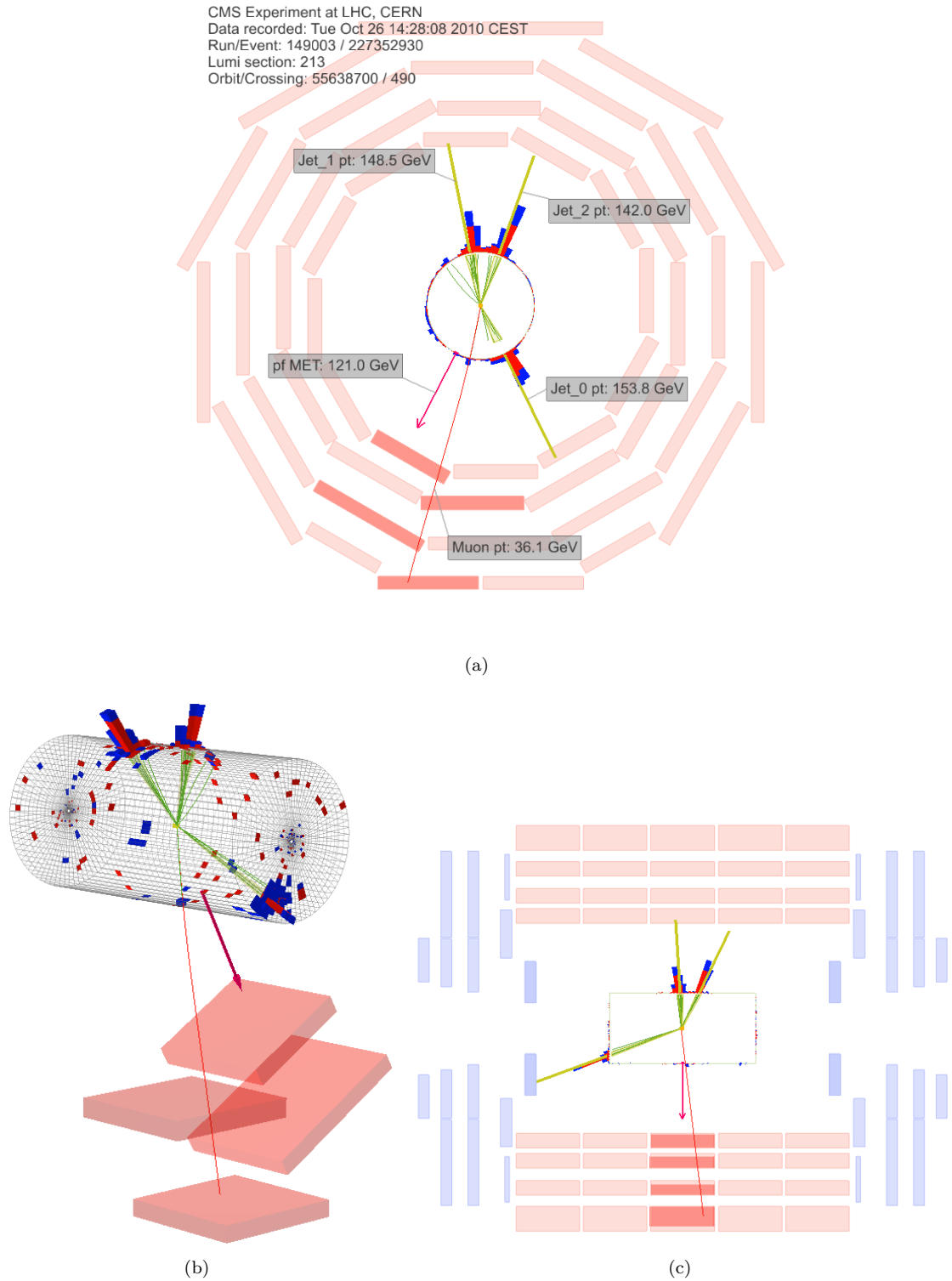

(a)

(b) (c)

Figure 5.13: Event in the CMS detector that has passed the full analysis selection with one muon (red line), three jets (yellow cones) and missing transverse energy (arrow). Figure (a) shows the detector in the r-ϕ plane, (b) gives a three dimensional view and (c) is set in the r-z plane.

5.5 Extracting QCD Multi-jet Background from Data

Despite finding the data and SM backgrounds to be in good agreement, using MC estimations for the latter, it is important to additionally estimate backgrounds with data driven techniques. The simulation of the QCD multi-jet background may lack precision or can even be incorrect, possibly hiding new physics and making the analysis unreliable. The following section illustrates a method to extract the QCD multi-jet background from data, thus becoming independent of its MC estimate. The search channel pursued in this analysis only takes QCD multi-jet events in to account that also include at least one muon. It is the dominant background at early stages of the analysis. A further step would be to also estimate the main backgrounds of the final event selection, $t\bar{t}$ and W+jets, from data, therefore becoming completely independent of the MC. However, this is beyond the scope of this thesis. A brief explanation of the data-driven method is given beforehand, followed by a detailed description with various cross-checks in the next paragraphs.

Selecting two variables that are uncorrelated in QCD background allows the plane of these two variables to be divided into the two regions shown in figure 5.14. The top region may then be used as an estimate of the bottom one by extrapolating it downwards. The extrapolation scale is obtained by normalizing the top to the bottom region according to the number of events in each region. Applying this procedure to the data returns an estimate for the QCD background, that can be used to substitute the MC simulation.

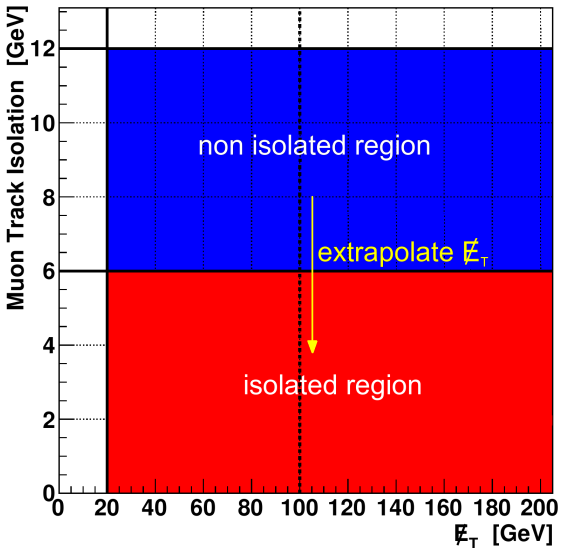

Figure 5.14: The data-driven method for QCD background in short.

5.5.1 The Method

The initial step is to determine two variables that are uncorrelated and at the same time discriminate between QCD background and signal. Choosing two fully uncorrelated variables is not realistic, so one has to resort to ones where the correlation is small. Three more or less orthogonal variables could be identified for this study: the missing transverse energy of the event $\not\!\!E_T$, the track isolation of the leading muon of the event TrkIso$^\mu$ and the angular distance between $\not\!\!E_T$ and the leading muon $\Delta\phi(\not\!\!E_T,\mu)$. In the following study $\not\!\!E_T$ and track isolation of the muon TrkIso$^\mu$ are used to extrapolate the QCD background, since they show to have a rather good discriminating power between background and signal. The $\Delta\phi(\not\!\!E_T,\mu)$ variable will be used for consistency cross-checks. Both the cut on $\not\!\!E_T$ and TrkIso$^\mu$ are released to populate the control regions. To

increase the amount of statistics the choice has been made to apply only the object selection and clean up cuts. Furthermore the $\Delta R(\mu, \text{jet}_i)$ cut has not been required for the isolated muons.

Figure 5.15 shows the distribution of the LM0 and LM1 signal estimates, QCD background and the data in the $\not\!\!E_T$–TrkIso$^\mu$ plane. The correlation factors evaluated for all four sets of events are given in the caption of the respective figure and show to be rather small. LM1 and LM0 are dominant for isolated muons over the entire $\not\!\!E_T$ range, whereas QCD background is located in the region of low $\not\!\!E_T$ but evenly distributed for all values of muon track isolation. Thus the $\not\!\!E_T$–TrkIso$^\mu$ plane can be divided into four regions, as shown in figure 5.14.

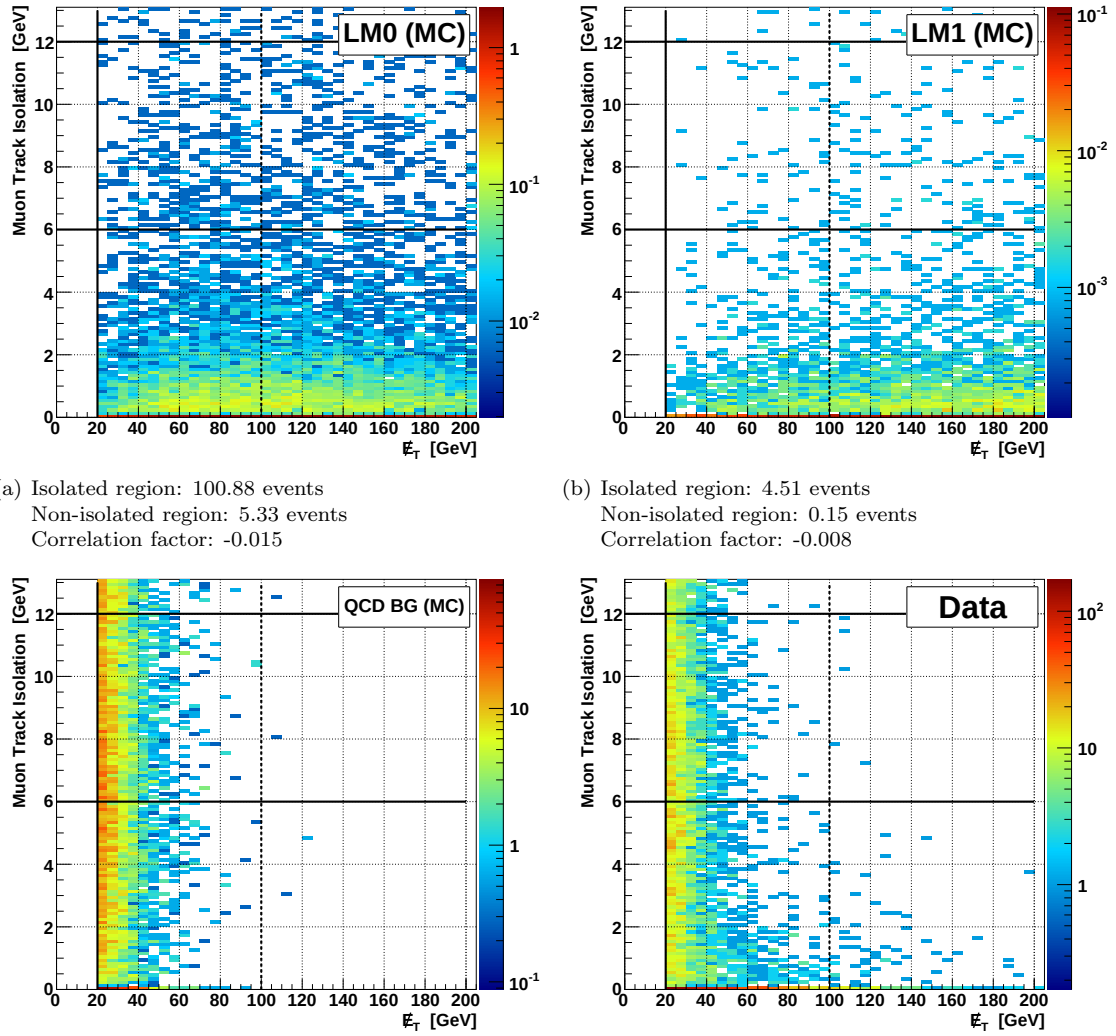

(a) Isolated region: 100.88 events
Non-isolated region: 5.33 events
Correlation factor: -0.015

(b) Isolated region: 4.51 events
Non-isolated region: 0.15 events
Correlation factor: -0.008

(c) Isolated region: 1970.88 events
Non-isolated region: 1959.07 events
Correlation factor: 0.029

(d) Isolated region: 3708 events
Non-isolated region: 2139 events
Correlation factor: -0.227

Figure 5.15: The four diagrams show the distribution of the LM0, LM1 and QCD background Monte Carlo samples and the data in the $\not\!\!E_T$–TrkIso$^\mu$ plane. The number of events for the isolated and non-isolated region are given in the caption of each diagram, along with the correlation factor between both variables.

By inverting the TrkIso$^{\mu}$ cut placed at 6 GeV, an isolated and a non-isolated region are created. Taking the observations concerning the distribution of the QCD background and signal into account, it can be assumed that the non-isolated region predominantly contains QCD background and contributions from signal are assumed to be negligible everywhere but in the isolated, high $\not\!\!E_{\mathrm{T}}$ region. Next, the electroweak backgrounds are subtracted from the data using their MC estimates. The non-isolated region can be used to approximate the QCD background in the tight region by applying a scaling factor. This extrapolation scale is evaluated from the $\not\!\!E_{\mathrm{T}}$ distribution, using the ratio of the number of events in the isolated and non-isolated region in an interval of $\not\!\!E_{\mathrm{T}}$=20 to 100 GeV:

$$scale = \frac{\#\text{ isolated } \mu \text{ events}(20\,\mathrm{GeV} < \not\!\!E_{\mathrm{T}} < 100\,\mathrm{GeV})}{\#\text{ non-isolated } \mu \text{ events}(20\,\mathrm{GeV} < \not\!\!E_{\mathrm{T}} < 100\,\mathrm{GeV})}. \tag{5.5}$$

Extrapolated events are not used twice in the analysis, since cuts are made for the final event selection at $\not\!\!E_{\mathrm{T}}$=100 GeV and TrkIso$^{\mu}$=6 GeV, as indicated in figures 5.14 and 5.15.

Summarizing one can say that the two so called control regions with $\not\!\!E_{\mathrm{T}}$<100 GeV are set in relation to each other to determine a normalization factor. This scale is then used to extrapolate events from a region not included in the final analysis selection to the so called signal region with $\not\!\!E_{\mathrm{T}}$>100 GeV and TrkIso$^{\mu}$ <6 GeV. If this is performed with data an alternative estimate of the QCD multi-jet background can be given.

In addition it is essential to define two regions with similar sample composition. To make sure that this is the case a third orthogonal variable is determined: $\Delta\phi(\not\!\!E_{\mathrm{T}},\mu)$. Several studies, that will be presented in the following paragraphs, have shown that inverting only the muon track isolation and not the ECal or HCal isolation is a satisfactory choice for this analysis. Furthermore, best results were achieved with a non-isolated region ranging from TrkIso$^{\mu}$=6 GeV to 12 GeV, rather than using the entire TrkIso$^{\mu}$ > 6 GeV region. This choice represents a compromise between high statistics and a good agreement of the event composition in the regions of isolated and non-isolated muons.

5.5.2 Cross-Checks with QCD Monte Carlo Estimates

As a validation of the data-driven method, cross-checks are first carried out with pure QCD background MC, before actually using the data itself. The same set of Monte Carlo samples is used to model the QCD multi-jet process as explained in section 5.2. The following section will outline these self-consistency and correlation checks that are undertaken to define the parameters of the method.

To ensure the comparability of the isolated and non-isolated regions a further variable, preferable uncorrelated to the TrkIso$^{\mu}$, is chosen to compare the two isolation regions to each other. If the respective distributions from both regions exhibit a similar shape, one can assume that a satisfactory choice has been made for the cut values of TrkIso$^{\mu}$. The plots in figure 5.16 demonstrate, that the angle between the missing transverse energy and the leading muon $\Delta\phi(\not\!\!E_{\mathrm{T}},\mu)$ fulfills the requirement of a third orthogonal variable: the events are more or less uniformly distributed over the entire plane. The correlation factor for each set of points is given in the caption of the respective figure and is generally small. One can expect to find isolated and non-isolated muons over all ranges of $\Delta\phi(\not\!\!E_{\mathrm{T}},\mu)$.

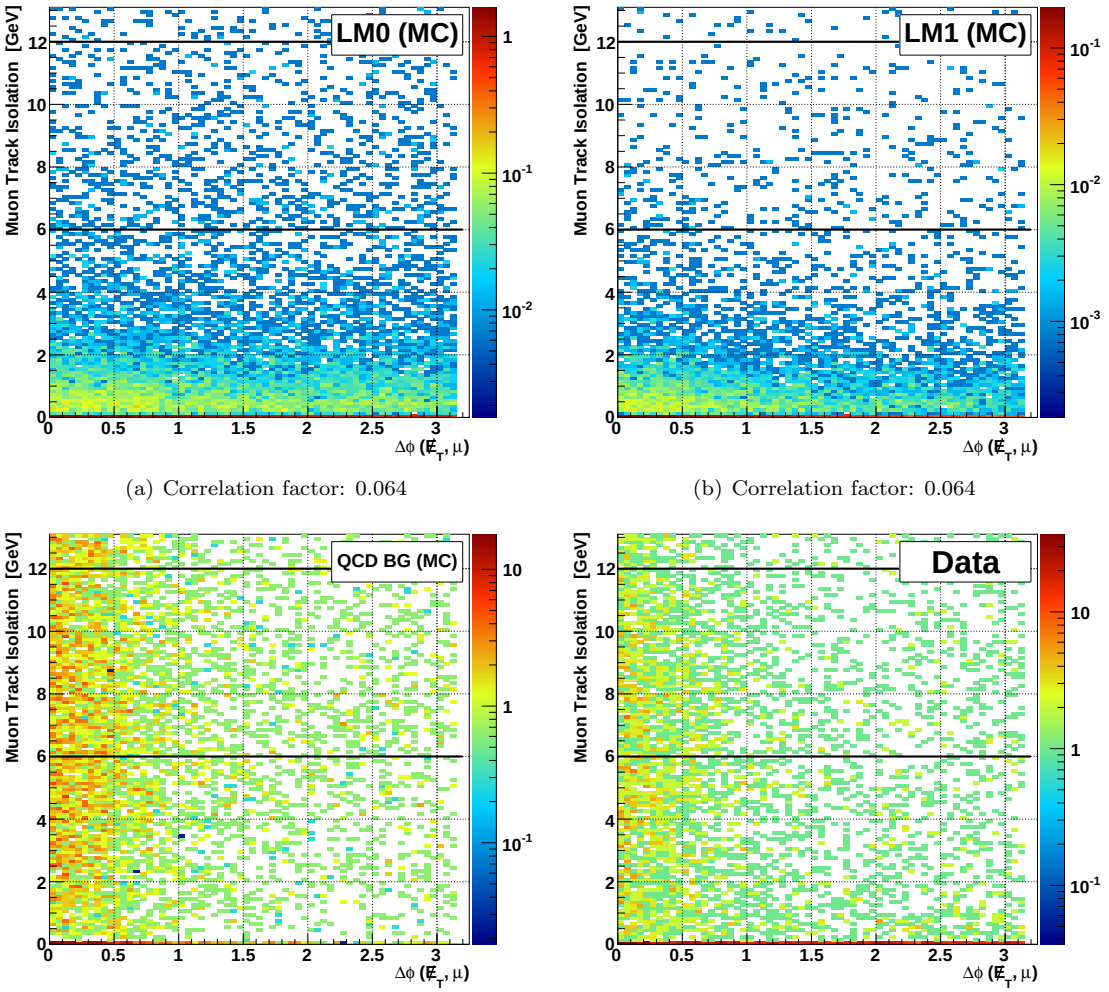

(a) Correlation factor: 0.064

(b) Correlation factor: 0.064

(c) Correlation factor: 0.021

(d) Correlation factor: -0.078

Figure 5.16: The four diagrams show the distribution of the LM0, LM1 and QCD background Monte Carlo samples and the data in the $\Delta\phi(\not\!\!E_{\mathrm{T}},\mu)$–TrkIso$^{\mu}$ plane. The correlation factor between both variables is given in the caption of each diagram.

Figure 5.17(a) shows the comparison of both regions in $\Delta\phi(\not{E}_T,\mu)$. The distribution of non-isolated events, shown by orange markers, has been normalized to the area of the tight muon events, depicted in blue. Their shapes agree well over the entire range of $\Delta\phi(\not{E}_T,\mu)$. This verifies the muon isolation values chosen to define the non-isolated region.

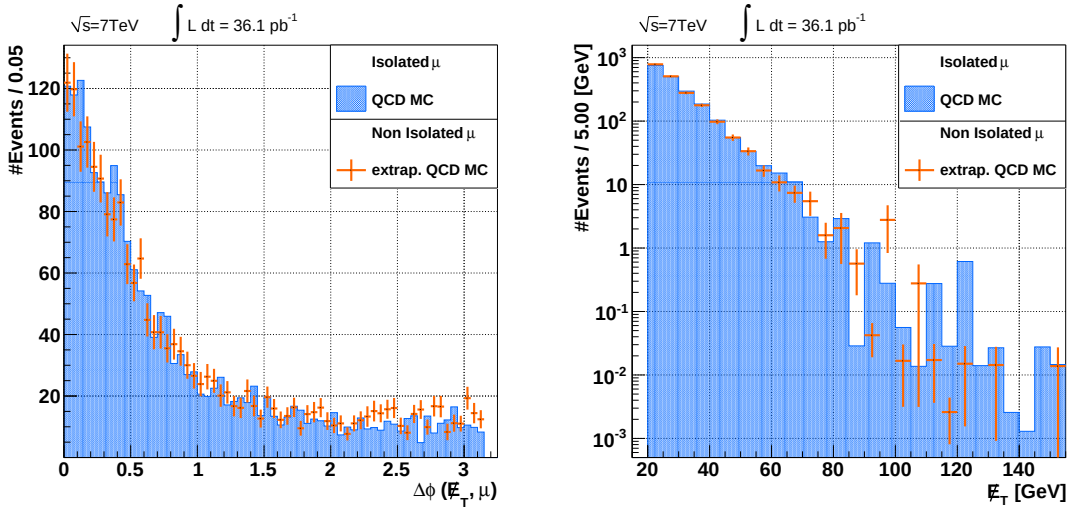

(a) (b)

Figure 5.17: Cross-checks of the QCD extrapolation with MC simulation. Events with tight muons are depicted in blue, non-isolated muon events by orange markers.

The next step is to cross-check the $\not{E}_T$ distribution, which is used for the actual extrapolation. The scale from equation 5.5 has been applied to the non-isolated events. As shown in figure 5.17(b), good agreement within the statistical errors can be found here as well. The high statistics achieved in QCD MC simulation have shown to be a great profit for both cross-checks.

To justify the assumptions made earlier about negligible correlations between all three variables a closure test is performed, which is shown in figure 5.18. Excluding correlations between the track isolation of the muon and the missing transverse energy is done by subtracting the $\not{E}_T$ distribution of extrapolated non-isolated events from the $\not{E}_T$ distribution of isolated events: $\not{E}_T^{iso} - \not{E}_T^{extr}$. The result can be fitted by a straight line, shown in red in figure 5.18. The slope of this line is sufficiently small, so the resulting points show to fluctuate around an almost constant value close to zero along the abscissa. One can conclude that events with and without tight muons are fairly evenly distributed over the $\not{E}_T$ range. To analyze the correlation between $\Delta\phi(\not{E}_T,\mu)$ and $\not{E}_T$, this procedure is performed separately for events where $\Delta\phi$ between the leading muon and $\not{E}_T$ is lower or greater than 1.5. The respective $\not{E}_T$ distributions actually used for the closure test can be found figure C.1 of appendix C. The exact value of the $\Delta\phi$ cut is only important in terms of comparable statistics for the two sub-sets. Both tests are shown in figure 5.18 and deliver similar results. Strong correlations between $\not{E}_T$ and $\Delta\phi(\not{E}_T,\mu)$ can thus be excluded.

To gain a better understanding of the muon's isolation properties in QCD multi-jet background a brief study concerning jet flavors is done with QCD MC simulation. By performing an angular matching in $\Delta\eta$ and $\Delta\phi$ the muon is matched to the jet it was produced in. The jet can in turn be matched to the initial quark before the fragmentation and hadronization processes. Thus, the quark flavor composition of the event can be estimated. The results are given in figures 5.19(b) - 5.19(d) and binned in the muon's track, ECal and HCal isolation. Each bin represents the relative fractions of jet flavors. Due to the large number of muons or jets that could not be matched there are strong statistical fluctuations. The absolute distributions of jet flavor vs. muon isolation, including the unmatched events, can be found in figure C.2 of appendix C. One can see that the

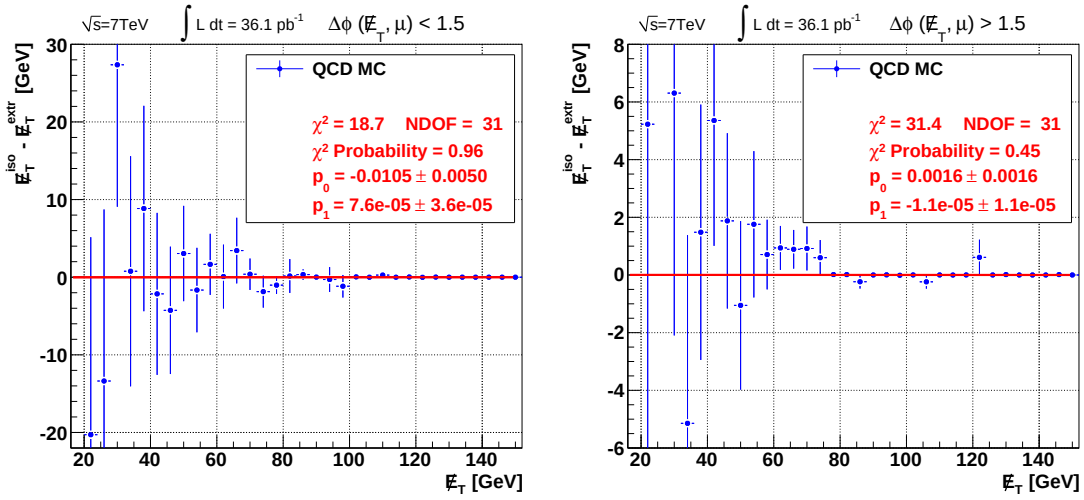

Figure 5.18: Closure test using QCD MC estimates. A straight line has been fitted to the resulting points and is shown in red. The corresponding fit parameters are given in the legend. (a) Depicts events with $\Delta\phi(\not{E}_{\mathrm{T}},\mu)$<1.5 and (b) those with $\Delta\phi(\not{E}_{\mathrm{T}},\mu)$>1.5.

largest contributions are gluon and b-jets. Light quarks are almost negligible. Unfortunately, a large amount of muons go unmatched and it is therefore difficult to make an exact prediction.

All three distributions in figure 5.19 are rather flat, so no systematics arise from the flavor of the jets. One would expect the choice of the non-isolated region to be fairly independent of cuts on any of the muon isolation variables. For test purposes all three isolation cuts were inverted at 6 GeV to form the region shown in yellow in figure 5.19(a). This would increase statistics dramatically. The red cube labeled Non-Isolated 1 represents the region originally chosen, inverting only the track isolation of the muon.

Using QCD MC events in which all three isolation cuts are inverted up to energies of 12 GeV, the cross-checks previously explained are evaluated once more, which leads to the unsatisfactory result shown in figure 5.20. The $\Delta\phi(\not{E}_{\mathrm{T}},\mu)$ distribution in QCD MC shows a strong dependency on the isolation region. A clear excess of events with non-isolated muons can be seen at the range around zero and π.

Further investigation leads to the conclusion that this behavior originates from mis-measurements in the calorimeters, as outlined by a schematic drawing in figure 5.21. If the energy of jets surrounding non-isolated muons is not measured precisely, the surplus or deficit in energy is reconstructed as $\not{E}_{\mathrm{T}}$. Too little energy will result in $\not{E}_{\mathrm{T}}$ in the direction of the muon and too much energy will produce $\not{E}_{\mathrm{T}}$ back-to-back with the muon. This cannot happen if the muon is separated from the jet, i.e. isolated.

Inverting only the isolation measured in the HCal showed to have a stronger effect than inverting only the ECal isolation. This reflects the difference in the amount of energy deposited in both detector components. Most of the jet's energy is measured in the HCal, so a mis-measurement in this detector component will lead to a higher absolute value than in the ECal. Furthermore the resolution of the HCal is lower than that of the ECal, so a mis-measurement will lead to a stronger deviation from the actual jet energy value than in the ECal.

For the proposed method of estimating QCD background from data best results are attained by solely inverting the muon isolation measured in the tracker. The tight muon cuts should be used for the HCal and ECal isolation.

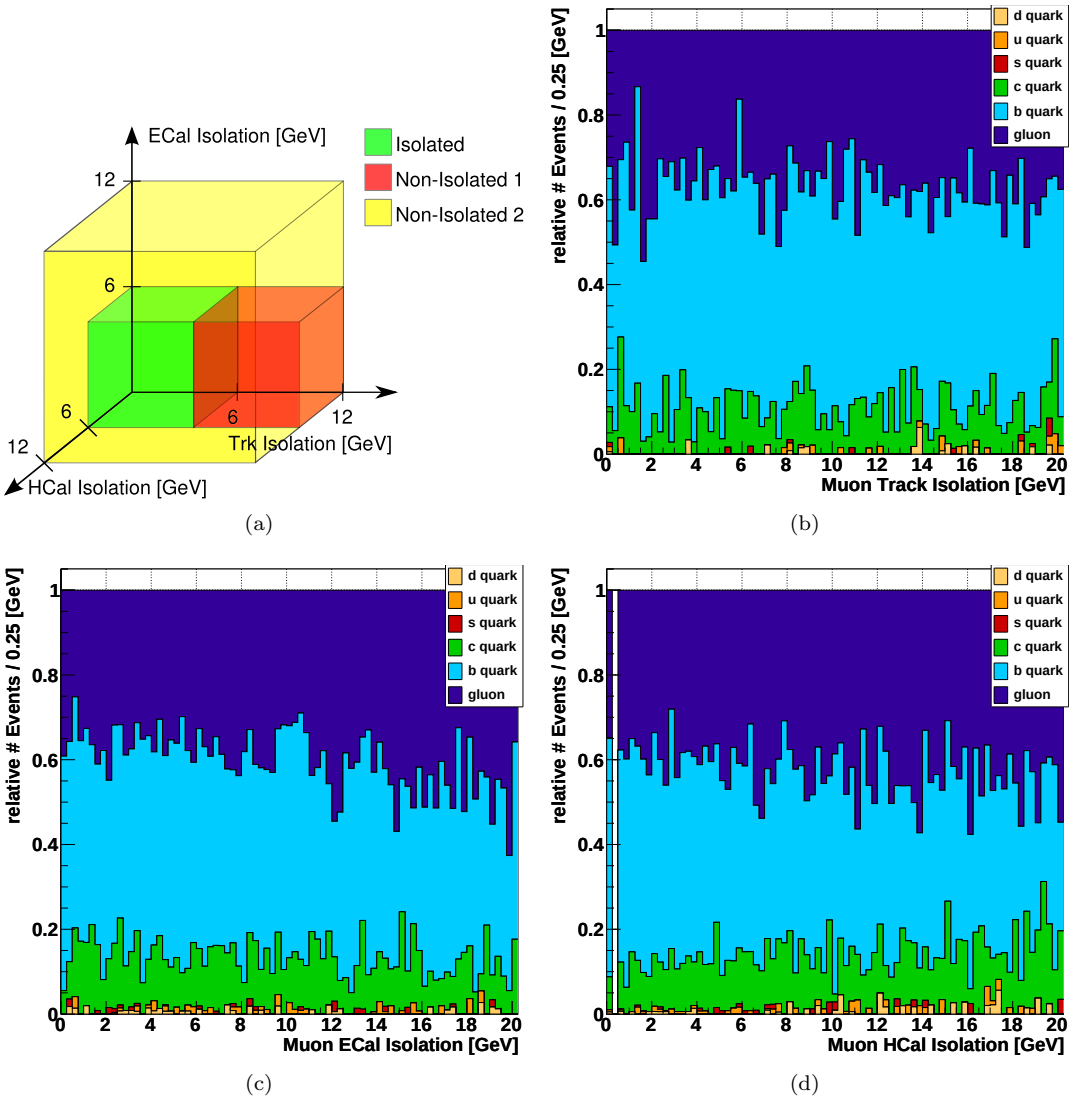

Figure 5.19: Figure (a) illustrates the two investigated regions of events with non-isolated muons. Figures (b), (c) and (d) depict the jet flavors binned in track, ECal and HCal isolation of the leading muon shown for the QCD MC estimate. The relative fractions of gluons, u, d, s, c and b quark are given.

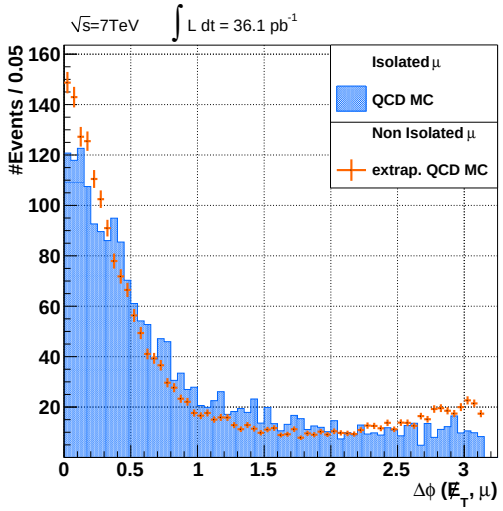

Figure 5.20: Cross-check of the QCD extrapolation with MC simulation using an alternative non-isolated region (shown in yellow in figure 5.19(a)). Events with tight muons are depicted in blue, non-isolated muon events by orange markers.

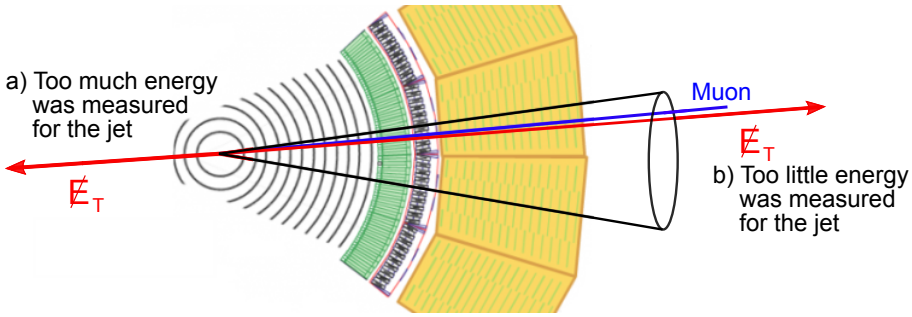

Figure 5.21: Schematic drawing of mis-measurements for non-isolated muons. The detector drawing is a modified version taken from [88].

5.5.3 Cross-Checks with Data

All MC simulation based cross-checks and the closure test have been found to be in favor of the presented method, when using the originally proposed non-isolated range. Two final cross-checks are now performed on the data. Again the $\Delta\phi(\not{E}_T,\mu)$ and $\not{E}_T$ distributions are used. They are shown in figure 5.22, which depicts the data after the electro-weak background estimates have been subtracted.

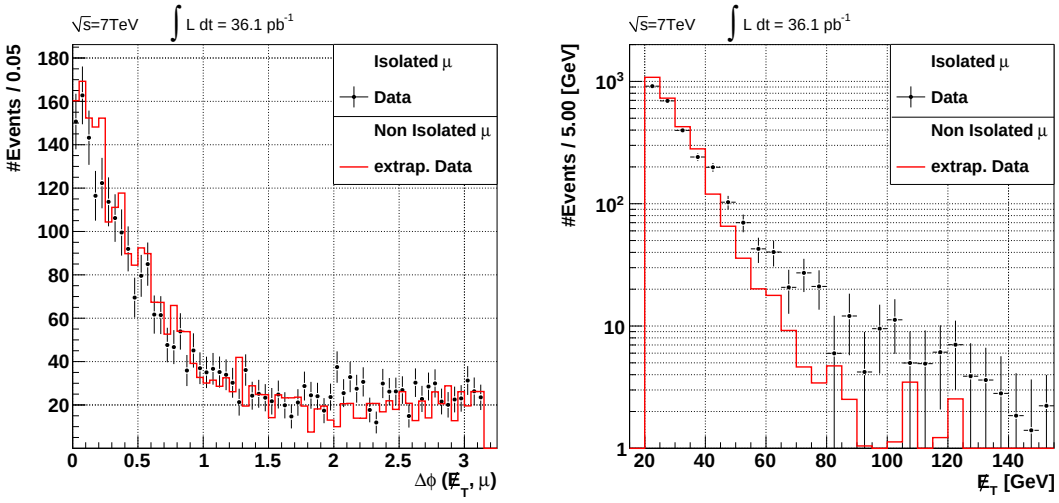

(a) (b)

Figure 5.22: Crosschecks of the QCD background estimation with the data. The contamination with electroweak backgrounds has been subtracted. Events with tight muons are depicted by black markers, non-isolated muon events by a red line.

Both distributions show a fair agreement of the isolated and non-isolated muon events. Subtracting the MC estimates of the $t\bar{t}$, single top, Diboson and Drell-Yan backgrounds from the data improves the situation by far. Figure C.3 of appendix C shows the respective distributions before reducing the contamination with electro-weak backgrounds, where much larger discrepancies are found between the two isolation regions.

Unfortunately, using MC samples to correct the data does not constitute a fully data-driven technique. Ideally, data-driven estimates of these backgrounds should be used for the subtraction. A technique for extracting the $t\bar{t}$ and W+jets backgrounds from data is presented in [89].

5.5.4 Results

The developed method is now used for the final selection, applying all cuts introduced in sections 5.3 and 5.4. In conclusion the following number of events can be found in the signal region with $\not{E}_T$>100 GeV, exactly one isolated muon and at least three jets with energies over 50 GeV:

- 0.151 ± 0.063 (stat.) events using the QCD MC simulation,
- 0.65 ± 0.45 (stat.) events using the QCD MC simulation with the extrapolation method,
- 0.13 ± 0.56 (stat.) events using the data with the extrapolation method.

The uncertainty on the number of events is purely statistical. The second number represents the validation of the method with the QCD Monte Carlo simulation and show to be compatible with

the number of events expected from the pure Monte Carlo estimate. Comparing the first and third number, shows the pure QCD MC estimate to be compatible with the data estimate well within one standard deviation. This validates that less than one event of QCD multi-jet background is found in the final selection. A larger statistical uncertainty occurs when using the data-driven estimate and results from the statistics in the data.

Figure 5.23 shows a comparison of MC simulated QCD background on the left and the data-driven estimate on the right. The transverse momentum of the leading jet is depicted. An extrapolation scale of 0.39 was estimated and applied to the non-isolated data events. The upper two figures show the comparison after applying the object selection, clean-up cuts and the tight muon requirement. The normalization factor for the QCD Monte Carlo estimate has been evaluated at this level of cuts. Both versions show a good agreement between background and the data up to about 190 GeV. At higher energies fluctuations become stronger, but still show the data to be in accordance with the Standard Model. The similar behavior of the two techniques exhibits a good validation of the Monte Carlo estimate.

Figures 5.23(c) and 5.23(d) show the distribution after the full set of cuts has been applied. Less than one event of the QCD multi-jet background has passed all cuts in both cases. To guide the eye, bins containing contributions from the QCD multi-jet process are circled in red. Low statistics in the tail of the distribution lead to an only moderate agreement between the data and the Monte Carlo estimate at energies over about 200 GeV.

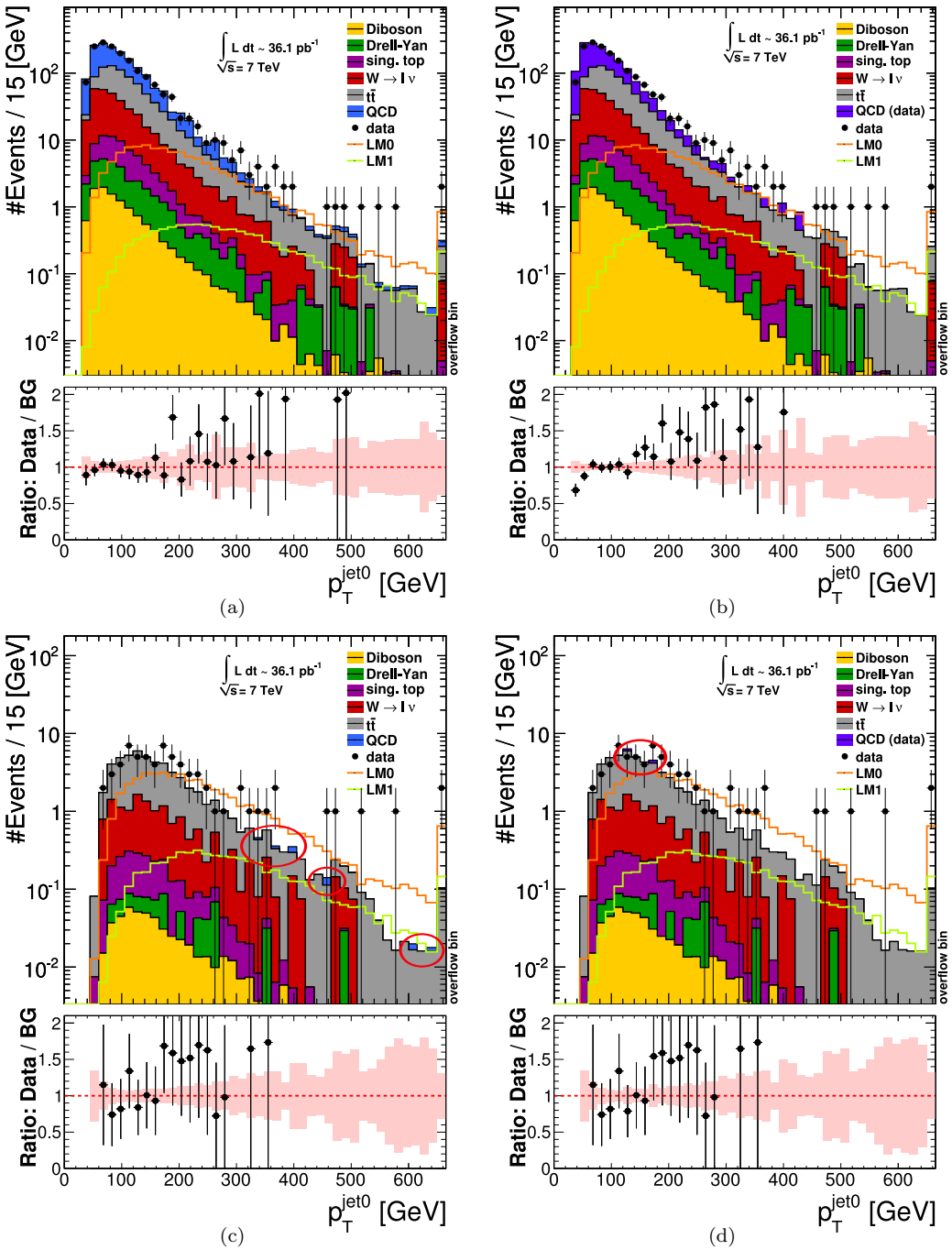

Figure 5.23: Comparison of QCD background from a Monte Carlo estimate (left) and using the data-driven technique (right). The transverse momentum of the leading jet is shown at two different stages of the analysis. Figures (a) and (b) are shown after object selection, clean-up cuts and the tight muon requirement. The QCD Monte Carlo simulation has been normalized to the data at this level of cuts. Figures (c) and (d) are shown after the full set of analysis cuts has been applied. The small remaining contributions from the QCD process are marked by red ovals.

5.6 Systematic Uncertainties

5.6.1 PDF and α_s Uncertainties

Parton distribution functions (PDFs) describe the substructure of hadrons, in particular of the proton. One cannot deduce these functions from quantum chromodynamics, but must resort to performing fits with data from fixed-target and collider experiments. Within the particle physics community several groups are devoted to estimating PDF models. The PDF4LHC Working Group has made an effort to review the PDF sets from different groups and gives recommendations on evaluating the related uncertainties [90] [91]. This working group is the source of citation for the following section if not stated otherwise. Uncertainties will be evaluated from PDF sets produced by the CTEQ[1] and MSTW[2] group following a Hessian approach [92] and from the NNPDF[3] group, which follows a Monte Carlo approach [93]. Figure 5.24 shows fit results from the MSTW group at two energy scales Q^2. For values of the momentum fraction x below about 10^{-1} the PDF of the gluon is dominant over those of the quarks.

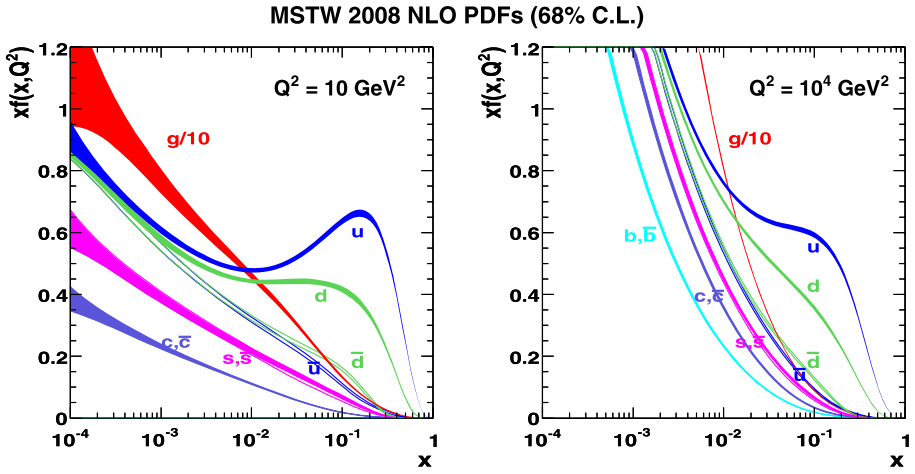

Figure 5.24: Proton PDFs estimated by the MSTW group at two values of Q^2, bands represent the 68% C.L. [94].

An analysis of hadron collider data relies on information about the PDFs, since these contribute to cross sections of all processes:

$$\sigma = \sum_{i,j} \int_0^1 \int_0^1 dx_1\ dx_2\ f_i(x_1, Q^2)\ f_j(x_2, Q^2)\ \hat{\sigma}_{ij} \tag{5.6}$$

where Q^2 is the momentum transfer between the two colliding quarks, $f_i(x_k, Q^2)$ is the probability to find a parton i with the momentum fraction x_k inside the proton and $\hat{\sigma}_{ij}$ is the cross section of the partonic subprocess. The cross section σ, expressed in equation 5.6, is used twice when generating Monte Carlo samples: first to calculate the matrix element for the hard interaction and again for modeling the parton showering. Thus it is necessary to evaluate uncertainties on the MC samples that arise from the choice of PDF model, commonly referred to as PDF uncertainties.

At values of $Q^2 \gtrsim 1$ GeV, one finds that the PDFs only depend on x_k, a property known as *Bjorken scaling*. In the course of further deep inelastic scattering (DIS) experiments deviations from this behavior were found at higher values of Q^2: the PDFs are highly dependent on the value of the

[1] **C**oordinated **T**heoretical-**E**xperimental Project on **Q**CD
[2] **M**artin-**S**tirling-**T**horne-**W**att
[3] **N**eural **N**etwork **P**arton **D**istribution **F**unction

momentum transfer Q^2. The so called DGLAP[4] equations [95] of perturbative QCD describe the PDFs as a function of x_k and the renormalization scale of QCD μ, which is chosen equal to the factorization scale μ_f. This scale is used to factorize the processes of parton shower evolution and fragmentation from partons to hadrons. By setting $\mu_f = Q$ the equations can be solved and eliminate Q^2 as an unknown parameter. Measuring the PDFs at one scale now allows a direct prediction for any other given scale.

To gain access to the x_k dependence, CTEQ and MSTW estimate fit functions to DIS, Drell-Yan and jet data, by means of a χ^2 method. The free parameters of the resulting fit function are then varied up and down to account for the uncertainties on the fit function, this produces the so called *members* or error sets of the PDF set. The central PDF set or *best fit* corresponds the point in the parameter space with the smallest value of χ^2. Since the fit parameters may be correlated these PDF uncertainty contributions must first be transformed to an orthogonal eigenvector basis. This can be done by diagonalizing the matrix of second derivatives of χ^2, the Hessian matrix. NNPDF relies on ensembles of MC samples, called *replicas*, generated from data. They are fitted by the output of neural networks, leading to the PDF replicas.

The PDFs also depend on the running value of the strong coupling constant $\alpha_s(Q^2)$, which is afflicted with a (theoretical) uncertainty. To estimate the consequences of this for the PDFs, α_s is varied by one Gaussian standard deviation $\Delta\alpha_s = 0.0012$, where the value itself is chosen differently by the three groups, but always at the Z-boson mass scale: $\alpha_s(M_Z)_{\mathrm{CTEQ}}$=0.118, $\alpha_s(M_Z)_{\mathrm{MSTW}}$=0.12018 and $\alpha_s(M_Z)_{\mathrm{NNPDF}}$=0.119.

There are two possible means of incorporating PDF and α_s uncertainties in the analysis: by the method of "brute force" or by a reweighting technique [96]. In the lines of the first method all Monte Carlo samples used in the analysis, i.e. backgrounds and signal, are produced anew with different PDF sets. The default PDF set within the CMS Collaboration is CTEQ6LL which considers leading order QCD calculations and leading order α_s corrections. The second method uses the initial Monte Carlo samples and simply reweights each event to the probability it would have with different PDF sets. This is far less time consuming than generating multiple Monte Carlo samples, moreover it refrains from increasing the resulting uncertainty due to statistical fluctuations during event generation. A disadvantage is, however, that the variations only propagate into the cross section of the hard scattering, but not the parton showering. The effect of this has been shown to be small [97][98], thus the reweighting technique is nevertheless the method chosen within the PDF4LHC recommendations.

The reweighting is performed using PDF set files and specialized analysis functions from the LHAPDF[5] group [99]. Before carrying out the cut based analysis, the Monte Carlo samples are scaled event by event. The number of events passing all cuts is the final observable $\mathcal{O}$ and the corresponding uncertainty Δn is calculated via the following formulae 5.7 - 5.10 for each PDF group individually. The CTEQ and MSTW groups supply a PDF set with N=44 and 40 members, respectively, where the best fit is included as an additional member 0. The following formulae 5.7 and 5.8 take asymmetric errors into account, where $\mathcal{O}_0^{\mathrm{pdf}}$ represents the value of the observable using the best fit PDF set. The values $\mathcal{O}_{2i-1}^{\mathrm{pdf}}$ and $\mathcal{O}_{2i}^{\mathrm{pdf}}$ correspond to the up- and downwards fluctuations of the respective fit parameter. $\Delta n^{\mathrm{Hess}}(\mathrm{PDF}, +)$ sums up the contributions that lead to larger values of the observable $\mathcal{O}$, whereas $\Delta n^{\mathrm{Hess}}(\mathrm{PDF}, -)$ does likewise for the contributions that lead to a decrease of $\mathcal{O}$. The upwards/downwards variation of a respective fit parameter does not necessarily lead to an increase/decrease of the observable. Thus, only the most positive or negative contribution, respectively, is added to the sum for each fit parameter.

$$\Delta n^{\mathrm{Hess}}(\mathrm{PDF}, +) = \frac{1}{C}\sqrt{\sum_{i=1}^{N/2}\left(\max\{\mathcal{O}_{2i-1}^{\mathrm{pdf}} - \mathcal{O}_0^{\mathrm{pdf}},\ \mathcal{O}_{2i}^{\mathrm{pdf}} - \mathcal{O}_0^{\mathrm{pdf}},\ 0\}\right)^2} \tag{5.7}$$

[4] **D**okshitzer **G**ribov **L**ipatov **A**ltarelli **P**arisi
[5] **L**es **H**ouches **A**ccord **PDF**

$$\Delta n^{\text{Hess}}(\text{PDF}, -) = \frac{1}{C}\sqrt{\sum_{i=1}^{N/2}\left(\max\{\mathcal{O}_0^{\text{pdf}} - \mathcal{O}_{2i-1}^{\text{pdf}},\ \mathcal{O}_0^{\text{pdf}} - \mathcal{O}_{2i}^{\text{pdf}},\ 0\}\right)^2} \tag{5.8}$$

Furthermore, α_s sets in which the variation by 68% is performed for the best fit PDF are available from CTEQ and MSTW. The best fit set $\mathcal{O}_0^{\alpha_s}$ is set in relation to the corresponding up- and downwards fluctuation of α_s. The resulting uncertainties can be obtained by:

$$\Delta n^{\text{Hess}}(\alpha_s, \pm) = \frac{1}{C'}(\mathcal{O}_{\pm}^{\alpha_s} - \mathcal{O}_0^{\alpha_s}). \tag{5.9}$$

The coefficients C and C' are necessary for rescaling all uncertainties to a 68% C.L. due to the PDF fit groups' different approaches. The combined PDF and α_s uncertainty within each PDF set is then obtained by the quadratic sum of the individual values.

A visualization of the impact these uncertainties have on the analysis is shown in figures 5.25 and 5.26. They depict the η distribution of the top quark for the $t\bar{t}$ background MC sample after all cuts of the analysis have been made. Additional η distributions for the $W \to l\nu$ backgrounds, LM0 and LM1 are included in appendix D. Figures on the left side show the reweighting to the different PDF sets and those on the right give information about the influence of varying α_s. The black line represents the original distribution with CTEQ6LL as the set used during MC sample production. In dark blue one can see the best fit of the respective set and the variations in light blue and green. The lower plots in each figure represent a version of the upper plots normalized to the best fit of the investigated set, as well as the uncertainty bands calculated with equations 5.7 - 5.9. For the case of CTEQ the bands are shown with and without the rescaling factor C: the PDF set members were produced at 90% C.L. and not at 68%.

One can see, that the LO PDF from the MC production is not in good agreement with the NLO sets used to estimate the uncertainties. Furthermore the determined fluctuation increases for large values of $|\eta|$. The impact of α_s is shown to be negligible in the light of varying the PDFs. A comparison of the two groups following the Hessian approach shows that the errors evaluated from the CTEQ set are generally larger than those using the MSTW sets.

The NNPDF approach differs from that of the groups using the Hessian method. The α_s variation is not performed solely for the best fit, but for all of the varying MC estimates. This results in N_{α_s}=7 sets of α_s each containing 100 replicas. The assumption is made that the value for α_s follows a Gaussian distribution and one chooses the number of replicas $N_{rep}^{\alpha_s^{(j)}}$ used from each set accordingly to determine the standard deviation via:

$$\Delta n^{\text{NNPDF}}(PDF + \alpha_s) = \sqrt{\frac{1}{N_{rep} - 1}\sum_{j=1}^{N_{\alpha_s}}\sum_{k_j=1}^{N_{rep}^{\alpha_s^{(j)}}}\left[\mathcal{O}(\text{PDF}^{(k_j,j)}, \alpha_s^{(j)}) - \langle\mathcal{O}\rangle_{ref}\right]^2} \tag{5.10}$$

where $\langle\mathcal{O}\rangle_{ref}$ is the mean over all of the used replicas.

If all replicas from the central set are used N_{rep}=300. A large set with many replicas ensures the suppression of statistical fluctuations, allowing even non-gaussian or asymmetric probability distribution to be reproduced sufficiently. This can be of great profit for the accuracy and reliability of determined uncertainties. The numbers of replicas used from each set are thus: $N_{rep}^{\alpha_s=0.116} = N_{rep}^{\alpha_s=0.122}$=4, $N_{rep}^{\alpha_s=0.117} = N_{rep}^{\alpha_s=0.121}$=25, $N_{rep}^{\alpha_s=0.118} = N_{rep}^{\alpha_s=0.120}$=71 and $N_{rep}^{\alpha_s=0.119}$=100. In total this adds up to 700 replicas.

The visualization of the reweighting technique showing the impact of the estimated uncertainties can be found in figure 5.27. Two methods were studied to select which replicas are to be used from the sets aside from the central set. First, the weighted mean is used to calculate the standard deviation, where the weights correspond to the numbers of replicas to be used from each set. The error band shown in figure 5.27(b) is calculated in this manner. It is smaller than those from CTEQ and MSTW, bearing in mind that it already combines PDF and α_s uncertainties.

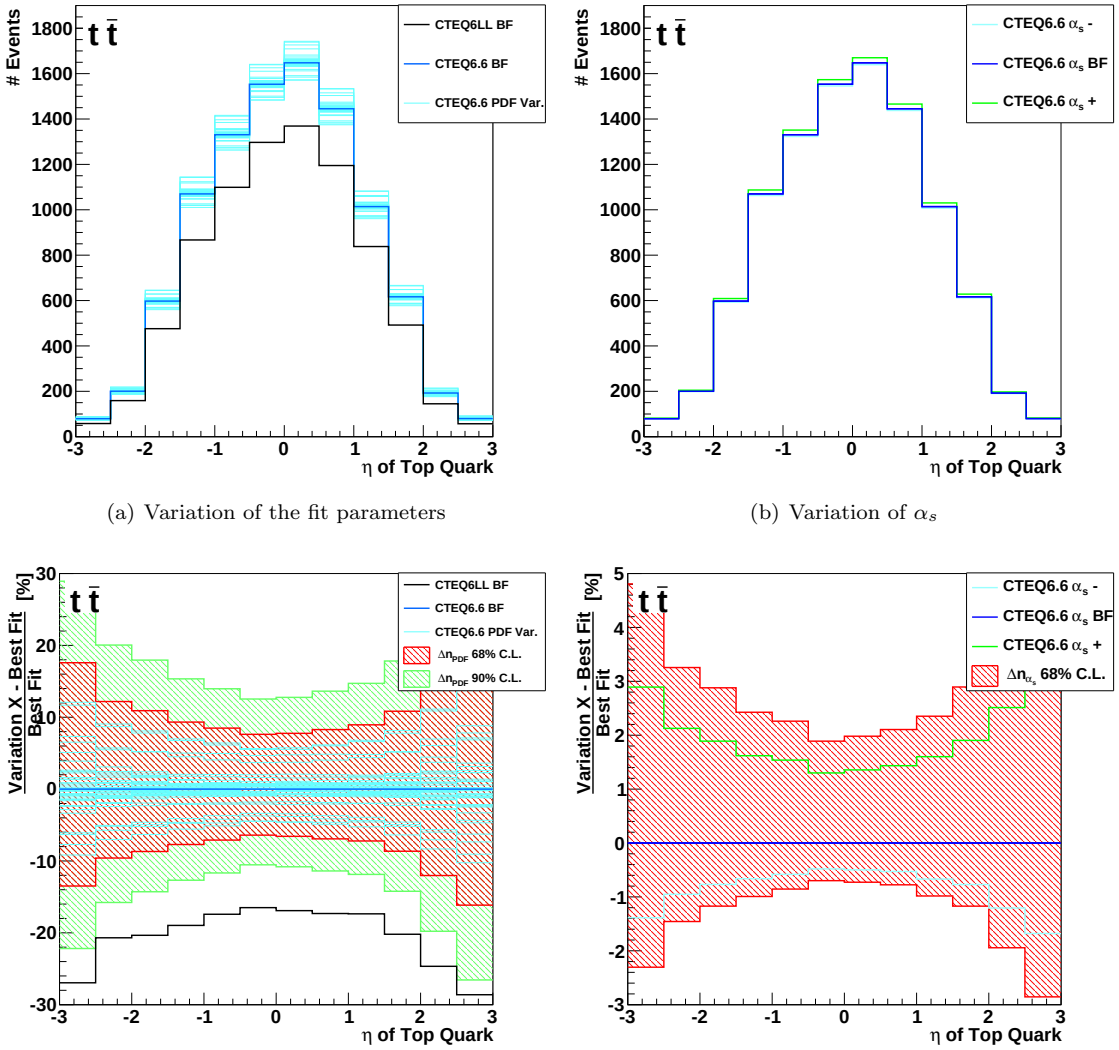

(a) Variation of the fit parameters

(b) Variation of α_s

(c) Variation of the fit parameters scaled to best fit

(d) Variation of α_s scaled to best fit

Figure 5.25: η distribution of top quark for estimation of PDF and α_s uncertainties with sets from CTEQ6.6. Entries in the legend labeled "BF" refer to the best fit member of the PDF set and "PDF Var." stands for members where fit parameters have been varied.

Alternatively, a random number generator is used to obtain $N_{rep}^{\alpha_s^{(j)}}$ unique integers. Then the correspondingly numbered replicas are used for equation 5.10. Figure D.1 in appendix D shows the result of rolling the dice one million times, where again the number of events after all cuts is the observable. To estimate the final uncertainty a Gaussian distribution is fitted in the range of $\pm 1\sigma$ around the maximum. The results are the same as those using a weighted mean calculation for all MC samples, so apparently 700 replicas supply a large enough amount of statistics.

To conclude, the relative uncertainty on the number of events after all cuts is given for all background and signal MC samples in table 5.4. The final uncertainty for each MC sample is determined by symmetrizing the envelope over all three PDF fitting groups. For the estimates of the three main backgrounds after all cuts the relative uncertainties on the number of events is evaluated to:

$$\Delta n_{PDF+\alpha_s}^{W\mu\nu} = \pm 2.4\% \qquad \Delta n_{PDF+\alpha_s}^{W\tau\nu} = \pm 2.3\% \qquad \Delta n_{PDF+\alpha_s}^{t\bar{t}} = \pm 8.3\%.$$

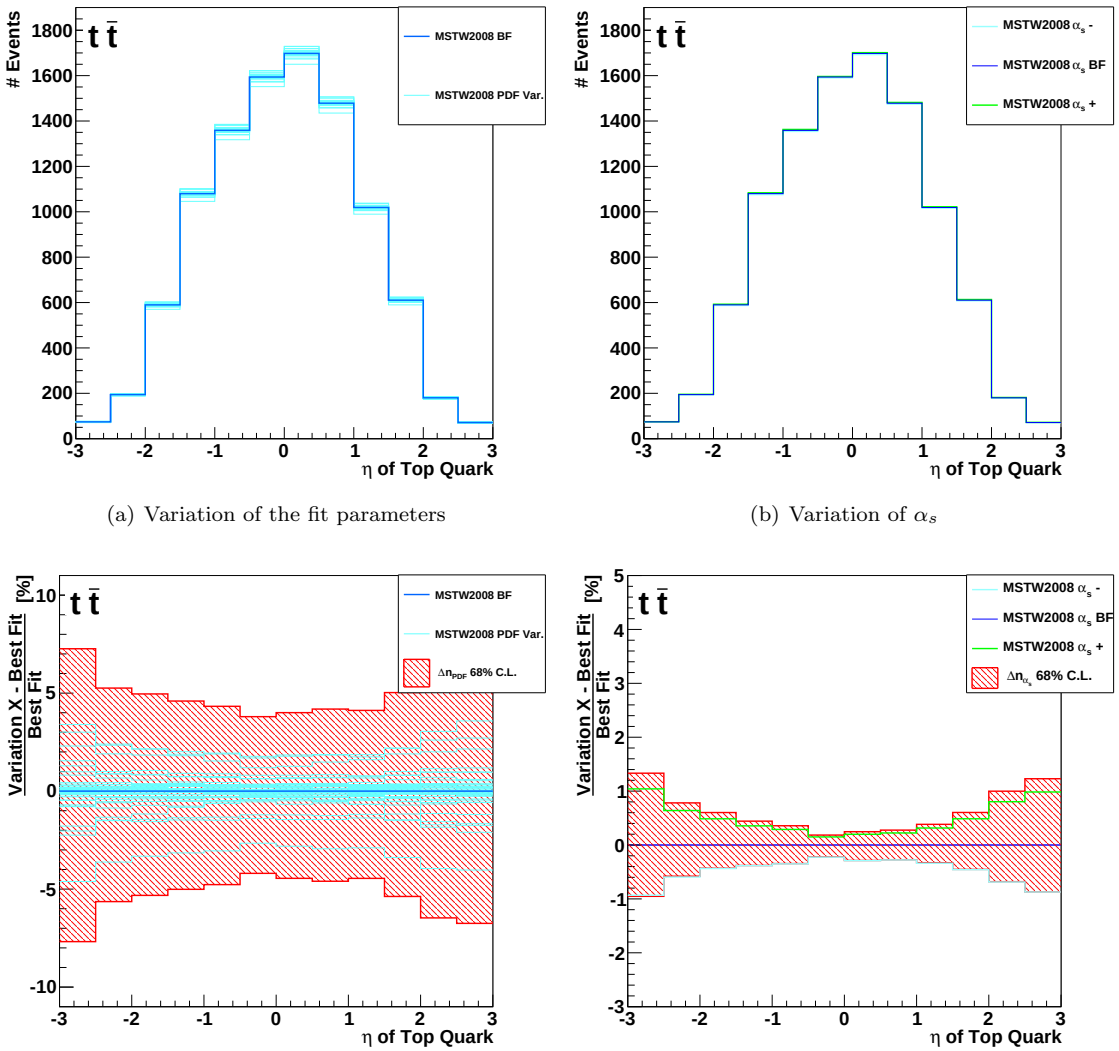

(a) Variation of the fit parameters

(b) Variation of α_s

(c) Variation of the fit parameters scaled to best fit

(d) Variation of α_s scaled to best fit

Figure 5.26: η distribution of top quark for estimation of PDF and α_s uncertainties with sets from MSTW. Entries in the legend labeled "BF" refer to the best fit member of the PDF set and "PDF Var." stands for members where fit parameters have been varied.

Using the calculated uncertainties for LM0 and LM1 as reference an uncertainty of ±10% on the number of events after all cuts is assumed for each grid point of the m_0-$m_{1/2}$ scan.

Since the PDFs are used during the Monte Carlo event generation, the resulting uncertainty must also be calculated for the number of events before cuts, i.e. number of produced events. This is once more done for LM0 and LM1 and used as an approximation. The final uncertainty on the number of produced Monte Carlo events is ±6% for each point in the m_0-$m_{1/2}$ plane. The uncertainty on the number of events before and after all cuts are propagated into the calculation of the signal efficiency, as will be described in section 5.7.2.

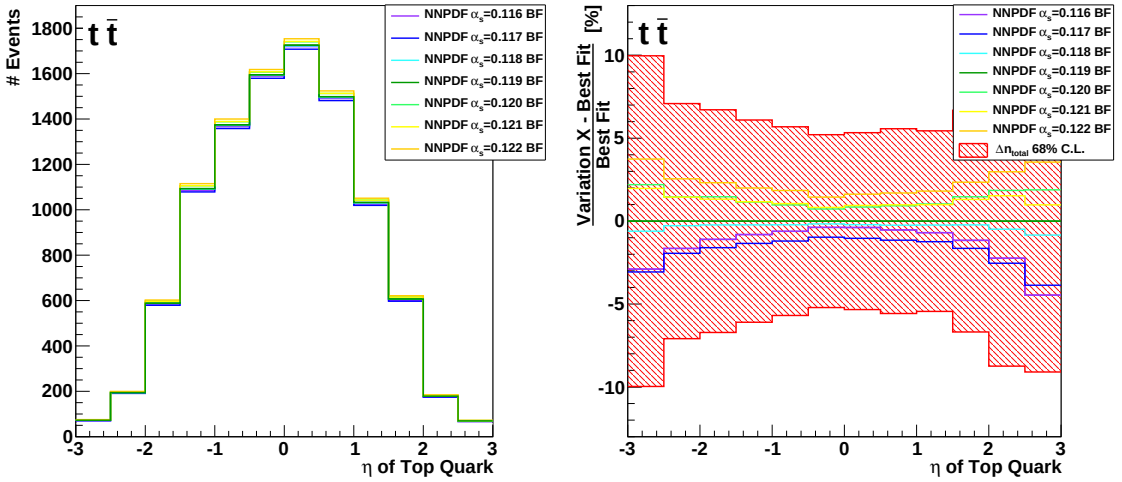

(a) Variation of the fit parameters and α_s

(b) Variation of the fit parameters and α_s scaled to best fit

Figure 5.27: η distribution of top quark for estimation of PDF and α_s uncertainties with sets from NNPDF.

	CTEQ6.6			MSTW2008			NNPDF
[%]	Δn^{PDF}	Δn^{α_s}	combined	Δn^{PDF}	Δn^{α_s}	combined	combined
$W \to \mu\nu$	+ (2.1) - (2.1)	+ (0.1) - (-0.6)	+ (2.1) - (2.2)	+ (2.2) - (1.7)	+ (0.5) - (0.5)	+ (2.3) - (1.8)	**± 2.4**
$W \to \tau\nu$	+ (2.0) - (1.9)	+ (0.2) - (-0.7)	+ (2.0) - (2.0)	+ (2.3) - (1.6)	+ (0.6) - (0.6)	**+ (2.3)** - (1.7)	**± 2.2**
$t\bar{t}$	+ (8.9) - (7.4)	+ (2.3) - (-0.9)	**+ (9.2)** **- (7.4)**	+ (4.3) - (4.7)	+ (0.4) - (0.4)	+ (4.4) - (4.7)	± 5.8
$LM0$	+ (8.4) - (6.8)	+ (2.0) - (-0.6)	**+ (8.6)** **- (6.8)**	+ (3.9) - (4.0)	+ (0.1) - (0.1)	+ (3.9) - (4.0)	± 4.9
$LM1$	+ (11.1) - (8.5)	+ (2.5) - (-0.8)	**+ (11.4)** **- (8.6)**	+ (4.7) - (4.3)	+ (0.2) - (0.2)	+ (4.7) - (4.3)	± 5.9

Table 5.4: Results of the PDF and α_s uncertainty estimation for all MC samples present after all analysis cuts have been made, where the listed values are the relative uncertainties on the number of events. The largest value for each MC sample is given in red.

5.6.2 Jet Energy Scale Uncertainties

As described in section 4.4.6 the energy of a jet is a function of its transverse momentum p_T and pseudorapidity η. Corrections were applied to make the detector response flat in both variables. Systematic uncertainties have been estimated by the CMS Jet Energy Correction Subgroup [61], which are normalization and shape changing. To estimate their influence on the final event selection, the jet momentum and energy is varied up and down by these factors. This procedure is also propagated to the missing transverse energy.

For the final JES uncertainty on the number of events after all cuts, the maximum deviation for each background process is chosen. In total a rather large influence on the background of about 15% is found. This is the most prominent systematic uncertainty for the background yield. Once

again the results for LM0 and LM1 are used to estimate the uncertainty on the signal and lead to a value of about 5%. The JES uncertainty is one of the most important uncertainties for the signal. Only the combined PDF and α_s uncertainty is larger by approximately a factor of two.

5.6.3 Jet Resolution Uncertainties

The resolution of jets was estimated to about 10% using the Asymmetry method on events with at least two jets. Furthermore, uncertainties on this method were determined from Monte Carlo simulations. For particle flow jets an uncertainty of 40% on the result of the Asymmetry method is assumed as a conservative estimate [100].

To include this value of 4% in the analysis, a Gaussian smearing is performed on the jet momenta and propagated into the missing transverse energy, where the standard deviation of the Gaussian distribution is set to 0.04. This results in a deviation of the background yield of only about 1.6%. The influence on the signal samples is even smaller at about 0.2% and practically negligible.

5.6.4 Lepton Resolution and Scale Uncertainties

The presented analysis uses muons and a veto on electrons to define its search channel. Both particles' momentum scale can only be measured within a given accuracy. Furthermore, an estimate of the uncertainty of the particles' resolution must be accounted for.

To estimate the uncertainties on the resolution and momentum scale of muons, events from $Z \to \mu\mu$ decays are used. They give a good approximation for muons with a transverse momentum between 20 and 100 GeV. The Z mass is reconstructed and two methods are applied to fit its shape. Comparing the peak values and widths of both fits gives an estimate of the uncertainty on the muon scale and resolution [49].

The relative muon resolution uncertainty is estimated to about 0.5%. This value is used as the standard deviation of a Gaussian used to smear the transverse momentum of the muon and also propagated into the missing transverse energy. Only a small influence on the number of events passing the selection is seen. It is found to be under one per mil for the background and about 1% for the signal estimates.

Comparing the peak values of both Z mass fits, a deviation of about 0.1% on m_Z is found. It is assumed that this shifts the momentum of positive and negative muons by about $0.1\% \cdot p_T/m_Z$. Propagating the shift into the analysis is done by varying the muon's momentum and energy values up and down. Once more only a small influence can be observed. The background and signal yields change by about 0.3% and 0.2%, respectively.

To account for the electron momentum scale uncertainty the electron's energy and momentum are varied by 1.3% for electrons in the barrel region ($|\eta| < 1.5$) and 4.1% in the endcaps [101]. At 0.6% the effect of this variation is small for the background yield and even smaller at 0.1% for the signal. The effect of the electron resolution uncertainty is assumed to be negligible.

5.6.5 $\not{E}_T$ Resolution

The impact of systematic uncertainties on the clustered part of the missing transverse energy are taken into account by the methods described above. To gain an estimate of how mis-measurements of the unclustered energy propagate into the final number of events, the x and y components of $\not{E}_T$ are smeared by a Gaussian distribution. The standard deviation of the Gaussian is assumed to 10% of the nominal value as suggested by [102].

For the background yield a small effect of about 1% is calculated. The signal shows an influence only 0.5% on the number of events after all cuts.

5.6.6 Cross Section Uncertainties

All cross sections of Standard Model processes listed in table 5.1 have uncertainties that originate from the limited knowledge of the factorization and renormalization scale. To account for this, both scales are varied up and down by a factor of 2, assuming both scales are fully correlated. The cross section uncertainties are included in the table and have been taken from [73].

Being the main background in the final event selection, the 6% uncertainty on the $t\bar{t}$ cross section has the largest influence. In summary the cross section uncertainty on the number of all background events after all cuts is evaluated to 5.0%. The leading order Monte Carlo estimates for LM0 and LM1 are not used for the final analysis. The influence of the factorization and renormalization scale will be estimated separately and explained in section 5.7.

5.6.7 Luminosity Uncertainty

Using the complete dataset taken in 2010 corresponds to an integrated luminosity of $36\,\mathrm{pb}^{-1}$, which was determined by Van der Meer scans of the two beams. An uncertainty of 4% has been estimated for this value [103]. All simulated samples are normalized with the luminosity, so the uncertainty must be propagated to all of them.

5.6.8 Summary of all Systematics

The following table 5.5 summarizes the effects of the different systematics taken into account on the total background and signal yield. As mentioned above the benchmark points LM0 and LM1 are used to estimate the uncertainties on the number of signal events.

The uncertainty on the jet energy scale corrections has by far the largest impact on the number of background events. For the signal yield the effects evaluated from the PDF reweighting are even more prominent than those of the JES corrections.

[%]	$\sum$ BGs	LM Points
PDF + α_s	6.5	10
Jet Energy Scale	15	4.9
Jet Resolution	1.6	0.18
μ Resolution	0.011	1.0
μ Scale	0.30	0.24
e Scale	0.60	0.086
$\not{E}_\mathrm{T}$ Scale	1.1	0.48
Cross sections	5.0	—

Table 5.5: Summary of results of the systematics estimation for all considered uncertainties. The listed values are the relative uncertainties on the number of events after all analysis cuts.

5.7 Exclusion Limits

Since no significant excess in data was seen over the Standard Model prediction limits are set on cross sections of SUSY models in the m_0-$m_{1/2}$ plane. This extends the search from the benchmark points to a larger region in the five dimensional mSUGRA parameter space.

5.7.1 Bayesian Statistics

Using the RooStats Bayesian upper limit calculator [104][105], observed and expected limits are computed for the one bin counting experiment presented in this thesis. In Bayesian statistics one assumes a subjective degree of belief for the value of a parameter, in contrast to the frequentist approach where probabilities are represented by the outcome of repeatable measurements [106]. Taking n_{obs} to be the number of events observed in background and signal, one finds the likelihood function to follow a Poisson distribution

$$L(n_{obs}|\mu) = \frac{\mu^{n_{obs}}}{n_{obs}!} \cdot e^{-\mu} \tag{5.11}$$

with the mean μ given by

$$\mu = \sigma_{sig} \cdot \mathcal{L} \cdot \epsilon + n_{bg} \tag{5.12}$$

where σ_{sig} is the signal cross section, $\mathcal{L}$ is the integrated luminosity, ϵ refers to the product of signal efficiency and acceptance and n_{bg} is the expected background yield of the final selection. With the signal cross section σ_{sig} being the parameter of interest, a limit on this quantity can be calculated by integrating over the posterior distribution $P(\sigma_s|n_{obs})$ determined from Bayes' theorem:

$$P(\sigma_{sig}|n_{obs}) = \int_0^{\sigma_{up}} L(n_{obs}|\mu) \cdot \pi(\sigma_{sig}) \cdot \pi(\nu) d\nu \tag{5.13}$$

A uniform prior function $\pi(\sigma_{sig})$ for the parameter of interest is chosen along with lognormal priors $\pi(\nu)$ for the nuisance parameters ν modeling systematic uncertainties of the signal cross section. Setting the value of expression 5.13 to 0.95 and determining the necessary upper boundary σ_{up} corresponds to a 95% C.L. upper limit [107].

An observed limit results from relating the number of observed data events to the background and signal estimate. For the expected limit background-only pseudo experiments are performed repeatedly, each used to evaluate an upper limit by comparing the calculated number of events to the signal estimate. The median expected limit, as well as the 1σ and 2σ bands can be determined from this ensemble of limits.

5.7.2 Limit Calculation and Results

The Monte Carlo mSUGRA estimates used for this study were produced with Fast Simulation [108] by the CMS SUSY group [109]. To obtain an NLO result, a k-factor is applied. It accounts for higher order corrections to the signal processes that were not considered during the LO production. A separate k-factor is applied to each process for every value of m_0-$m_{1/2}$. The calculated upper limit on the cross section of a given point is compared to NLO cross section estimations given by [109] and evaluated with PROSPINO2 [110][111].

The limit estimation relies on information about the number of observed background events as well as the efficiency (times acceptance) $\epsilon = \frac{n}{N}$ of the signal. Statistic and systematic uncertainties are assigned to both values. A Poisson standard deviation is used for statistical fluctuations of the background, whereas a binomial estimate is chosen for the efficiency. An improved description of the statistical uncertainty on the efficiency could be achieved with a Clopper-Pearson interval

[112]. This thesis assumes the binomial estimate to perform sufficiently, since the values for n and N do not resemble extreme cases that result in failure e.g. $n = 0$ [113]. The systematics discussed above are included in the number of events before and after cuts and propagated into the efficiency $\epsilon = \frac{n}{N}$ via:

$$\Delta\epsilon^{sys} = \epsilon \cdot \sqrt{\left(\frac{\sigma_n^{sys}}{n}\right)^2 + \left(\frac{\sigma_N^{sys}}{N}\right)^2}. \tag{5.14}$$

Figure 5.28 shows the final results of the limit calculation for three different values of $\tan\beta$: 3, 10 and 50. The plots were made using a plotting tool from the CMS SUSY group [114]. In all three plots the trilinear coupling is set to $A_0 = 0$ and the unified Higgsino mass term μ is assumed to take on positive values.

In all of the following figures depicting the exclusion limits the solid red line shows the observed limit at 95% C.L. using the NLO cross section estimates as described above. The expected limit is depicted by a black dash-dotted line and its 1σ band is given by blue dashed lines. One can generally see that the expected limit exceeds the observed, since more events were seen in data than predicted by the Standard Model Monte Carlo estimate. The deviation is not significant, which is shown by the fact that the observed limit is within or close to the lower 1σ quantile of the expected limit.

The value of $\tan\beta$ determines the amount of third generation quarks and leptons in the parameter space [115]. The choice of $\tan\beta$=50 shown in figure 5.28(c) represents the highest value that can be chosen within the MSSM before encountering theoretical or experimental constraints. It is motivated by the ratio of the top and bottom quark masses, since these are proportional to the Higgs vacuum expectation values $\langle H_u^0 \rangle$ and $\langle H_d^0 \rangle$ at the GUT scale. The fraction of taus is larger than that of muons and electrons for high values of $\tan\beta$, whereas low values of $\tan\beta$ favor the first and second generation leptons. Thus one would expect the muon-based analysis considered in this thesis to be less sensitive at $\tan\beta = 50$ than at low values of $\tan\beta$. The branching ratio $\tau \to \mu$ is only about 17.4% [2], so not many events with muons will be present in the parameter space. This trend is hard to be seen when comparing figures 5.28(a), 5.28(b) and 5.28(c).

The limit is calculated individually for each bin of m_0 and $m_{1/2}$, with a bin width of 10 GeV in both directions. One would expect that if a specific point is excluded within the expected limit, that all points at smaller values m_0 and $m_{1/2}$ should also be excluded. Due to low efficiencies this does not hold to be true for all regions of the parameter space. Figure 5.29 shows the efficiency times acceptance, ϵ, of the complete set of cuts for a value of $\tan\beta = 3$. The color code accounts for values of ϵ ranging from zero in dark blue to about 0.07 in red. White spaces in the figure represent bins where the calculations were not performed.

In the region of low $m_{1/2}$ the efficiency falls below values of 0.01. Calculating a limit in these bins does not result in an exclusion. The expected number of signal events is so small, that it cannot compete with the statistical and systematic uncertainties on the background. To understand why this behavior is found especially for low regions of $m_{1/2}$, the cuts applied during the analysis are reconsidered. Three bins with different values of m_0 and $m_{1/2}$ covering the low, medium and high efficiency range are selected for a detailed investigation of the cuts. The color code corresponds to the one from figure 5.29. Figure 5.30 shows the analysis cuts in succession for the three selected parameter space points. The respective values for m_0, $m_{1/2}$ and the efficiency are given in the legend. Figure 5.30(a) depicts the number of events passing each cut, whereas the relative affect of each cut can be seen in figure 5.30(b).

One can see that no single cut has a particularly strong influence on the three regions, but that the combination of several cuts leads to the different efficiencies. Recalling the approximate relations 3.15 from chapter 3, one can understand that sfermion masses are small at low values of m_0 and $m_{1/2}$, so muons from the decay would not be very energetic. Thus the cut on the p_T of the muons applied by the single muon trigger and by the loose muon requirement will especially effect this region. The gaugino masses depend on the value of $m_{1/2}$, see equation 3.14, so jets produced from gaugino decays will show higher energies at larger values. Furthermore, the missing transverse

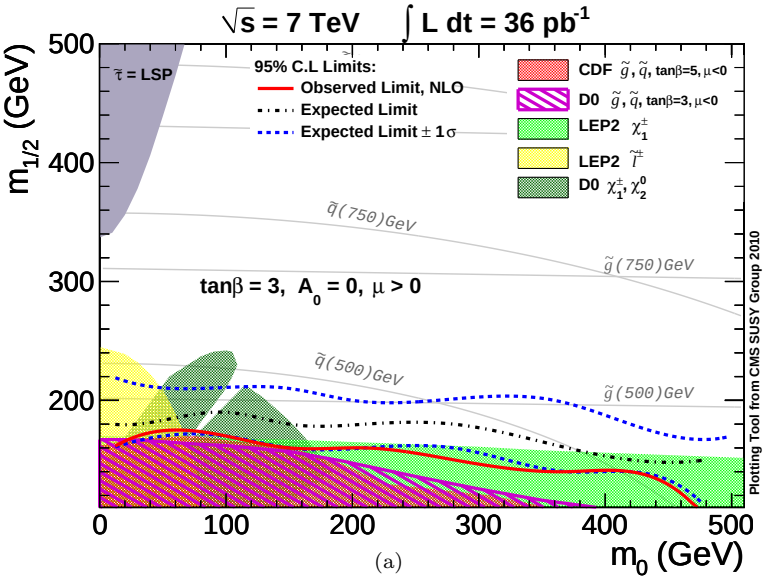

(a)

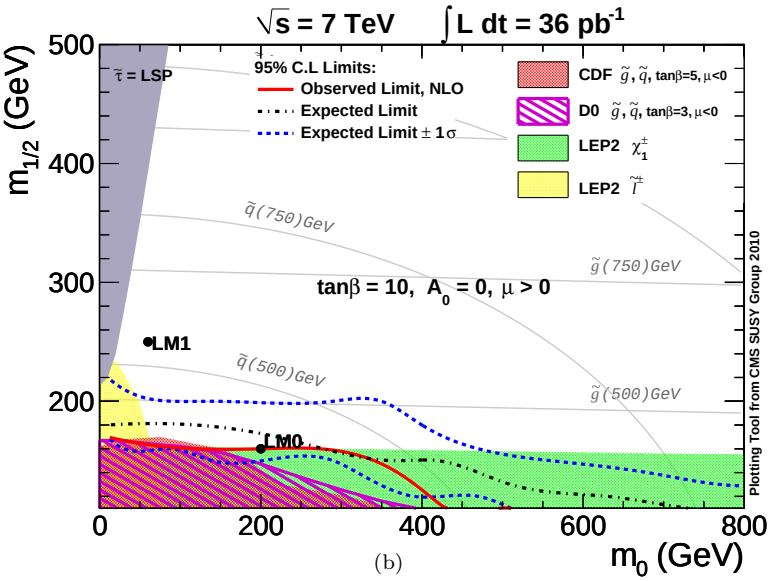

(b)

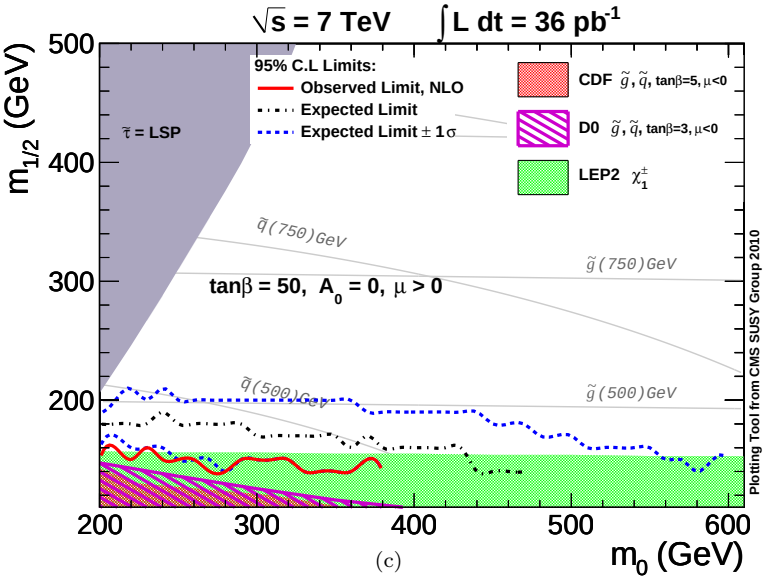

(c)

Figure 5.28: Upper exclusion limits set in the m_0-$m_{1/2}$ plane with A_0=0, μ >0 and tan β=3, 10 or 50. The observed limit at NLO is shown by a solid red line. The expected limit is depicted by a black dash-dotted line and its 1σ quantiles by blue dashed lines

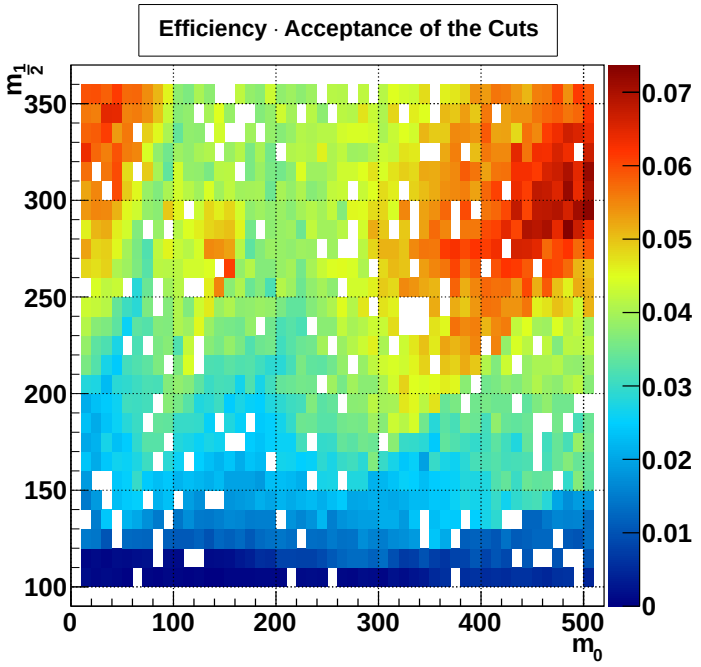

Figure 5.29: Scan of the mSUGRA plane with $\tan\beta$=3, A_0=0, μ >0. The efficiency times acceptance of the analysis cuts is shown, where blue bins correspond to a low efficiency and red bins represent higher values.

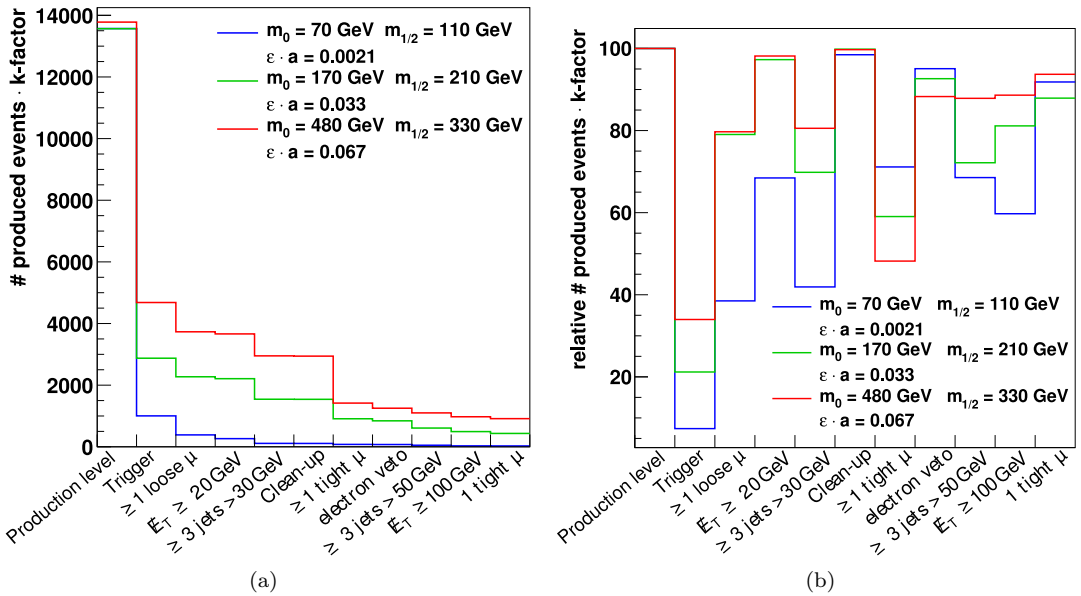

(a) (b)

Figure 5.30: Event count of the individual cuts for three points in the m_0-$m_{1/2}$-plane with $\tan\beta$=3, A_0=0, μ >0. Figure a) gives the total number of events and b) relates each cut to the one before.

energy originating from the LSP takes on m_0-$m_{1/2}$ dependent values, resulting in varying cut efficiencies.

The points that show a low efficiency in this analysis have already been excluded by previous experiments at LEP and at the Tevatron, so they will not be taken further into account here.

The lines shown in figure 5.28 represent the upper boundary between excluded and not excluded points.

Exclusions from previous experiments are shown by surfaces of various colors in all of the following plots. A synopsis of these limits can be found in [12].

Firstly, exclusions were set in e^+e^- annihilation at the LEP collider. The green band parallel to the m_0 axis represents the combined exclusion of the ALEPH, DELPHI, L3 and OPAL collaborations. It was estimated by setting a lower limit on mass of the lightest chargino resulting at $m_{\widetilde{\chi}_1^\pm} > 91.9\,\text{GeV}$ [116]. Furthermore lower limits could also be set on slepton masses resulting in a combined value of approximately 100 GeV for smuons, selectrons and staus [117]. This is accounted for by the yellow region in the following figures. Combined results of all four experiments can be found on [118] and their interpretation in the mSUGRA framework is documented by [119].

Shown by a purple striped area in all figures is an exclusion from a search for squarks and gluinos conducted by the DØ experiment at Tevatron with $\sqrt{s}$=1.96 GeV [120]. The search channel covered events with jets and missing transverse energy. Lower limits could be set on the sparticle masses: $m_{\tilde{q}} > 379\,\text{GeV}$ and $m_{\tilde{g}} > 308\,\text{GeV}$. The CDF collaboration reported similar results [121], which are shown by the red area in all figures.

Depicted in dark green in figure 5.28(a) where $\tan\beta = 3$ is a further exclusion from the DØ experiment based on an integrated luminosity of $2.3\,\text{fb}^{-1}$. The search was performed for the trilepton final state in associated production of charginos and neutralinos: $p\bar{p} \to \widetilde{\chi}^\pm\widetilde{\chi}_2^0$ [122].

The observed limit calculated in this thesis does not exceed the exclusions from previous experiments, since the data only correspond to an integrated luminosity of $36\,\text{pb}^{-1}$ taken during 2010. The expected limits do exclude new regions in the mSUGRA plane i.e. higher values of $m_{1/2}$ than those from former experiments, showing the generally good sensitivity of the analysis. As already assumed at the end of section 5.4, LM0 can be excluded at 95% C.L., whereas LM1 cannot be ruled out.

During the production of the signal Monte Carlo estimate, the renormalization and factorization scales are set to fixed values. To incorporate the theoretical uncertainty on the scales, the NLO cross sections have been re-calculated with two different choices: both scales are set to twice and to half their nominal values. A direct comparison of the cross sections revealed an effect of about 10%. To quantify the impact of this variation on the observed limit it was re-evaluated for the two additional scenarios. The results for all three values of $\tan\beta$ can be seen in figure 5.31. The nominal observed limit is shown by a continuous red line, the variations are shown by orange and purple dashed lines. In general the variations do not exceed 10 GeV.

For comparison figure 5.32 shows the exclusion limit set by the CMS single lepton group (RA4) using the 2010 dataset [74]. The cuts applied in the RA4 analysis differ slightly from the ones presented in this thesis. The most noteworthy difference is that four jets with $p_T > 30\,\text{GeV}$ are required instead of three jets with $p_T > 50\,\text{GeV}$. The approximate factor of two found between the exclusion limit of figures 5.28(b) and 5.32, is due to the fact that the RA4 group combines single muon and single electron channels, thus roughly doubling their sensitivity. Furthermore the limits produced by this group exhibit the expected decrease in sensitivity for higher values of $\tan\beta$ as motivated above.

A similar result has also been reported by ATLAS with an integrated luminosity of $35\,\text{pb}^{-1}$ [123].

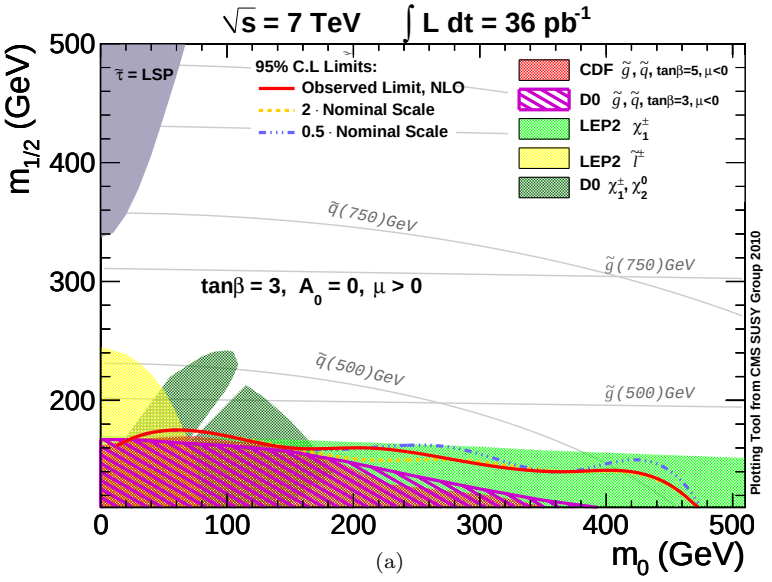

(a)

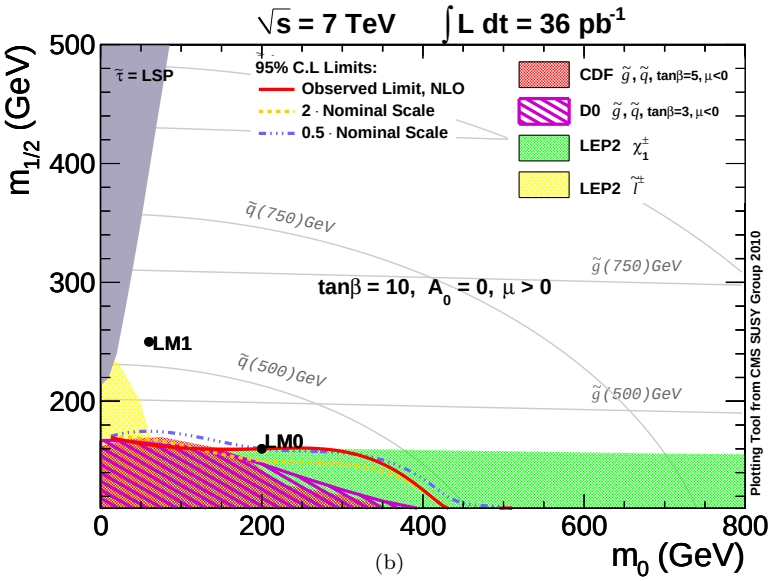

(b)

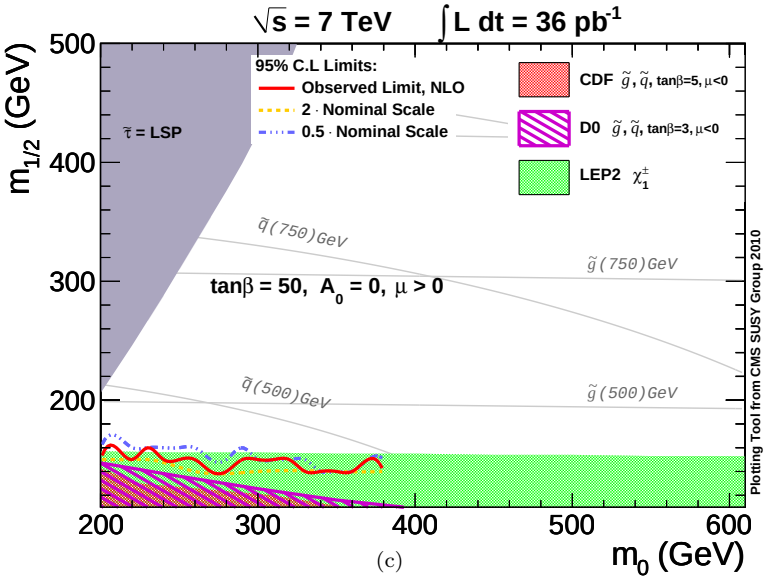

(c)

Figure 5.31: Upper exclusion limits set in the m_0-$m_{1/2}$ plane with A_0=0, μ >0 and $\tan\beta$=3, 10 or 50. The observed limit at NLO is shown by a solid red line. Variations of the factorization and renormalization scales are shown by orange and purple dashed or dash-dotted lines.

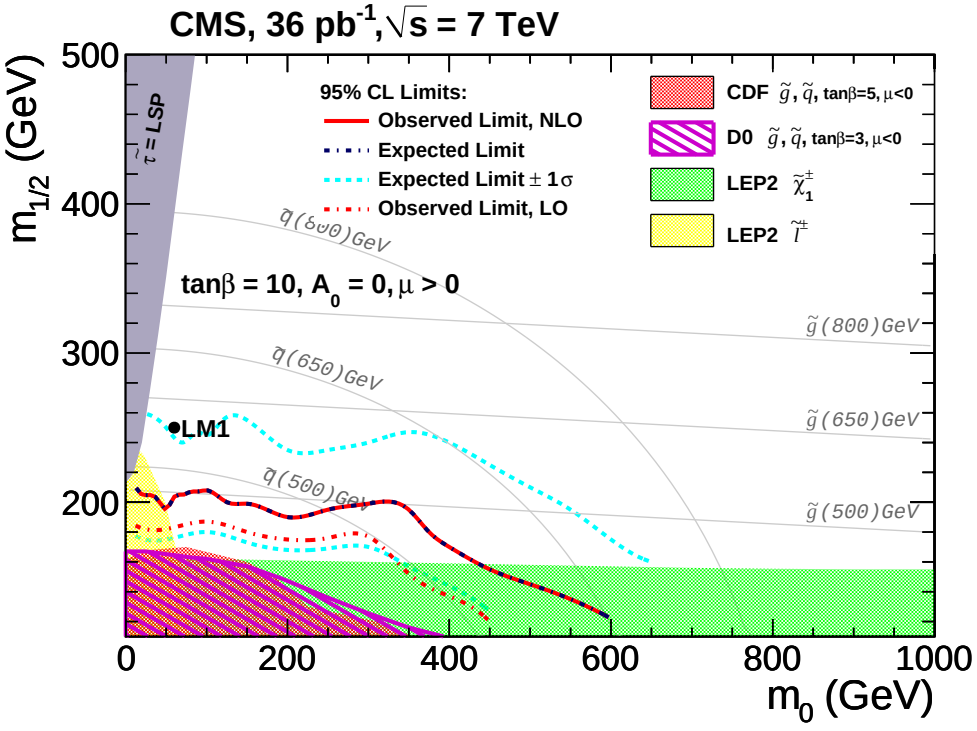

Figure 5.32: Exclusion limits from the CMS RA4 group [74] with $\tan\beta$=10, A_0=0, μ >0.

Chapter 6

Conclusion and Outlook

In this thesis a search for supersymmetry in the single muon channel was presented using the 2010 data from the CMS detector. To reduce large contributions from Standard Model backgrounds topologically motivated cuts were introduced. In the final event selection the data were in accordance with the Standard Model prediction:

$$\text{data: } 69 \text{ events} \qquad \text{vs.} \qquad \text{SM BG: } 54.3 \pm 1.1(\text{stat.}) \pm 16.3(\text{sys.}) \text{ events.}$$

A data-driven method was developed to gain a better understanding of the QCD multi-jet background. It is based on an extrapolation of events containing non-isolated muons into the signal region of events with isolated muons and $\not{E}_{\mathrm{T}} > 100\,\mathrm{GeV}$. Cross checks were carried out with QCD Monte Carlo estimates and the data itself. An overall good agreement was found between the data-driven estimate and the simulation. To make future analyses independent of Monte Carlo estimates a data-driven method should also be applied for the $t\bar{t}$ and W+jets backgrounds.

To estimate the effect of PDF and α_s variations on the simulated processes, the PDF4LHC recipe was incorporated in the analysis. Furthermore the impact of uncertainties from the jet energy scale and resolution, the lepton scale and resolution, the unclustered energy resolution, background process cross sections and the luminosity was evaluated.

Resulting from the absence of signal, exclusion limits were set in the mSUGRA parameter space. Expected limits, calculated from Monte Carlo estimates, were able to exclude new regions in the $m_0 - m_{1/2}$-plane including the benchmark point LM0. The analysis proves to have a good sensitivity. Due to a slight excess in the data the observed limits are less constraining. At an integrated luminosity of $36\,\mathrm{pb}^{-1}$ not enough data was collected to extend the excluded regions over those of previous collider experiments.

In 2011 the LHC has continued to run successfully, delivering over $3\,\mathrm{fb}^{-1}$ of data [124]. Analyses performed at CMS with the 2011 data set have not found any sign of supersymmetry yet. Significantly larger regions of the mSUGRA plane could be ruled out, as summarized in figure 6.1.

In light of these exclusions, proposals have been made to intensify the search for supersymmetry outside of the mSUGRA framework. Analyses of R-parity violating SUSY or simplified models are already being performed and could be important stepping stones to discovering supersymmetry. A summary of alternative models and new corresponding benchmark points has recently been given in [126].

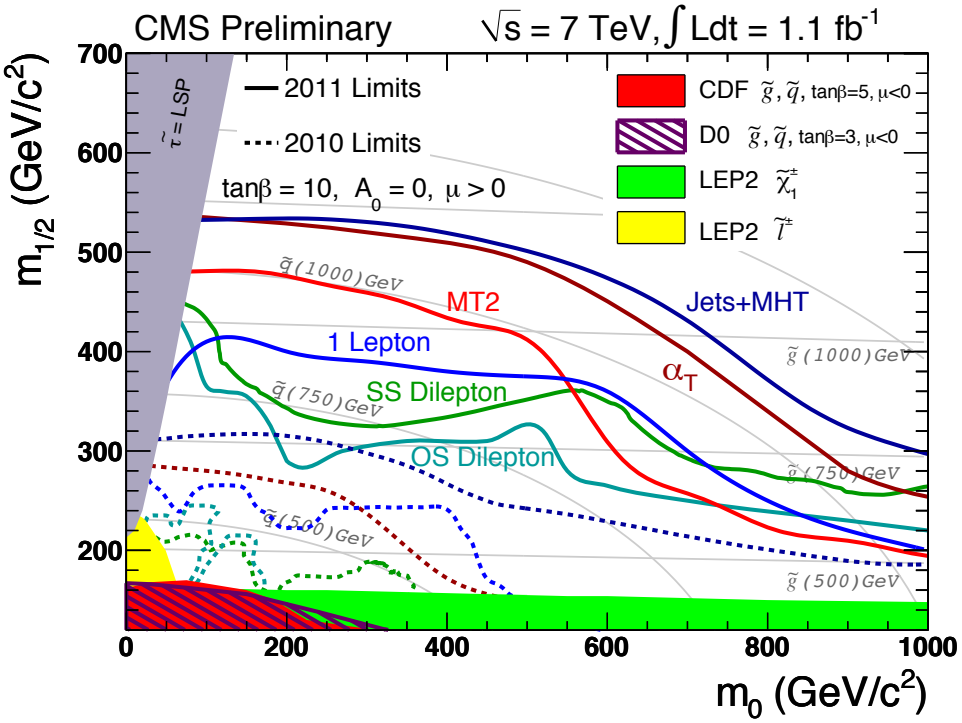

Figure 6.1: Summary of CMS supersymmetry searches from 2010 and 2011 [125].

Appendix A

Control Plots of the Object Selection Cuts

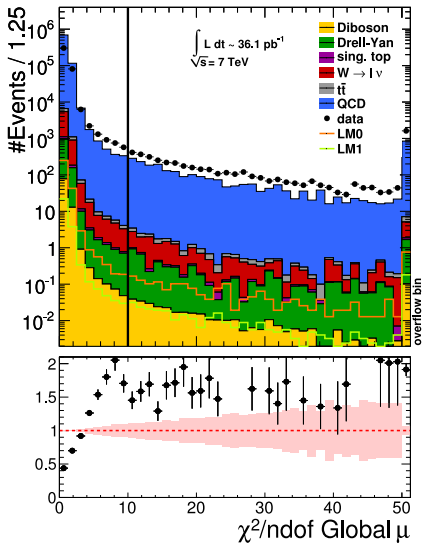

(a) Normalized χ^2 of the fit to the global muon (cut: $\chi^2/\text{ndof}_{global\ \mu} < 10$)

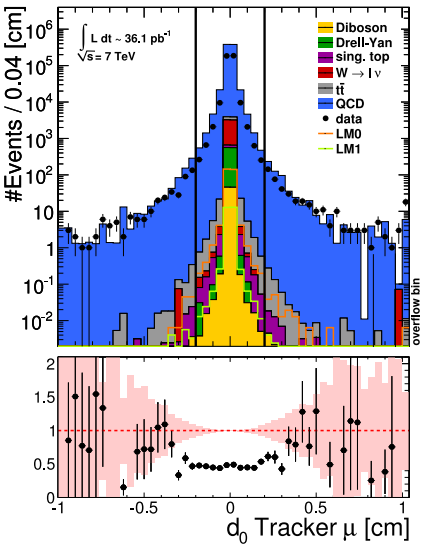

(b) Impact parameter of the muon's track in the tracker (cut: $|d_0|_{tracker\ \mu} < 0.2$ cm)

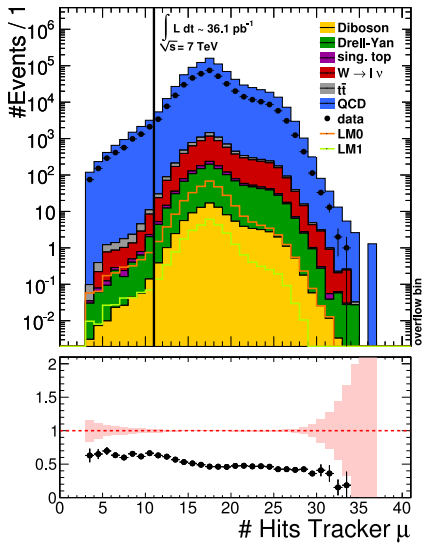

(c) Number of hits used to reconstruct the muon's track in the tracker (cut: # $\text{hits}_{tracker\ \mu} \geq 11$)

Figure A.1: Distributions of the quality criteria on the muon track. Each distribution is shown after all other cuts defining a loose muon have been applied. Not only the leading muon, but all muons of the event are included in the distributions.

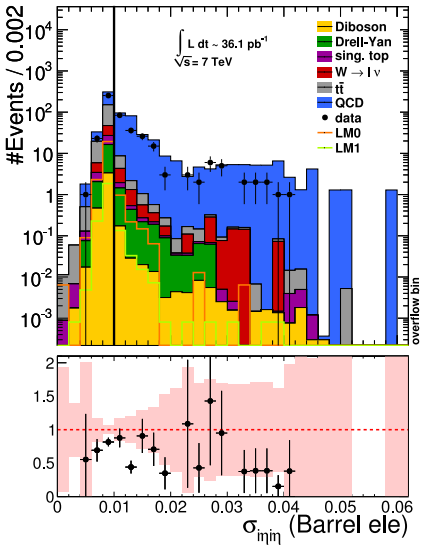

(a) Spread in η of energy in a 5x5 cluster (cut: $\sigma_{i\eta i\eta} < 0.01$)

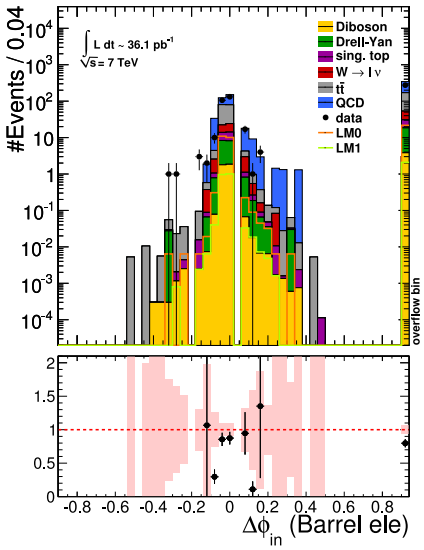

(b) $\Delta\phi$ between extrapolated track and supercluster (cut: $|\Delta\phi_{\rm in}| < 0.8$)

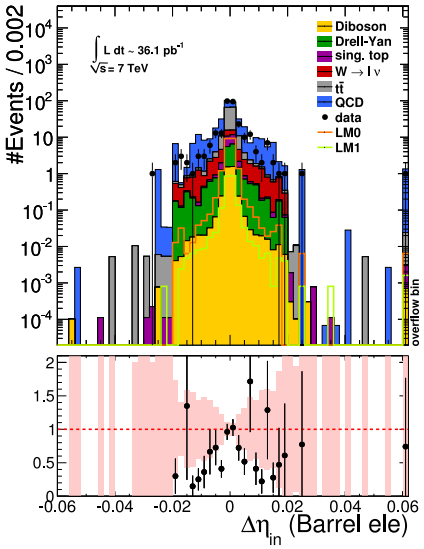

(c) $\Delta\eta$ between extrapolated track and supercluster (cut: $|\Delta\eta_{\rm in}| < 0.007$)

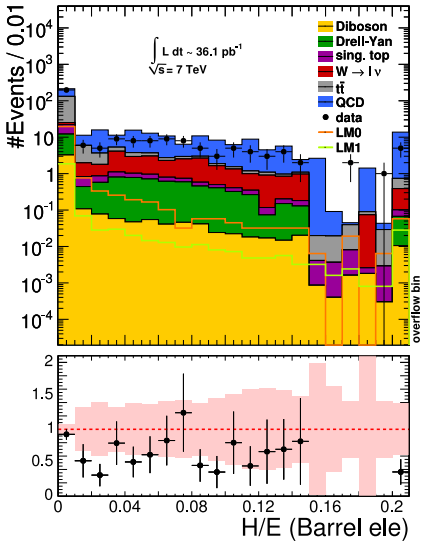

(d) Ratio of energy in HCal and ECal (cut: H/E < 0.15)

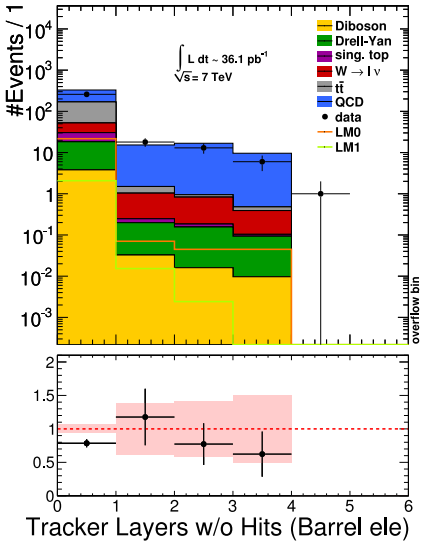

(e) Number of tracker layers without a hit may not be larger than one.

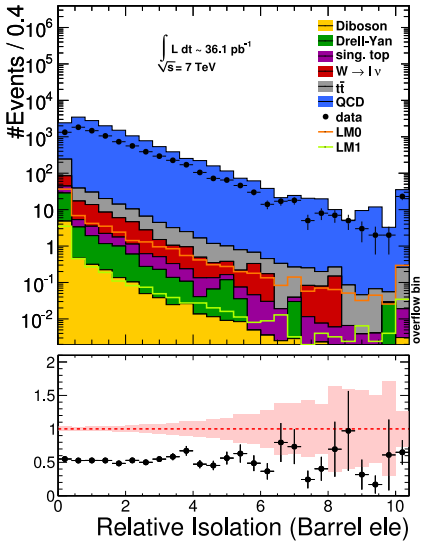

(f) Relative Isolation of the electron (cut: $RelIso^{ele} < 0.1$)

Figure A.2: Distributions of the quality criteria on electrons in the barrel region of the detector. Each distribution is shown after all other cuts defining a good electron have been applied. All electrons of the event are included in the distributions.

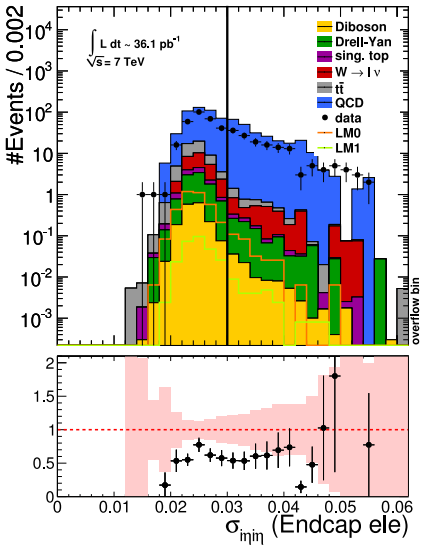

(a) Spread in η of energy in a 5x5 cluster (cut: $\sigma_{i\eta i\eta} < 0.03$)

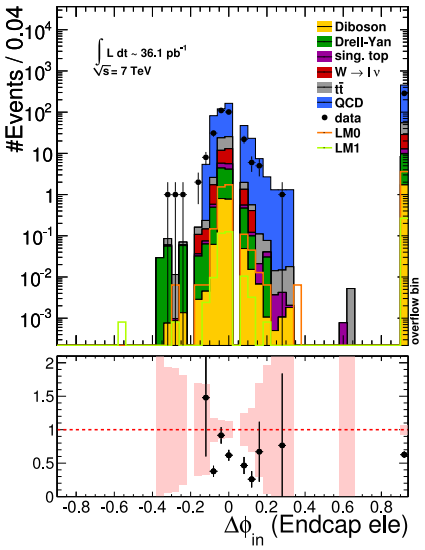

(b) $\Delta\phi$ between extrapolated track and supercluster (cut: $|\Delta\phi_{\rm in}| < 0.7$)

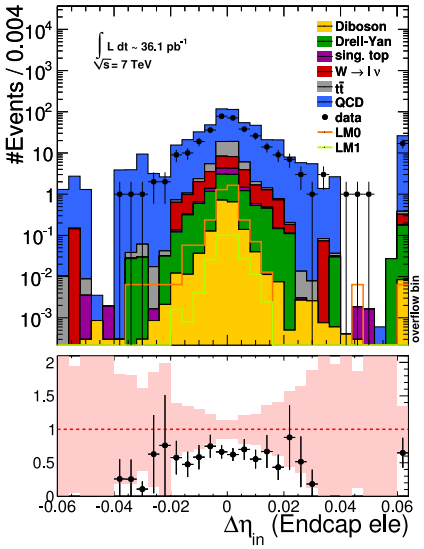

(c) $\Delta\eta$ between extrapolated track and supercluster (cut: $|\Delta\eta_{\rm in}| < 0.01$)

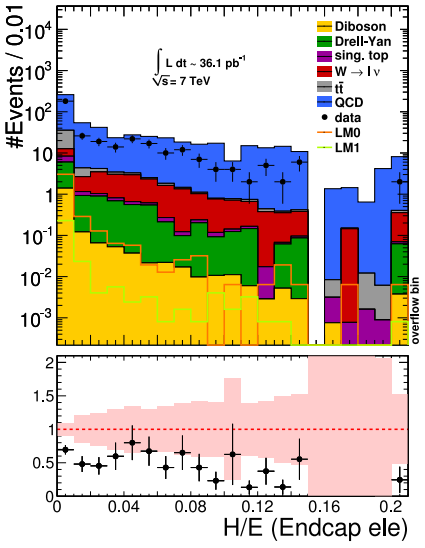

(d) Ratio of energy in HCal and ECal (cut: H/E < 0.07)

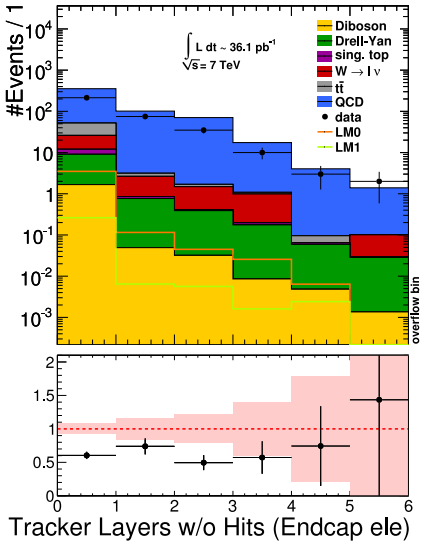

(e) Number of tracker layers without a hit may not be larger than one.

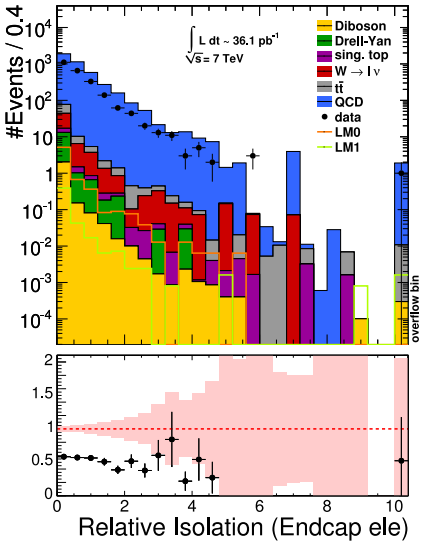

(f) Relative Isolation of the electron (cut: $RelIso^{ele} < 0.1$)

Figure A.3: Distributions of the quality criteria on electrons in the endcap regions of the detector. Each distribution is shown after all other cuts defining a good electron have been applied. All electrons of the event are included in the distributions.

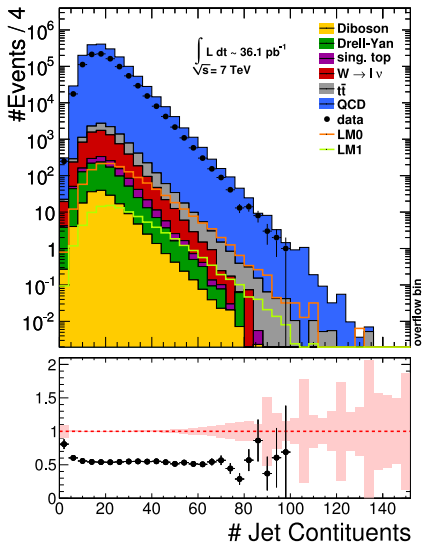

(a) Number of jet constituents must be greater than one

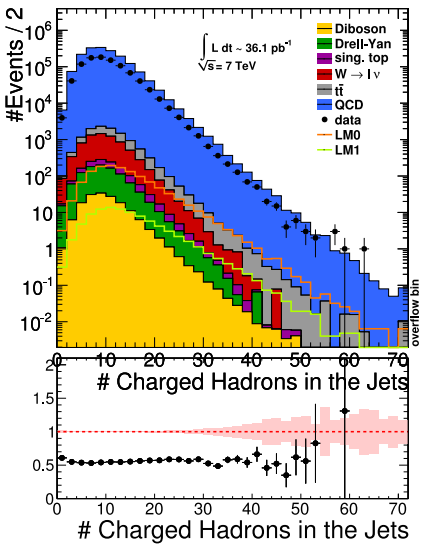

(b) Number of charged hadrons within the jet must be larger than zero

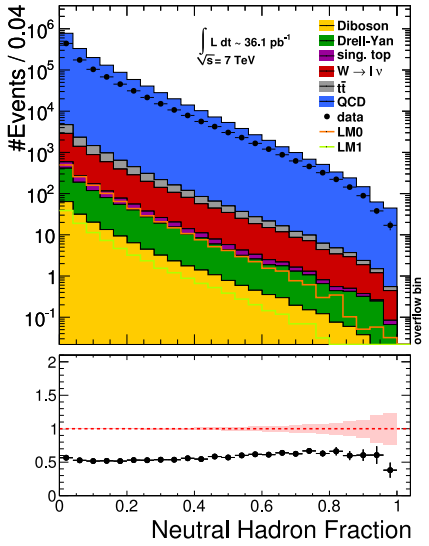

(c) Fraction of neutral hadrons within the jet (cut: $NHF < 0.99$)

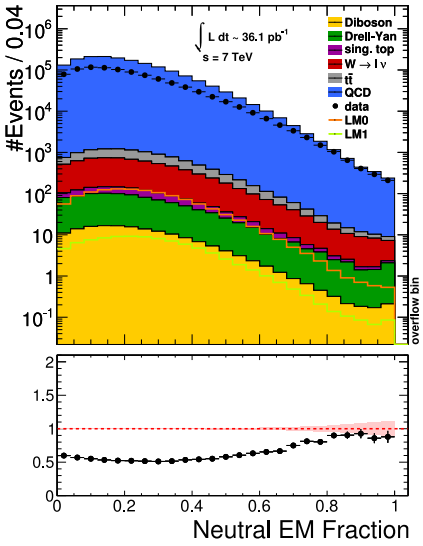

(d) Fraction of neutral electromagnetic particles within the jet (cut: $NEF < 0.99$)

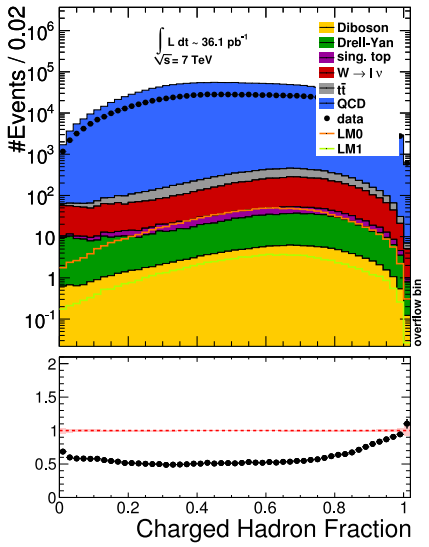

(e) Fraction of charged hadrons within the jet must be larger than zero

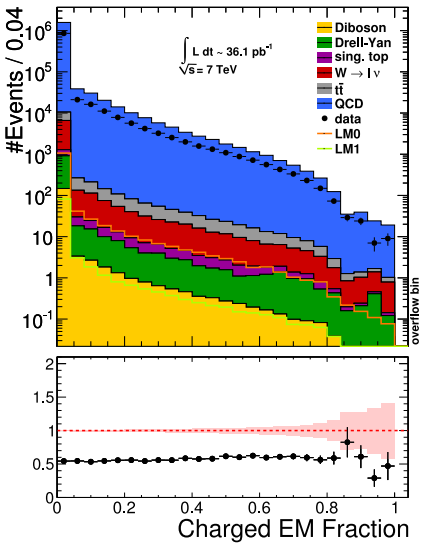

(f) Fraction of charged electromagnetic particles within the jet (cut: $CEF < 0.99$)

Figure A.4: Distributions of the quality criteria on jets. Each distribution is shown after all other cuts defining a good jet have been applied. Not only the leading jet, but all jets of the event are included in the distributions.

Appendix B

Supporting Plots for the Cut Based Analysis

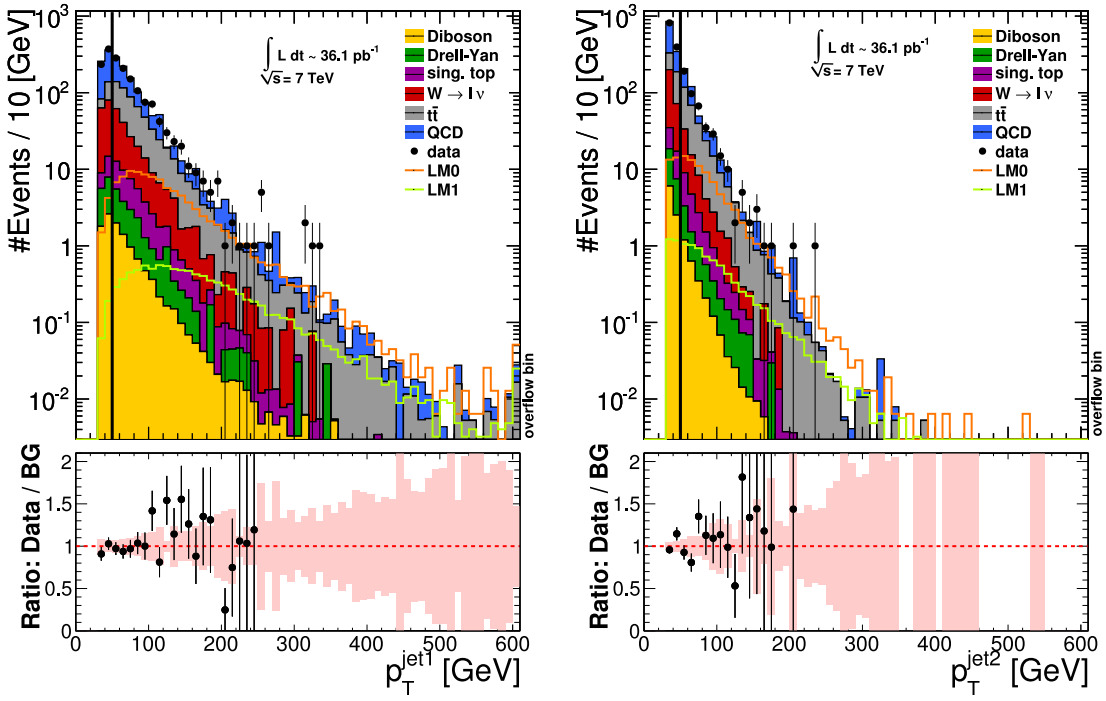

(a) (b)

Figure B.1: Transverse momentum distribution of the second and third hardest jet. Object selection, clean-up cuts, tight muon requirement and the electron veto have already been applied.

Appendix C

Supporting Plots for the Data-Driven QCD Background Estimation

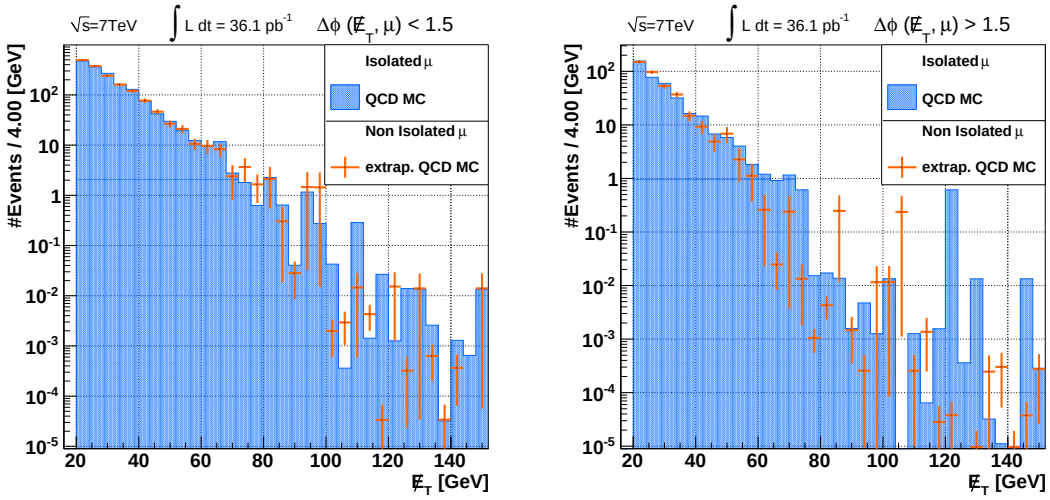

Figure C.1: Cross check of the QCD event extrapolation with MC simulations. Events containing tight muons are depicted in blue, those with non-isolated events are shown by orange markers. Both figures show the $\not{E}_{\mathrm{T}}$ distribution in both isolation regions, where an extrapolation scale has been applied to the non-isolated muon events. The plot on the left only includes events with $\Delta\phi(\not{E}_{\mathrm{T}},\mu)$<1.5 and the one on the right with $\Delta\phi(\not{E}_{\mathrm{T}},\mu)$>1.5. These four $\not{E}_{\mathrm{T}}$ distributions are used to conduct the closure test shown in figure 5.18.

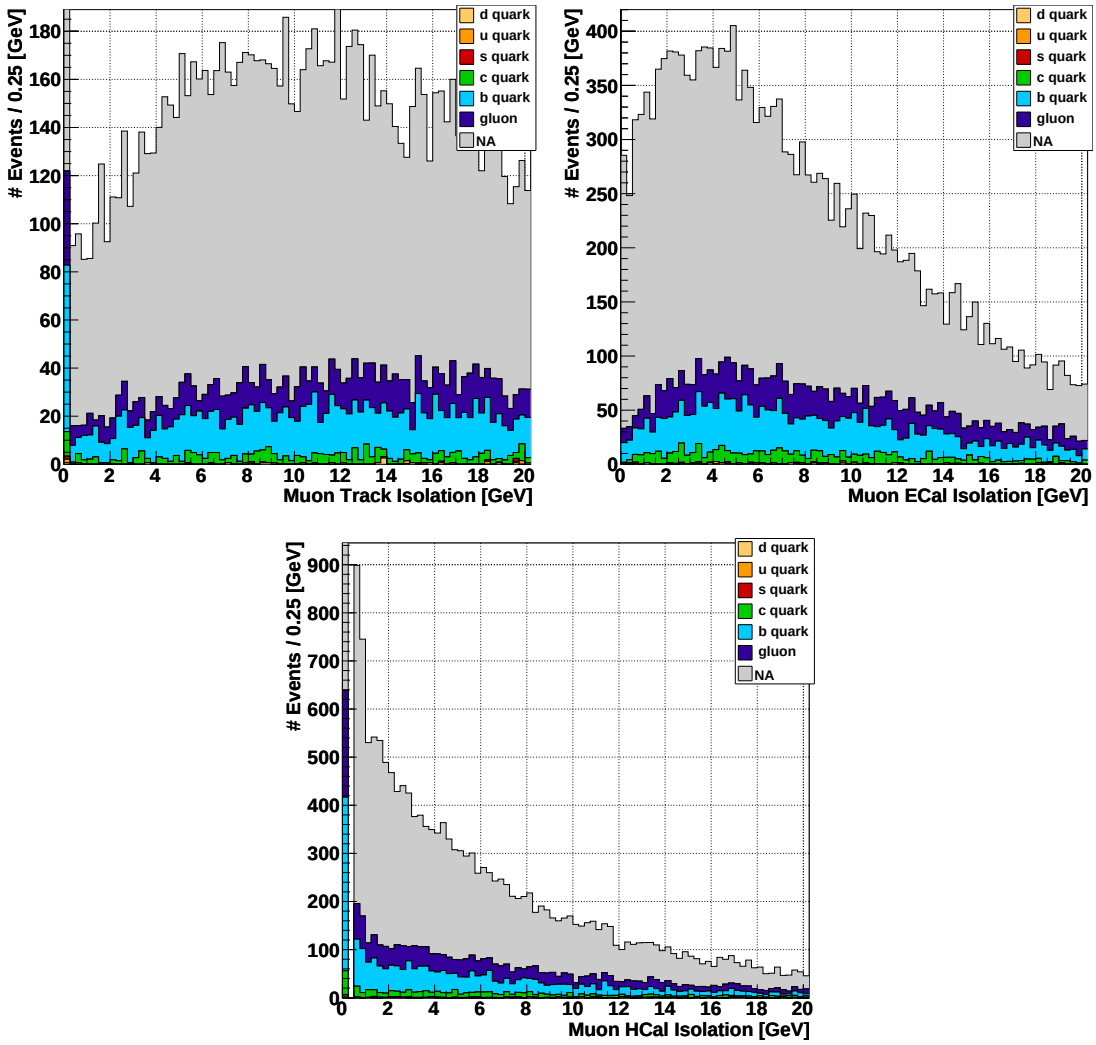

Figure C.2: Jet flavors binned in track, ECal and HCal isolation of the leading muon shown for the QCD MC estimate. The absolute number of gluons, u, d, s, c and b quark are given. Furthermore, the large amount of unmatched jets is given in gray.

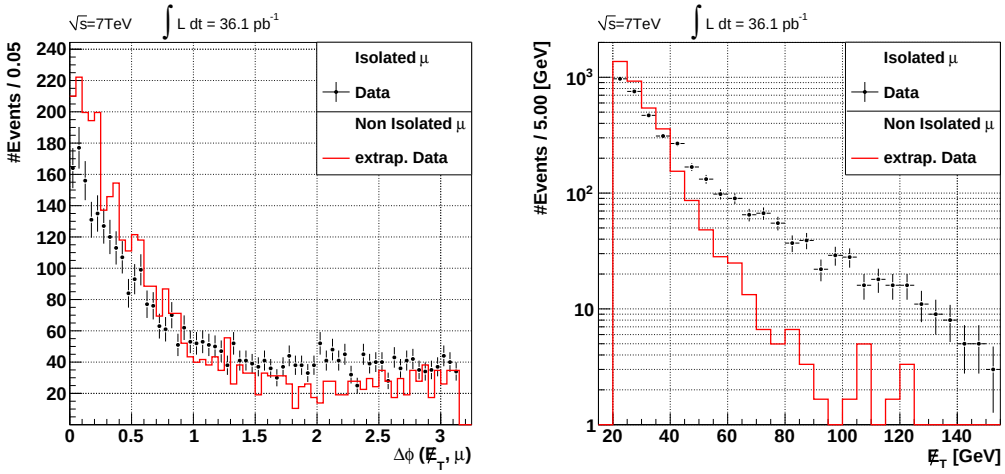

Figure C.3: Crosschecks of the QCD background estimation with the data. Events with tight muons are depicted by black markers, non-isolated muon events by a red line. The contributions from the electroweak backgrounds have not been subtracted, which leads to poor agreement in both the $\Delta\phi(\not\!\!E_{\mathrm{T}},\mu)$ and in the $\not\!\!E_{\mathrm{T}}$ distribution. Figure C.4 shows the comparison of isolated and non-isolated region for the MC estimates of the electroweak backgrounds.

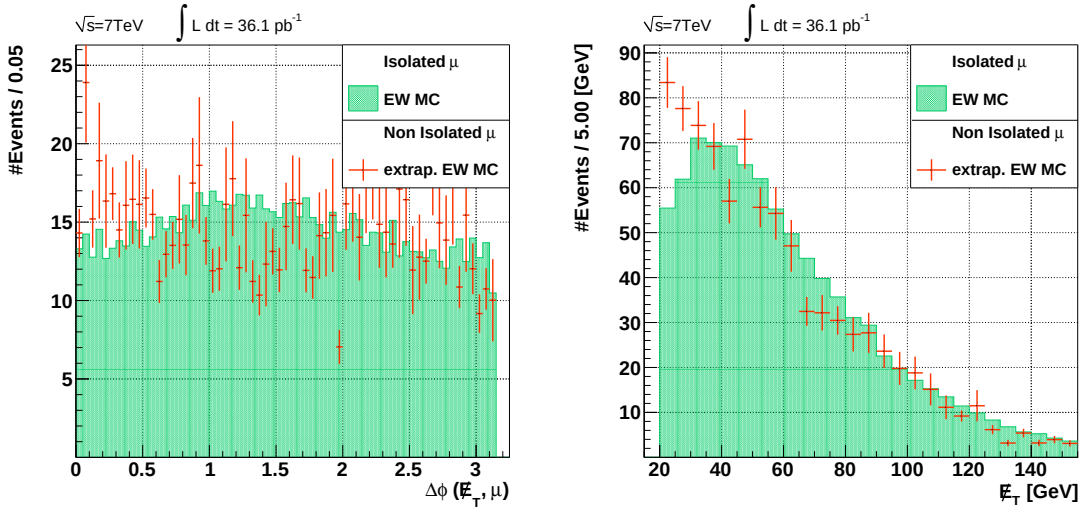

Figure C.4: Crosschecks of the data-driven method with electroweak MC estimates. The $t\bar{t}$, single top, Diboson and Drell-Yan backgrounds are summed up. Events containing isolated muons are depicted in green, non-isolated muon events are shown with orange markers.

Appendix D

Supporting Plots for the PDF and α_s Uncertainty Estimation

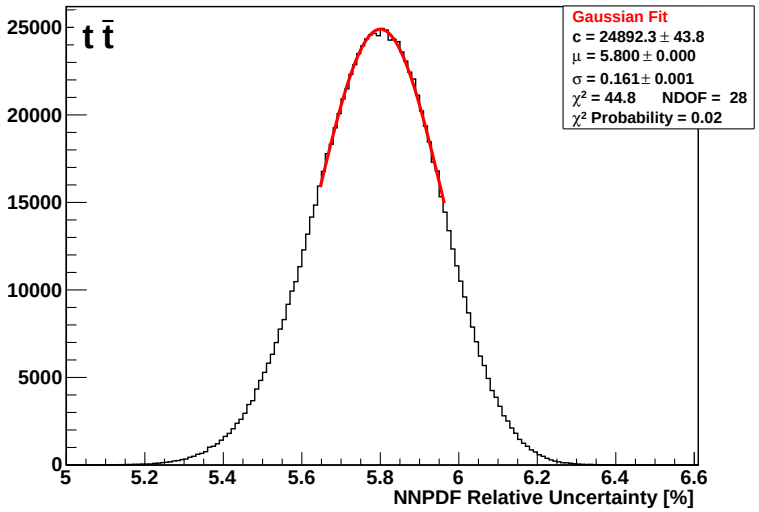

Figure D.1: Distribution of the uncertainty on the number of events after all cuts using a random selection of replicas from the NNPDF group. A Gaussian fit is performed to estimate the final uncertainty. For more detailed information see section 5.6.1.

The η distributions shown on the following pages for the $W \rightarrow l\nu$ do not exhibit the typical symmetrical shape one would expect. This is due to the fact that they only display events that have passed the complete set of analysis cuts, leading to low statistics. See table 5.3 for the number of events passing all cuts. Apparently the final selection of events is not a good representation of the underlying process.

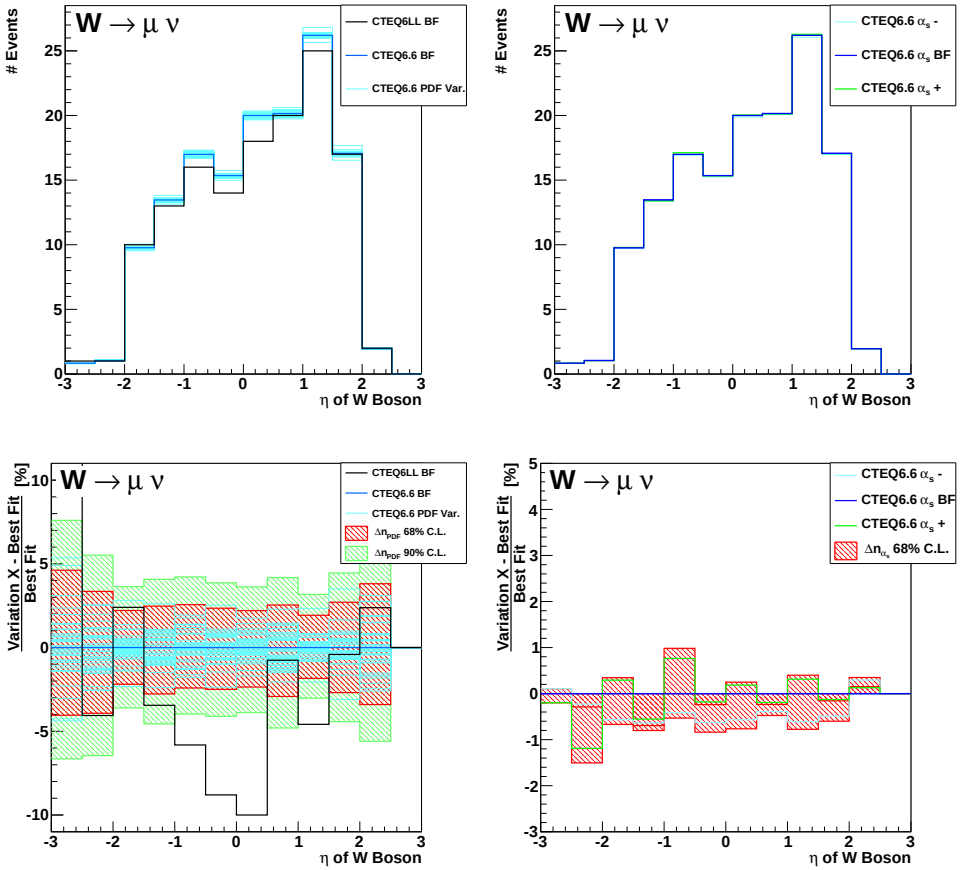

Figure D.2: η distribution of W boson for the estimation of PDF and α_s uncertainties with sets from CTEQ6.6. Legend entries labeled "BF" refer to the best fit member of the PDF set and "PDF Var." stands for members where fit parameters have been varied.

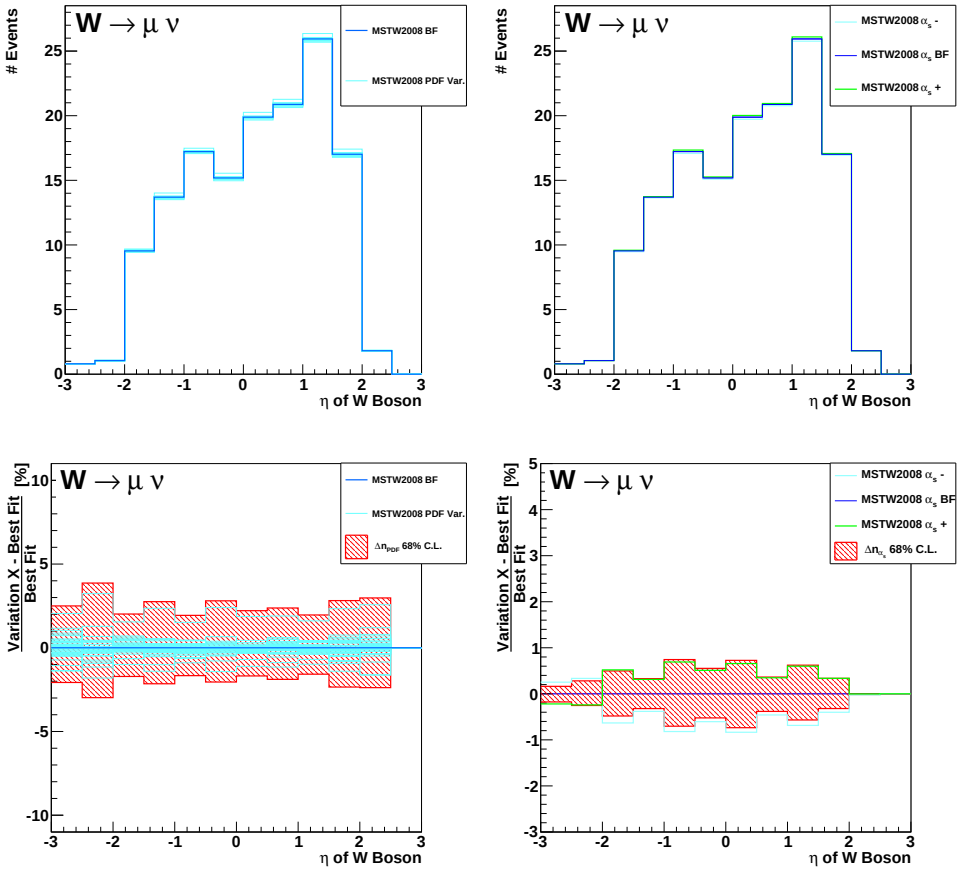

Figure D.3: η distribution of W boson for the estimation of PDF and α_s uncertainties with sets from MSTW2008. Legend entries labeled "BF" refer to the best fit member of the PDF set and "PDF Var." stands for members where fit parameters have been varied.

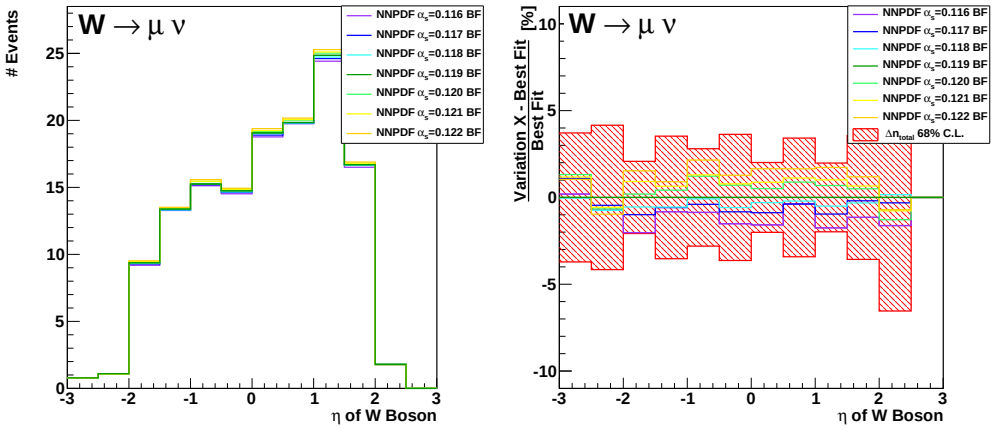

Figure D.4: η distribution of W boson for the estimation of combined PDF and α_s uncertainties with sets from NNPDF.

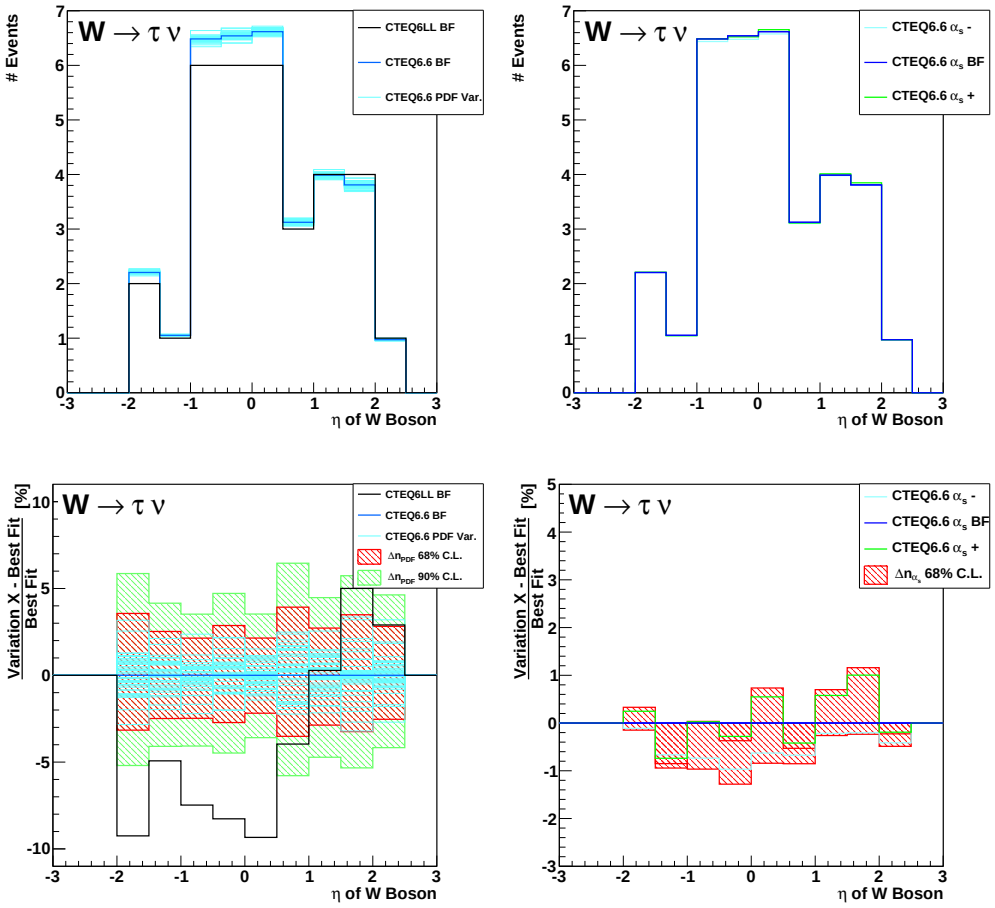

Figure D.5: η distribution of W boson for the estimation of PDF and α_s uncertainties with sets from CTEQ6.6. Legend entries labeled "BF" refer to the best fit member of the PDF set and "PDF Var." stands for members where fit parameters have been varied.

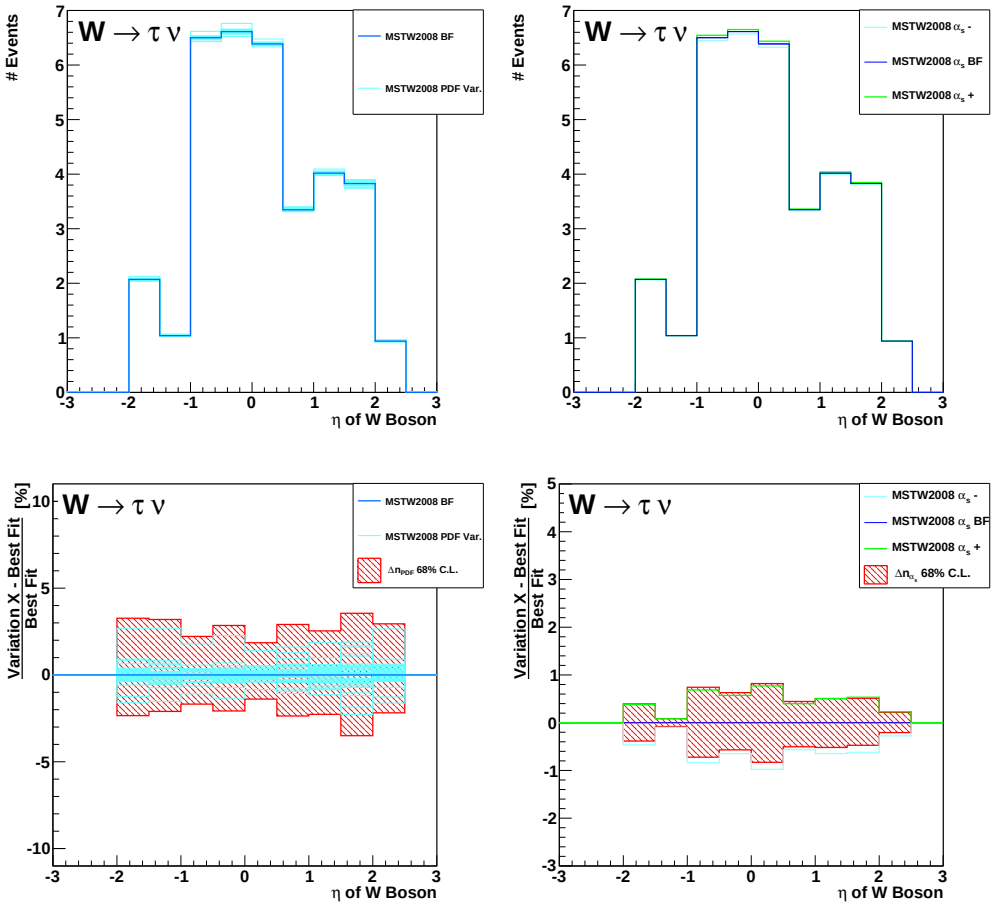

Figure D.6: η distribution of W boson for the estimation of PDF and α_s uncertainties with sets from MSTW2008. Legend entries labeled "BF" refer to the best fit member of the PDF set and "PDF Var." stands for members where fit parameters have been varied.

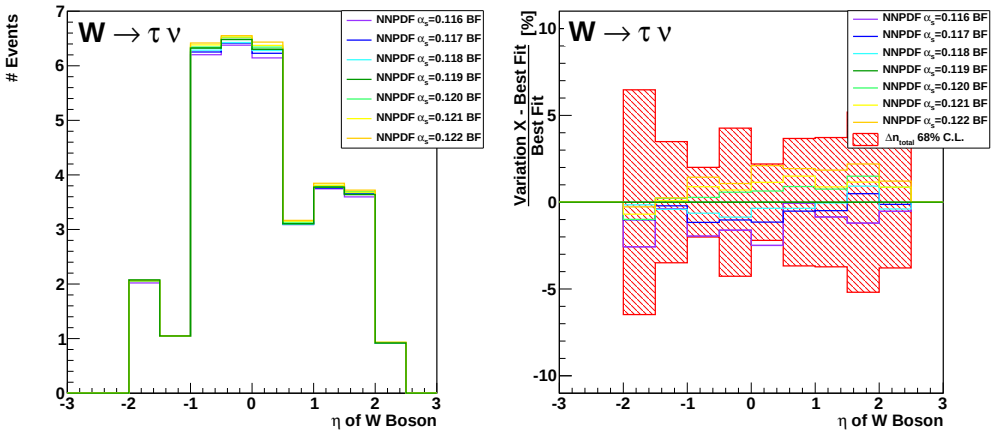

Figure D.7: η distribution of W boson for the estimation of combined PDF and α_s uncertainties with sets from NNPDF.

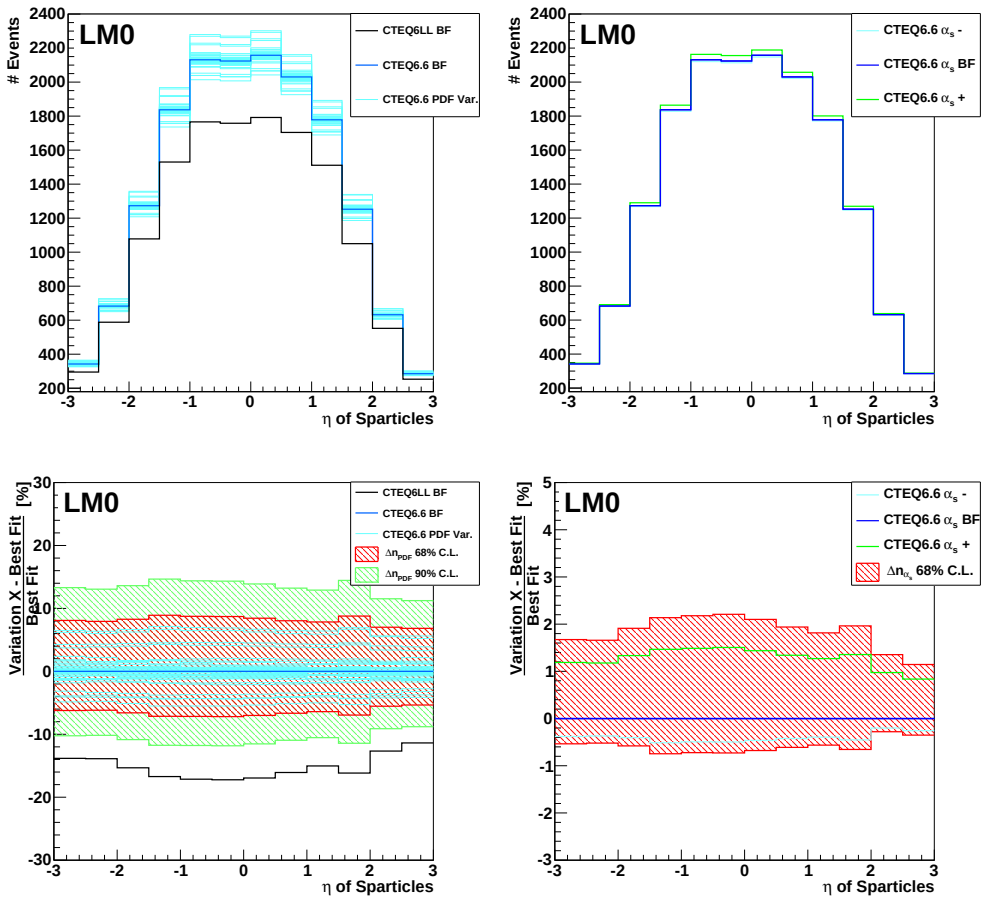

Figure D.8: η distribution of the produced sparticles for the estimation of PDF and α_s uncertainties with sets from CTEQ6.6. Legend entries labeled "BF" refer to the best fit member of the PDF set and "PDF Var." stands for members where fit parameters have been varied.

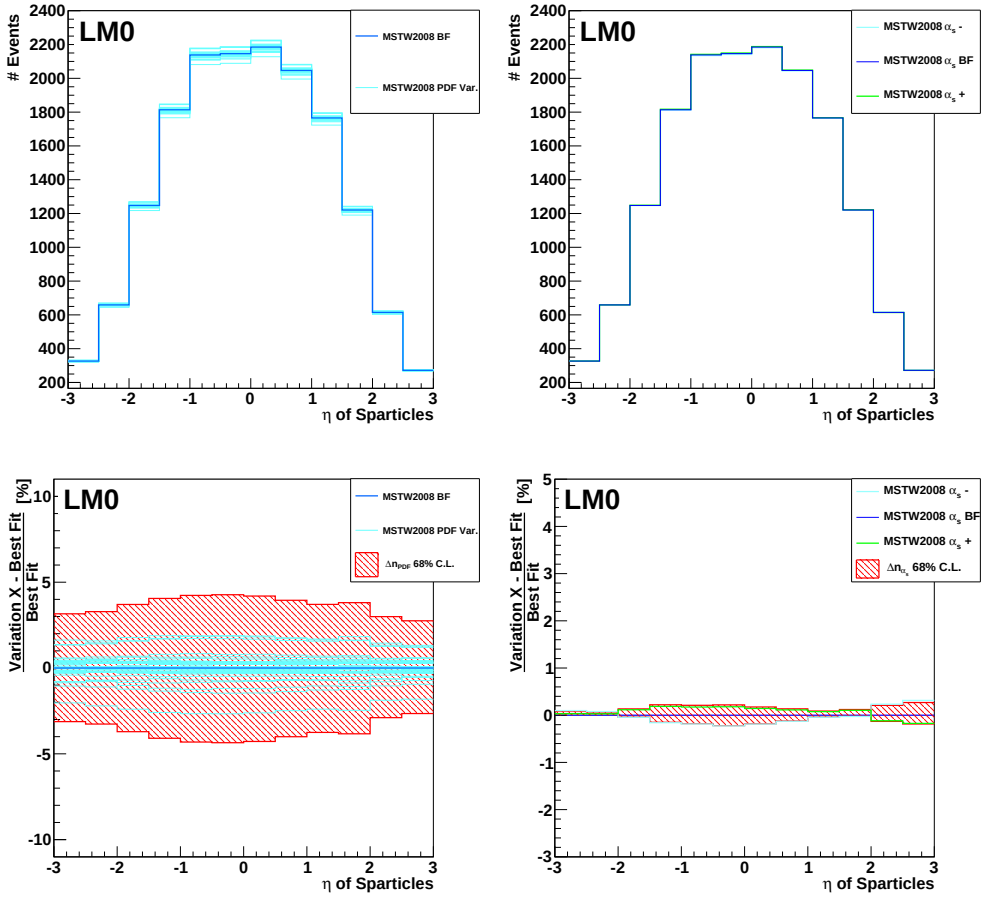

Figure D.9: η distribution of of the produced sparticles for the estimation of PDF and α_s uncertainties with sets from MSTW2008. Legend entries labeled "BF" refer to the best fit member of the PDF set and "PDF Var." stands for members where fit parameters have been varied.

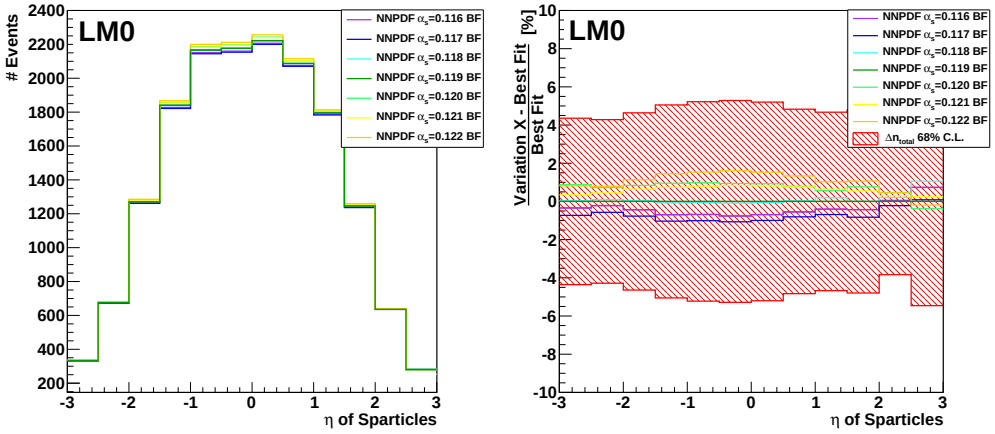

Figure D.10: η distribution of the produced sparticles for the estimation of combined PDF and α_s uncertainties with sets from NNPDF.

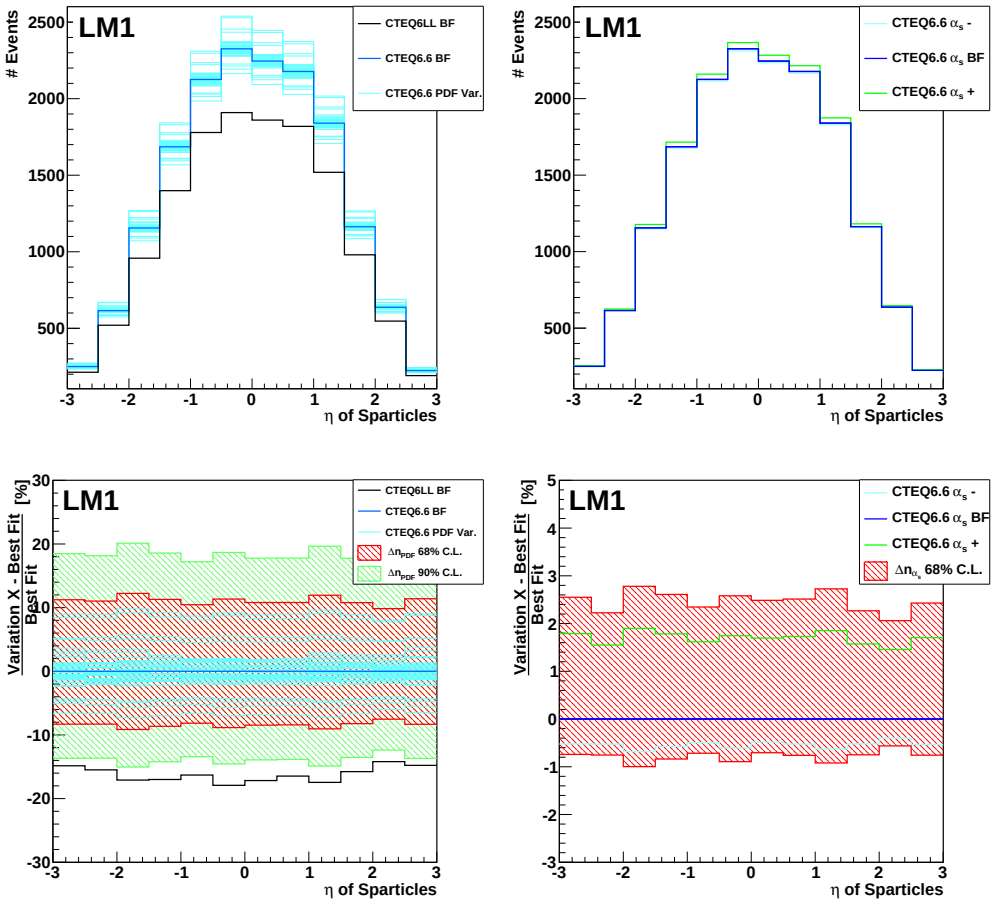

Figure D.11: η distribution of the produced sparticles for the estimation of PDF and α_s uncertainties with sets from CTEQ6.6. Legend entries labeled "BF" refer to the best fit member of the PDF set and "PDF Var." stands for members where fit parameters have been varied.

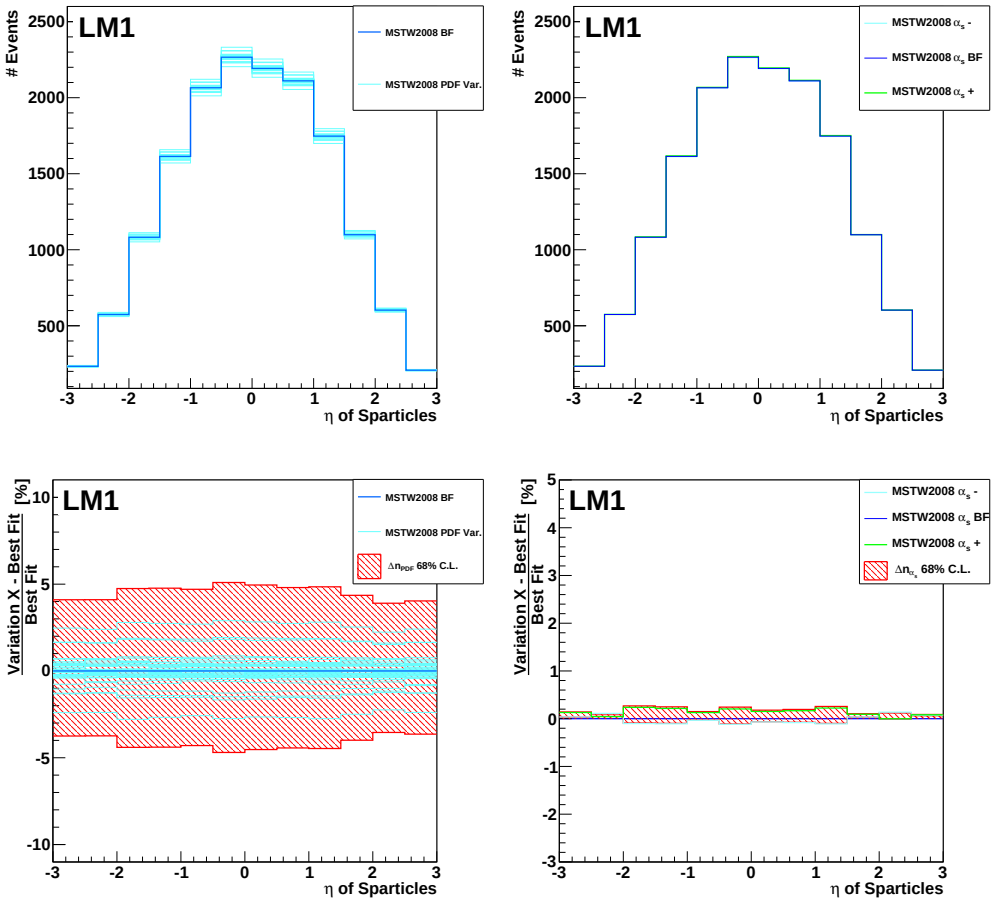

Figure D.12: η distribution of of the produced sparticles for the estimation of PDF and α_s uncertainties with sets from MSTW2008. Legend entries labeled "BF" refer to the best fit member of the PDF set and "PDF Var." stands for members where fit parameters have been varied.

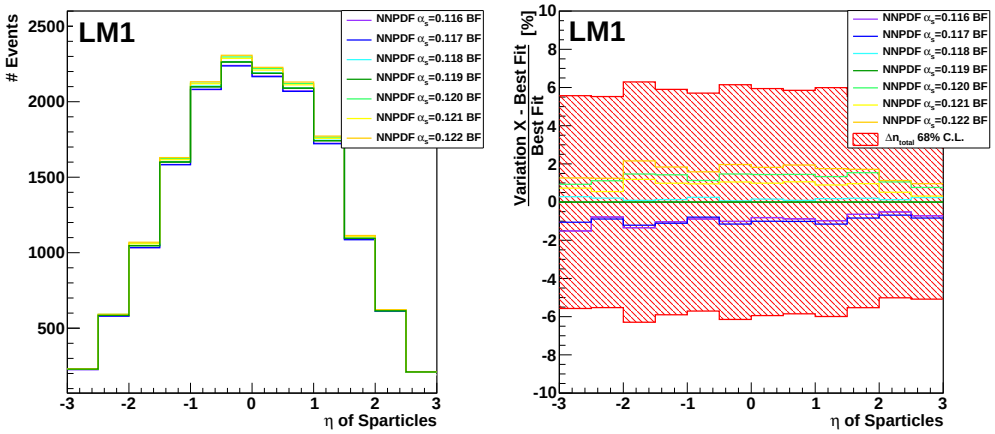

Figure D.13: η distribution of the produced sparticles for the estimation of combined PDF and α_s uncertainties with sets from NNPDF.

Bibliography

[1] D. Griffiths, "Introduction to Elementary Particles". WILEY-VCH Verlag GmbH & Co. KGaA, Weinheim, 2004.

[2] Particle Data Group, "Review of Particle Physics", *Journal of Physics G* **37 075021** (2010). http://pdg.lbl.gov/.

[3] "Symmetry - Dimensions of Particle Physics". http://www.symmetrymagazine.org/cms/?pid=1000708 accessed on 08/08/2011.

[4] A. H. Compton, "A Quantum Theory of the Scattering of X-rays by Light Elements", *Physical Review* **21** (1923) 483502. dio:10.1103/PhysRev.21.483.

[5] B. T. Cleveland, T. Daily, R. Davis et al., "Measurement of the Solar Electron Neutrino Flux with the Homestake Chlorine Detector", *The Astrophysics Journal* **496** (1998) 1. doi:10.1086/305343.

[6] SNO Collaboration, "Measurement of the Rate of ν_e+dp+p+e$^-$ Interactions Produced by ^{8}B Solar Neutrinos at the Sudbury Neutrino Observatory", *Physics Review Letters* **87** (2001) 071301. dio:10.1103/PhysRevLett.87.071301.

[7] A. Djouadi, "The Anatomy of Electro-Weak Symmetry Breaking. I: The Higgs boson in the Standard Model", *Physics Reports* **457:1-216** (2008) arXiv:hep-ph/0503172.

[8] G. Abbiendi, "Search for the Standard Model Higgs Boson at LEP", *Physics Letters B* **565:61-75** (2003) arXiv:hep-ex/0306033.

[9] The TEVNPH Working Group, "Combined CDF and DØ Upper Limits on Standard Model Higgs Boson Production with up to 8.6 fb$^-$1 of Data", *Fermilab Confrence Report* **FERMILAB-CONF-11-354-E** (2011) arXiv:1107.5518.

[10] CMS Collaboration, "Search for standard model Higgs boson in pp collisions at $\sqrt{s}$= 7 TeV", *CMS Physics Analysis Summary* **CMS PAS HIG-11-011** (2011).

[11] ATLAS Collaboration, "Combined Standard Model Higgs Boson Searches in pp Collisions at s = 7 TeV with the ATLAS Experiment at the LHC", *ATLAS Conference Note* **ATLAS CONF-2011-112** (2011).

[12] J. L. Feng, J.-F. Grivaz, and J. Nachtman, "Searches for Supersymmetry at High-Energy Colliders", *Reviews of Modern Physics* **82** (2010) 699727. dio:10.1103/RevModPhys.82.699.

[13] P. Binétruy, "Supersymmetry: Theory, Experiment and Cosmology". Oxford University Press Inc., New York, 2006.

[14] N. Jarosik, C. L. Bennett, J. Dunkley et al., "Seven-Year Wilkinson Microwave Anisotropy Probe (WMAP) Observations: Sky Maps, Systematic Errors, and Basic Results", *The Astrophysical Journal Supplement Series* **192** (2011) 14. doi:10.1088/0067-0049/192/2/14.

[15] G. Bertone, D. Hooper, and J. Silk, "Particle dark matter: evidence, candidates and constraints", *Physics Reports* **405** (2005) 279–390. doi:10.1016/j.physrep.2004.08.031.

[16] J. R. Primack, "Dark Matter and Structure Formation", (1997). arXiv:astro-ph/9707285.

[17] G. Angloher, M. Bauer, I. Bavykina et al., "Results from 730 kg days of the CRESST-II Dark Matter Search", (2011). arXiv:1109.0702v1.

[18] CDMS Collaboration, "Results from a Low-Energy Analysis of the CDMS II Germanium Data", *Physics Review Letters* **106** (2011) 131302. dio:10.1103/PhysRevLett.106.131302.

[19] S. P. Martin, "A Supersymmetry Primer", (2008) arXiv:hep-ph/9709356.

[20] "Pre-SUSY 2010". Lecture by S. P. Martin based on [19] http://susy10.uni-bonn.de/presusy.php accessed on 08/25/2011.

[21] S. Coleman and J. Mandula, "All Possible Symmetries of the S Matrix", *Physical Review* **159** (1967) 1251. dio:10.1103/PhysRev.159.1251.

[22] The CMS TriDAS Project, "Technical Design Report Volume 2: Data Aquisation and High-Level Trigger", *CMS Technical Design Report* **CMS-TDR-6.2** (2002).

[23] A. D. Roeck, J. Ellis, F. Gianotti et al., "Supersymmetric Benchmarks with Non-Universal Scalar Masses or Gravitino Dark Matter", *The European Physical Journal C - Particles and Fields* **49** (2007), no. 4, 1041–1066. dio: 10.1140/epjc/s10052-006-0182-6.

[24] W. Adam et al., "Search for Single-Lepton SUSY Signatures (RA4): Background Determinations", *CMS Analysis Note* **CMS AN-2010/208** (2010).

[25] B. Allanach, "SOFTSUSY: a program for calculating supersymmetric spectra", *Computer Physics Communications* **143** (2002) 305–331. arXiv:hep-ph/0104145v16.

[26] A. Djouadi, M. Muhlleitner, and M. Spira, "Decays of Supersymmetric Particles: the program SUSY-HIT (SUspect-SdecaY-Hdecay-InTerface)", *Acta Physica Polonica B* **38** (2007) 635–644. arXiv:hep-ph/0609292v1.

[27] "CMS Twiki: SUSY benchmarks". https://twiki.cern.ch/twiki/bin/view/CMS/SUSYBenchmarks#Low_mass_LM_mSUGRA_benchmarks accessed on 08/08/2011.

[28] CMS Collaboration, "CMS Physics Technical Design Report, Volume II: Physics Performance", *Journal of Physics G: Nuclear and Particle Physics* **34** (2007), no. 6,. doi:10.1088/0954-3899/34/6/S01.

[29] T. Hebbeker, "Can the sneutrino be the lightest supersymmetric particle?", *Physics Letters B* **470** (1999) 259–262. doi:10.1016/S0370-2693(99)01313-1.

[30] T. Sjöstrand, S. Mrenna, and P. Skands, "PYTHIA 6.4 physics and manual", *Journal of High Energy Physics* **2006** (2006), no. 05, 026. doi:10.1088/1126-6708/2006/05/026.

[31] M. Muhlleitner, A. Djouadi, and Y. Mambrini, "SDECAY: a Fortran code for the decays of the supersymmetric particles in the MSSM", *Computer Physics Communications* **168** (2005) 46–70. doi:10.1016/j.cpc.2005.01.012.

[32] "CMS Twiki: SUSY Physics Analysis Group". https://twiki.cern.ch/twiki/bin/view/CMS/SUSY accessed on 09/05/2011.

[33] "CERN Document Server: The CERN accelerator complex". http://cdsweb.cern.ch/record/1260465 accessed on 09/11/2011.

[34] CMS Collaboration, "The CMS Experiment at the CERN LHC", *Journal of Instrumentation* **3** (2008) S08004. doi:10.1088/1748-0221/3/08/S08004.

[35] "CMS Twiki: CMS Luminosity Collision Data 2010". https://twiki.cern.ch/twiki/bin/view/CMSPublic/LumiPublicResults2010 accessed on 09/21/2011.

[36] L. Evans and P. Bryant, "LHC Machine", *Journal of Instrumentation* **3** (2008) S08001. doi:10.1088/1748-0221/3/08/S08001.

[37] ALICE Collaboration, "The ALICE experiment at the CERN LHC", *Jounal of Instrumentation* **3** (2008) S08002. doi:10.1088/1748-0221/3/08/S08002.

[38] ATLAS Collaboration, "The ATLAS Experiment at the CERN Large Hadron Collider", *Jounal of Instrumentation* **3** (2008) S08003. doi:10.1088/1748-0221/3/08/S08003.

[39] LHCb Collaboration, "The LHCb Detector at the LHC", *Jounal of Instrumentation* **3** (2008) S08005. doi:10.1088/1748-0221/3/08/S08005.

[40] LHCf Collaboration, "The LHCf detector at the CERN Large Hadron Collider", *Jounal of Instrumentation* **3** (2008) S08006. doi:10.1088/1748-0221/3/08/S08006.

[41] TOTEM Collaboration, "The TOTEM Experiment at the CERN Large Hadron Collider", *Jounal of Instrumentation* **3** (2008) S08007. doi:10.1088/1748-0221/3/08/S08007.

[42] CMS Collaboration, "The CMS Tracker System Project", *CMS Technical Design Report* **CMS-TDR-005** (1997).

[43] CMS Collaboration, "The Hadron Calorimeter Project", *CMS Technical Design Report* **CMS-TDR-2** (1997).

[44] CMS Collaboration, "CMS Physics Technical Design Report Volume I : Detector Performance and Software", *CMS Technical Design Report* **CMS-TDR-008-1** (2006).

[45] CMS Collaboration, "The CMS muon project", *CMS Technical Design Report* **CMS-TDR-003** (1997).

[46] The CMS TriDAS Project, "Technical Design Report Volume 1: The Trigger Systems", *CMS Technical Design Report* **CMS-TDR-6.1** (2000).

[47] S. Cucciarelli, M. Konecki, D. Kotlinski et al., "Track reconstruction, primary vertex finding and seed generation with the Pixel Detector", *CMS Note* **CMS NOTE 2006/26** (2006).

[48] R. Frühwirth, "Application of Kalman filtering to track and vertex fitting", *Nuclear Instruments and Methods in Physics Research* **262** (1987) 444–450. dio:10.1016/0168-9002(87)90887-4.

[49] CMS Collaboration, "Performance of muon reconstruction and identification in pp collisions at $\sqrt{s}$=7 TeV", *CMS Physics Analysis Summary* **CMS PAS MUO-10-004** (2011).

[50] S. Baffioni, C. Charlot, F. Ferri et al., "Electron reconstruction in CMS", *CMS Note* **CMS NOTE-2006/040** (2006).

[51] W. Adam, R. Frühwirth, A. Strandlie et al., "Reconstruction of Electrons with the Gaussian-Sum Filter in the CMS Tracker at the LHC", *CMS Note* **CMS NOTE 2005-001** (2005).

[52] CMS Collaboration, "Commissioning of the particle-flow event reconstruction with leptons from J/Psi and W decays at 7 TeV", *CMS Physics Analysis Summary* **CMS PAS PFT-10-003** (2010).

[53] CMS Collaboration, "Particle-Flow Event Reconstruction in CMS and Performance for Jets, Taus, and E_T^{miss}", *CMS Physics Analysis Summary* **CMS PAS PFT-09-001** (2009).

[54] M. Cacciari, G. P. Salam, and G. Soyez, "The anti- k t jet clustering algorithm", *Journal of High Energy Physics* **04** (2008) 063. doi:10.1088/1126-6708/2008/04/063.

[55] Y. Dokshitzer, G. Leder, S. Moretti et al., "Better jet clustering algorithms", *Journal of High Energy Physics* **08** (1997) 001. doi:10.1088/1126-6708/1997/08/001.

[56] S. Catani, Y. L. Dokshitzera, M. H. Seymour et al., "Longitudinally-invariant $k_\perp$-clustering algorithms for hadron-hadron collisions", *Nuclear Physics B* **406** (1993), no. 08, 187–224. doi:10.1016/0550-3213(93)90166-M.

[57] CMS Collaboration, "Missing E_T performance", *CMS Physics Analysis Summary* **CMS PAS JME-07-001** (2007).

[58] CMS Collaboration, "Performance of Jet Algorithms in CMS", *CMS Physics Analysis Summary* **CMS PAS JME-07-003** (2007).

[59] CMS Collaboration, "Performance of Track-Corrected Missing Transverse Energy in CMS", *CMS Physics Analysis Summary* **CMS PAS JME-09-010** (2009).

[60] CMS Collaboration, "Missing transverse energy performance of the CMS detector", *Jounal of Instrumentation* **CMS-JME-10-009**.

[61] CMS Collaboration, "Determination of Jet Energy Calibration and Transverse Momentum Resolution in CMS", *Jounal of Instrumentation* **CMS-JME-10-011** (2011).

[62] "CMS Twiki: Introduction to Jet Energy Corrections at CMS". https://twiki.cern.ch/twiki/bin/view/CMS/IntroToJEC accessed on 09/04/2011.

[63] CMS Collaboration, "Jet Energy Resolution in CMS at $\sqrt{s}$=7 TeV", *CMS Physics Analysis Summary* **CMS PAS JME-10-014** (2011).

[64] TOTEM Collaboration, "First measurement of the total proton-proton cross section at the LHC energy of $\sqrt{s}$ =7 TeV", (2011). arXiv:1110.1395v1.

[65] A. Quadt, "Top quark physics at hadron colliders", *The European Physical Journal C - Particles and Fields* **48** (2006), no. 3, 835–1000. doi:10.1140/epjc/s2006-02631-6.

[66] Geant4 Collaboration, "GEANT 4 a simulation toolkit", *Nuclear Instruments and Methods in Physics Research A* **506** (2003) 250303. doi:10.1016/S0168-9002(03)01368-8.

[67] F. Maltoni and T. Stelzer, "MadEvent: Automatic Event Generation with MadGraph", *Journal of High Energy Physics* **02** (2003) 27, arXiv:hep-ph/0208156.

[68] Z. Was, "TAUOLA the library for tau lepton decay, and KKMC/KORALB/KORALZ/... status report", *Nuclear Physics B - Proceedings Supplements* **98** (2001) 96–102. arXiv:hep-ph/0011305v1.

[69] CDF Collaboration, "Studying the Underlying Event in Drell-Yan and High Transverse Momentum Jet Production at the Tevatron", *Physics Review D* **82** (2010) 034001. 10.1103/PhysRevD.82.034001.

[70] CMS Collaboration, "Measurement of the Underlying Event Activity at the LHC with $\sqrt{s}$= 7 TeV and Comparison with $\sqrt{s}$ = 0.9 TeV", *Journal of High Energy Physics* **9** (2011) 109. doi:10.1007/JHEP09(2011)109.

[71] R. Field, "Early LHC Underlying Event Data - Findings and Surprises",. Proceedings of the invited talk at HCP2010, Toronto, August 23, 2010 arXiv:1010.3558v1.

[72] "CMS Twiki: GeneratorProduction2010 – ReProcessingWinter2010". https://twiki.cern.ch/twiki/bin/viewauth/CMS/ReProcessingWinter2010 accessed on 10/18/2011.

[73] "CMS Twiki: Standard Model Cross Sections for CMS at 7 TeV". https://twiki.cern.ch/twiki/bin/view/CMS/StandardModelCrossSections accessed on 08/08/2011.

[74] CMS Collaboration, "Search for supersymmetry in pp collisions at $\sqrt{s} = 7$ TeV in events with a single lepton, jets, and missing transverse momentum", (2011). arXiv:1107.1870v1.

[75] CMS Collaboration, "Measurement of the W and Z inclusive production cross sections at sqrts=7 TeV with the CMS experiment at the LHC", *CMS Physics Analysis Summary* **CMS PAS EWK-10-002** (2010).

[76] M. Mulders, I. Bloch, E. James et al., "Muon Identification in CMS", *CMS Analysis Note* **CMS AN-2008/098** (2008).

[77] CMS Collaboration, "Performance of muon identification in pp collisions at $\sqrt{s} = 7$ TeV", *CMS Physics Analysis Summary* **CMS PAS 10-002** (2010).

[78] "CMS Twiki: Electron Identification Based on Simple Cuts". https://twiki.cern.ch/twiki/bin/view/CMS/SimpleCutBasedEleID accessed on 08/19/2011.

[79] D. Newbold, R. Walton, O. Charaf et al., "Electron ID at High Energies", *CMS Analysis Note* **CMS AN-2008/045** (2008).

[80] O. Charaf, B. Clerbaux, G. D. Lentdecker et al., "Search for high mass resonances decaying into an electron pair in CMS at 10 TeV with 100 pb^{-1}", *CMS Analysis Note* **CMS AN-2009/097** (2009).

[81] S. Harper and C. Shepherd-Themistocleous, "Improving Sigma Eta Eta". Talk held in CMS Egamma group meeting on 07/28/2008.

[82] D. Barge, C. Campagnari, S. Gessner et al., "Study of photon conversion rejection at CMS", *CMS Analysis Note* **CMS AN-2009/159** (2009).

[83] "CMS Twiki: Jet Identification". https://twiki.cern.ch/twiki/bin/viewauth/CMS/JetID accessed on 08/22/2011.

[84] CMS Collaboration, "Jet Performance in pp Collisions at 7 TeV", *CMS Physics Analysis Summary* **CMS PAS JME-10-003** (2010).

[85] C. Magass, "Study of ECal Noise". Talk held in III. Phys. Inst. A - Weekly Meeting 01/28/2010.

[86] C. Magass, "Search for New Heavy Charged Gauge Bosons". PhD thesis, III. Phys. Inst. A, RWTH Aachen, 2007.

[87] D. Kovalskyi, M. Tadel, A. Mrak-Tadel et al., "Fireworks: A physics event display for CMS", *Journal of Physics: Conference Series* **219** (2010) 3. doi:10.1088/1742-6596/219/3/032014.

[88] "CMS detector overview". http://cms.web.cern.ch/cms/Detector/FullDetector/index.html accessed on 09/07/2011.

[89] D. Duchardt, C. Magass, A. Meyer and D. Teyssier, "Search for Supersymmerty with a Single Muon, Jets and Large Transverse Missing Energy", *CMS Analysis Note* **CMS AN-2011/415** (2011).

[90] S. Alekhin, S. Alioli, R. D. Ball et al., "The PDF4LHC Working Group Interim Report", (2011) arXiv:1101.0536.

[91] A. Vicini, "Practical implementation of the PDF4LHC recipe". http://www.hep.ucl.ac.uk/pdf4lhc/ accessed on 08/16/2011.

[92] J. Pumplin, D. Stump, R. Brock et al., "Uncertainties of predictions from parton distribution functions II: the Hessian method", *Physics Reviews D* **65:014013** (2001) arXiv:hep-ph/0101032.

[93] R. D. Ball, L. D. Debbio, S. Forte et al., "A determination of parton distributions with faithful uncertainty estimation", *Nuclear Physics B* **809** (2009), no. 1-2, 1 – 63. doi:10.1016/j.nuclphysb.2008.09.037.

[94] A. Martin, W. Stirling, R. Thorne et al., "Parton distributions for the LHC", *The European Physical Journal C - Particles and Fields* **63** (2009) 189–285. doi:10.1140/epjc/s10052-009-1072-5.

[95] G. Sterman, J. Smith, J. C. Collins et al., "Handbook of perturbative QCD", *Reviews of Modern Physics* **67** (1995) 157248. doi:10.1103/RevModPhys.67.157.

[96] D. Bourilkov, R. C. Group, and M. R. Whalley, "LHAPDF: PDF Use from the Tevatron to the LHC", (2007) arXiv:hep-ph/0605240.

[97] P. Biallass, T. Hebbeker, C. Hof et al., "Parton Distribution Uncertainty Determination within CMSSW", *CMS Analysis Note* **CMS AN-2009/048** (2009).

[98] S. Gieseke, "Uncertainties of Sudakov form factors", *Journal of High Energy Physics* **053** (2005) 01. doi:10.1088/1126-6708/2005/01/058.

[99] "LHAPDF the Les Houches Accord PDF Interface". http://projects.hepforge.org/lhapdf/ accessed on 08/30/2011.

[100] H. Held, P. Schieferdecker, and M. Voutilainen, "Update of the Measurement of the Jet p_T Resolution in $\sqrt{s}$=7 TeV Collision Data with the Asymmetry Method", *CMS Analysis Note* **CMS AN-2010/371** (2010).

[101] S. Bhattacharya, S. Jain, M. Pieri et al., "Search for an Excited Electron in pp Collisions at $\sqrt{s}$= 7 TeV", *CMS Analysis Note* **CMS AN-2010/320** (2010).

[102] CMS Collaboration, "MET Performance in pp Collisions at $\sqrt{s}$=7 TeV", *CMS Physics Analysis Summary* **CMS PAS JME-10-009** (2010).

[103] CMS Collaboration, "Absolute luminosity normalization", *CMS Detector Performance Summary* **CMS DP-2011-002** (2011).

[104] "CMS Twiki: RooStats CL95: cross section in a counting experiment". https://twiki.cern.ch/twiki/bin/view/CMS/RooStatsCl95 accessed on 09/03/2011.

[105] DØ Collaboration, "A Recipe for the construction of confidence limits", *Fermilab Technical Publication* **FERMILAB-TM-2104**.

[106] G. Cowan, "Statistical Data Analysis". Oxford University Press Inc., New York, 1998.

[107] A. Caldwell, D. Kollar, and K. Kroeninger, "BAT - The Bayesian Analysis Toolkit", (2008) arXiv:0808.2552.

[108] "CMS Twiki: Simulating and Reconstructing events with Fast Simulation". https://twiki.cern.ch/twiki/bin/view/CMSPublic/WorkBookFastSimulation accessed on 09/08/2011.

[109] "CMS Twiki: SUSY Scan points using CMSSW 3.8.x at 7 TeV". https://twiki.cern.ch/twiki/bin/view/CMS/SUSY38XSUSYScan accessed on 09/08/2011.

[110] W. Beenakker, R. Höpker, M. Spira et al., "Squark and Gluino Production at Hadron Colliders", *Nuclear Physics B* **492** (1997) 51–103. arXiv:hep-ph/9610490v1.

[111] "PROSPINO2". http://www.thphys.uni-heidelberg.de/~plehn/prospino/ accessed on 09/19/2011.

[112] C. J. Clopper and E. S. Pearson, "The use of confidence or fiducial limits illustrated in the case of the binomial", *Biometrika* **26** (1934) 404413. doi:10.1093/biomet/26.4.404 .

[113] M. Paterno, "Calculating Efficiencies and Their Uncertainties", *Fermilab Technical Publication* **FERMILAB-TM-2286-CD** (2003).

[114] "CMS Twiki: SUSY Tools and guidelines for limits (2010 data publications)". https://twiki.cern.ch/twiki/bin/view/CMS/SUSYLimitTools accessed on 09/21/2011.

[115] H. Baer, C. Chen, M. Drees et al., "Collider Phenomenology for Supersymmetry with Large tan β", *Physics Review Letters* **79** (1997) 986989. doi:10.1103/PhysRevLett.79.986.

[116] "LEP2 SUSY Working Group: Combined LEP Chargino Results, up to 208 GeV for low DM". http://lepsusy.web.cern.ch/lepsusy/www/inoslowdmsummer02/charginolowdm_pub.html accessed on 09/20/2011.

[117] "LEP2 SUSY Working Group: Combined LEP Selectron/Smuon/Stau Results, 183-208 GeV". http://lepsusy.web.cern.ch/lepsusy/www/sleptons_summer04/vec/lwg_sel_adlo_184_208_obr.vec accessed on 09/20/2011.

[118] "LEP 2 Joint SUSY Working Group: ALEPH, DELPHI, L3, OPAL Experiments". http://lepsusy.web.cern.ch/lepsusy/Welcome.html accessed on 09/20/2011.

[119] "The LEP-SUSY Working Group: Interpretation of the results in Minimal SUGRA". http://lepsusy.web.cern.ch/lepsusy/www/lspmsugra_summer02/02-06.2/mSUGRA_208.html accessed on 09/20/2011.

[120] DØ Collaboration, "Search for squarks and gluinos in events with jets and missing transverse energy using 2.1 fb^1 of p$\bar{\text{p}}$ collision data at $\sqrt{s}$=1.96 TeV", *Physics Letters B* **660** (2008) 449–457. doi:10.1016/j.physletb.2008.01.042.

[121] CDF Collaboration, "Inclusive Search for Squark and Gluino Production in p$\bar{\text{p}}$ Collisions at $\sqrt{s} = 1.96$ TeV", *Physics Review Letters* **102** (2009) 121801. doi:10.1103/PhysRevLett.102.121801.

[122] DØ Collaboration, "Search for Supersymmetry via Associated Production of Charginos and Neutralinos in Final States with Three Leptons", *Physics Review Letters* **95** (2005) 151805. doi:10.1103/PhysRevLett.95.151805.

[123] ATLAS Collaboration, "Search for supersymmetry using final states with one lepton, jets, and missing transverse momentum with the ATLAS detector in $\sqrt{s} = 7$ TeV pp", *Physics Review Letters* **106** (2011) 131802. doi:10.1103/PhysRevLett.106.131802.

[124] "LHC Luminosity Plots for the 2011 Proton Run". http://lpc.web.cern.ch/lpc/lumiplots.htm accessed on 09/21/2011.

[125] "CMS Twiki: CMS Supersymmetry Physics Results". https://twiki.cern.ch/twiki/bin/view/CMSPublic/PhysicsResultsSUS accessed on 09/21/2011.

[126] S. AbdusSalam, B. Allanach, H. Dreiner et al., "Benchmark Models, Planes, Lines and Points for Future SUSY Searches at the LHC", (2011). arXiv:1109.3859v1.

Danksagung

Zum Ende meines Studiums hin möchte ich mich bei zahlreichen Personen bedanken, die zum Entstehen dieser Diplomarbeit beigetragen haben. Mein erster Dank gebührt Prof. Dr. Thomas Hebbeker, der es mir ermöglicht hat im III. Physikalischen Institut A – während dieser spannenden Zeit der LHC Physik – eine Arbeit innerhalb der CMS Gruppe anzufertigen. Ich habe mich sehr über die Unterstützung bei Vorträgen und der Entwicklung dieser Analyse gefreut, ebenso über Ihre konstruktive Kritik an dem Entwurf dieser Diplomarbeit. Weiterhin bedanke ich mich bei Prof. Dr. Christopher Wiebusch des III. Physikalischen Instituts B, der sich bereit erklärt hat das Zweitgutachten meiner Arbeit zu übernehmen.

Für die wertvollen Ratschläge bei der Korrektur diverser Vorversionen dieser Arbeit sei herzlichst Arnd Meyer, Markus Merschmeyer, Holger Pieta und Martin Weber gedankt. Für die Entwicklung des ACSusy frameworks, welches maßgeblich zur technischen Implementierung dieser Analyse beigetragen hat, möchte ich Carsten Magaß vielmals danken, ebenso für die geduldige Betreuung.

Weiterhin danke ich der gesamten Arbeitsgruppe am III. Physikalischen Institut. Ihr habt alle zu dem angenehmen Arbeitsklima vor Ort beigetragen und viel Zeit für Fragen, offene Diskussionen und Problemlösungen (physikalischer und technischer Natur) bereit gestellt. Zur positiven Atmophäre und für unvergessliche Momente haben auch nette Gespräche zwischen durch und auf Dienstreisen beigetragen. Namentlich erwähnen möchte ich an dieser Stelle auch noch: Metin Ata, Michael Bontenackels, Adriana Del Piero, Matthias Endres, Andreas Güth, Kerstin Höpfner, Thomas Kreß, Mark Olschewski, Klaas Padeken, Paul Papacz, Stefan Schmitz, Jan Schulte, Daniel Teyssier, Sebastian Thüer und Peter Vanhoegen. Ohne euch wäre die Diplomarbeit in dieser Form nicht möglich gewesen.

Vielen Dank auch an Rebbeka Höing für die zahllosen Tage des gemeinsamen Studierens, inklusive stressiger Zeiten während der Praktika oder Prüfungsphasen, netten Erlebnissen außerhalb der Physik, sowie der tolle Zusammenhalt und gute Humor auch in frustrierenden Phasen.

Zu guter Letzt möchte ich mich bei meiner Familie bedanken, die mich während des gesamten Studiums liebevoll und ausdauernd unterstützt hat. Euer reges Interesse und Anteilnahme auch an meiner Diplomarbeit hat mir sehr viel bedeutet.

Selbständigkeiterklärung

Hiermit erkläre ich, dass ich die vorliegende Arbeit eigenständig verfasst habe. Desweiteren habe ich Zitate kenntlich gemacht und keine anderen als die angegebenen Hilfsmittel und Quellen verwendet.

Aachen, den 24.10.2011

_____

Deborah Duchardt